University of Sussex

New Frontiers in Terahertz Microscopy:

Development of Novel Near-Field Imaging Methodologies

Robyn Tucker

Submitted for the degree of Doctor of Philosophy

University of Sussex

Winter 2021

Declaration

I hereby declare that this thesis has not been and will not be submitted in whole or in part to another University for the award of any other degree.

Signature:

Robyn Tucker

UNIVERSITY OF SUSSEX

Robyn Tucker, Doctor of Philosophy

New Frontiers in Terahertz Microscopy: Development of Novel Near-Field Imaging Methodologies

–

Summary

Time-Domain imaging at Terahertz (THz) frequencies exploits illumination with short broadband electromagnetic pulses and has become a crucial tool for coherent 2D spectral analysis since its inception in 1995. Many materials of interest, bio compounds and even explosives exhibit typical revealing spectral signatures in this band. In addition, the interaction of terahertz waves with free carriers is widely used as diagnostic in several conducting and semiconducting media. A peculiar distinction established in the THz field is the ability to access the evolution of the full electromagnetic field in time (in the picosecond time-scale). Established implementations are generally remarkably slow, especially resolution finer than the wavelength are targeted, making them of limited practical significance in many fields. Approaching the desired resolutions with a real-time video rate is still a challenge. This work concerns the development of two novel methodologies that sharply move above state of the art, pushing forward all the typical qualifying features of THz imaging, enabling the field to further grow and even outpace the scope of established imaging techniques. The first methodology I developed, in terms of physical mechanism and methodological approach, regards a way to map ultrafast dynamics of carriers using terahertz imaging with resolution significantly

finer than the wavelength and acquisition rate approaching video-rate, which is unprecedented in the field. I conceived a video-rate large-area THz carrier analysis approach that allowed for phase-sensitive measurement of the conductivity changes that photo-excited carriers introduce in samples, significantly surpassing the performances of established approaches to map carrier relaxation dynamics and relate them to material properties in complex structures. This novel technique, the Optical Pump – Terahertz Near-field Microscopy, made THz carrier analysis possible simultaneously on large surfaces, showing how the full microscopic distribution of THz conductivity is affected by a distribution of hot carriers that lies on the sample plane. The technique achieves a video rate of multiple frames per second and also a subwavelength spatial resolution that exceeds $\lambda/20$. The second methodology I contributed to in my thesis work regards the establishment of a single-pixel terahertz microscopy approach, which does not require arrays of sensors. THz raster scan imaging approach has been around for a while. However, the achievable signal-to-noise ratio and the exploitation of mechanics scanning mechanisms fundamentally limit their performances. Within a research team, we then introduced the Nonlinear Ghost Imaging an approach that places a sample in the near-field of a optical-to-terahertz converter. My specific contribution regarded the specific methodological approach of sampling the object with a series of terahertz patterns and reconstructing the image by correlating this information with the information obtained with a single-pixel terahertz detector. Again, this approach significantly outperforms the state-of-the-art in terms of fidelity of the reconstructed spectral information and its publication is having a transformative effect on the field. This thesis work serves as a presentation of methodologies and results and also covers related issues such as limitations and future development, with a comprehensive exploration of the motivations behind the work and the general impact in the domain. Because some results and achievements are certainly the result of a teamwork, I will present them in a comprehensive manner, and then I will highlight my specific contribution.

Acknowledgements

I would like to thank Prof. Marco Peccianti for answering all of my questions, no matter how ridiculous, and for always supporting me. I'd also like to thank Prof. Alessia Pasquazi for her guidance, and Dr. Luke Peters and Dr. Juan Sebastian Totero-Gongora for helping me to understand the Terahertz field. Finally, I'd like to thank Dr. Jacob Tunesi and Dr. Maxwell Rowley for all of their help in the lab.

This project has received funding from the European Research Council under the European Union's Horizon 2020 research and innovation programme Grant agreement n°725046

Contents

List of Figures

Chapter 1

Introduction to Terahertz Analysis

1.1 Terahertz Radiation

The focus of this thesis discussion is Terahertz (THz) Radiation and a specific subset of its uses in imaging. The electromagnetic spectrum is the vast range of frequencies that the field manifestations of the electromagnetic force can possess. Photon energy, and thus frequency, is often the determining factor in any field-media interaction; understandably, there has always been interest in finding applications for the different frequency regions in the spectrum. Although the microscopic interaction driving a medium dielectric responses can have very different origin, interaction with low energy photons (meV) often relates to vibrational modes, as opposed to optical photons often triggering electronic transitions. Hence, for example in organic chemical molecular solids and polymers, intra-molecular bonds classically have resonances above Mid-Infrared wavelengths; molecular vibrational and rotational modes and inter-molecular weak bonds that resonate within the THz band. In addition, in inorganic crystalline and amorphous solids and metal, using THz as probe has the inherent advantage of not eliciting significant quantum transition on carriers because of the relative low energy photon. (Lee, 2009a) Essentially, a full classical description can be adopted on a relatively large excitation bandwidth. The THz frequency range was chronically under-explored until the late 20^{th} century because of the general unavailability of bright sources outside of big infrastructure (e.g. synchrotrons). In addition, thermal sources have been practically irrelevant below the 10 THz mark, as opposed to the flourishing pre-laser optical field. Probably the relevant milestone towards the adoption of THz systems has been the demonstration of ultra-short laser emission based on laser-mode-locking (Garmire and Yariv, 1967). Time domain terahertz systems exploit optical-to-terahertz conversion elicited by an ultra-fast field-matter interaction and by the large

instantaneous power of such laser pulses. The demonstration of chirped-pulse regenerative amplification, awarded very recently with a Nobel prize (Strickland and Mourou, 1985), enabled the generation of very bright terahertz pulses via nonlinear optical conversion, a foundation principle in this thesis. Relevant sources of THz radiation are described in detail in later chapters where the fundamental processes that contribute to their function are also explored.

1.1.1 The Definition of Terahertz

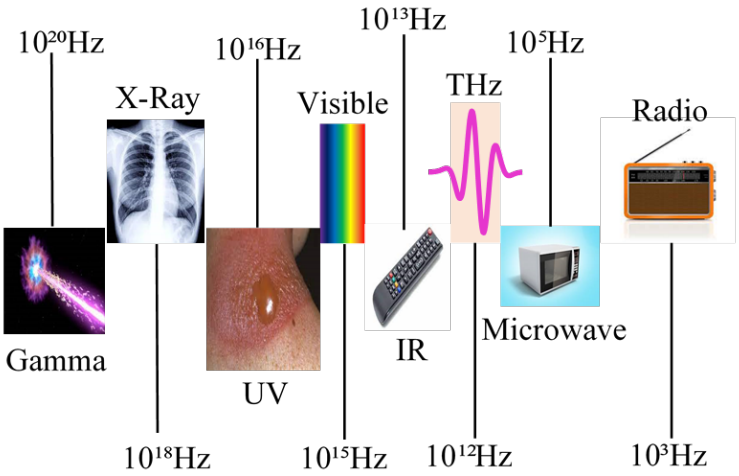

Figure 1.1: A scale illustrating different applications of electromagnetic radiation and their frequencies.

Terahertz radiation is traditionally an electromagnetic radiation in the frequency range of 0.1 THz to 10 THz, though some definitions extend beyond these margins. This region of the spectrum lies between the infrared (IR) and microwave parts of the electromagnetic spectrum. Interestingly, while IR and microwave are exclusive domains of (quantum) photonics sources (Jung et al., 2017) and electronics sources (Gu et al., 2017), ironically terahertz has been traditionally inaccessible to both, because the photon energy is too low and because the relative frequency is above the electronic bandwidth cut-off (Williams, 2005). Yet, many substances contain a unique spectral fingerprint in the THz region including bio-molecules (Zheng et al., 2012) and other chemicals (Fischer et al., 2005); this was a key motivator for the development of pulsed, broadband THz radiation for spectral analysis (Helminger et al., 1983). Unlike optical radiation, THz is invisible to the human eye and unlike x-ray, Ultra-violet and gamma radiation is non-ionising to biological tissue (Seo et al., 2015) and therefore non-destructive. Notably, in modern

technological settings there is a fundamental distinction between technologies producing continuous-wave terahertz emission, some of very recent demonstration (e.g. diodes and quantum-cascade-laser (Zeng et al., 2020)), and broadband pulsed laser sources. This thesis work is indeed related to the latter.

1.1.2 Terahertz Spectroscopy

There are not that many ways to identify the composition of an unknown substance. The available methods fall into two categories: destructive and non-destructive (Wang et al., 2020). Destructive methods often utilise chemical analysis and ionising radiation whereas non-destructive methods can utilise, for example, optical spectroscopy or ultrasound (Achenbach, 2000). Because THz radiation is non-ionising, (Seo et al., 2015) it does not destroy biological samples and thus is also an effective mode of non-destructive evaluation. With optical spectroscopy a vast range of wavelengths can be used to identify resonances, revealing particular media. High frequency photons, as in ultraviolet light, can illuminate inter-band transitions of core electrons (Fabian et al., 1971) while low frequency photons in mid- and far-infrared can identify large molecules, because of their structural resonance, like fatty acids (Meiklejohn et al., 1957). The wide range of available photon interactions necessitates spectroscopy applications for a variety of wavelength ranges and different detection techniques (Jepsen et al., 2011) depending on available technology as well as material state and conductivity. Terahertz spectroscopy can highlight low energy

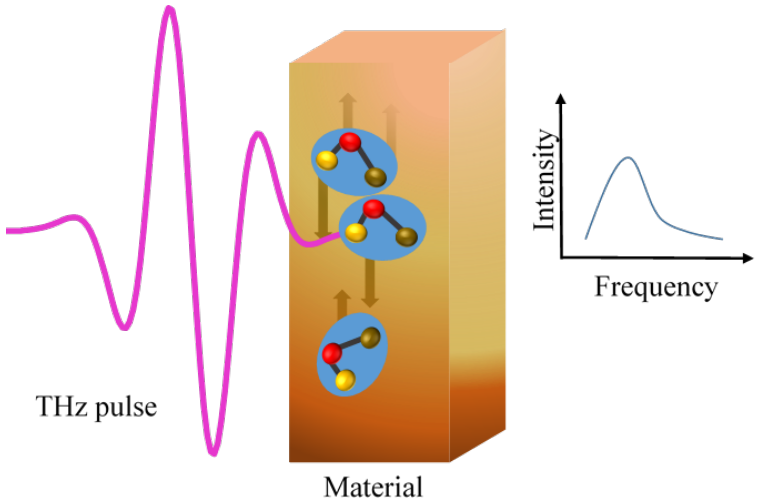

Figure 1.2: A graphic displaying the interaction between a THz field and molecular vibrational modes in a material. As seen on the right, analysis of the THz field yields an absorption spectrum in the frequency domain.

molecular transitions, for example the vibrational modes of polyatomic molecules (Leonhardt et al., 1987). Protein unfolding or other molecular processes can be quantified at the molecular level via their vibrational response to THz (Okumura and Tanimura, 1998). Interestingly, many of these proteins must be suspended in solutions, and water is a notoriously strong THz absorber (Gente et al., 2013), reducing the measurable field interaction. However, water absorption has been used for analysis of cancerous tissue (Woodward et al., 2002), which can be differentiated from their surroundings by the different concentration of blood vessels (Yu et al., 2012).

Time Domain Terahertz Spectroscopy

An interesting aspect in the generation of broadband Terahertz pulses from laser pulses is that the resulting long THz wave-period lies in the same dimensional scale as the duration of the optical pulse that excites its generation (Valdmanis et al., 1983). Conceptually, this means that a replica of this pulse can be used to synchronously 'sample' the field of a terahertz pulse in a certain point in space via a nonlinear device. By altering the delay between the two pulses we can change the sampling point in the terahertz wave. This concept is known in literature as time-domain-spectroscopy (TDS).

Primordial examples of generation and detection of terahertz waves via optical sampling was reported by Auston et al. (1980) (whereas first examples of terahertz generation from optical pulses date back to Yang et al. (1971)). The first example of TDS in its complete definition was reported by the same group in 1983, Valdmanis et al. (1983); a carrier spectroscopy demonstration using terahertz waves was reported much later (Nuss et al., 1987), in the framework of Measurement of Carrier Mobility of Photo-excited Electrons in Gallium Arsenide.

The core feature of the Time Domain Spectroscopy (TDS) is to operate via the complete reconstruction of the field-transient of short THz (Valdmanis et al., 1983). The basic idea is that the field is transmitted through an object (or reflected from it) and the change of the detected waveform can be used to infer the dielectric response of the object. The detection, usually referred as electro-optical sampling, of the field operates on the assumption that the THz waveform and the probing optical pulse are synchronised and then the optical pulse is sufficiently shorter than the terahertz period to fulfil the Nyquist-Shannon sampling limit (Weingarten et al., 1988). Phase-resolved techniques, popularised by Wu and Zhang (1995) among others, allowed for the amplitude of the field rather than the intensity to be measured as a voltage, offering extra insight into field and sample properties.

The resulting dataset can be used to determine complex parameters of an object such as the complex refractive index (Francis et al., 2020).

Interestingly, in modern practice, ultrafast lasers generating trains of pulses of duration 100 fs or shorter are quite common and most of the relevant ways to generate terahertz transients are from optical pulses; though this preserves only a fraction of the optical bandwidth (Zhang et al., 1992). This means that it is normally true that the transform-limited pulse is perfectly suitable to sample the generated waveform (Liu et al., 2009).

Trivially (sharply differently from the practice in the optical field), once the detected field waveform is available, a numerical Fourier transform can be used to address its spectral content. This aspect also highlights one of the most distinctive aspect of TDS, which is the providing of the complex spectrum of the detected field (amplitude and phase) - quite uncommon in the standard photonics practice. This means that both the absorption and refractive index spectrum of an object can be determined by placing it between the source and detection.

The THz time-domain spectroscopy of an actual medium was first reported in the late 80s (van Exter et al., 1989) and clearly demonstrated the THz sensitivity to water vapour in air. In fact, TDS systems are often subject to unwanted environmental contributions from air water content, which presents in the spectrum as absorption peaks at specific frequencies (Nahata et al., 1996).

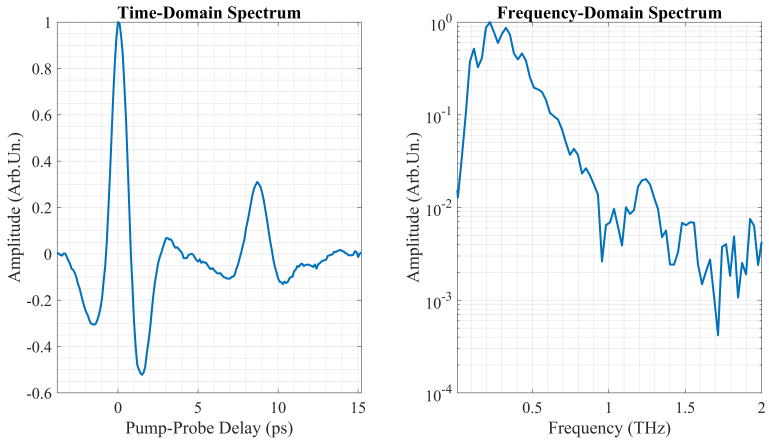

Figure 1.3: Terahertz Time domain and Frequency domain spectra taken with $LiNb0_3$ generation and detection crystals.

The Fig. 1.3 shows an example of the spectrum of a THz field transient transmitted through air. Visible notches corresponding to water absorption (at about 1 THz and 1.7 THz) are clearly visible in the pulse spectrum.

1.2 Terahertz Time-Domain Imaging

Terahertz imaging offers the benefits of Terahertz spectroscopy (Hu and Nuss, 1995) in 2-D morphological analysis and can be performed as an ultrafast time-of-flight measurement that produces a TDS for each measured pixel. Fixed-time THz images can produce biological contrast (Gente et al., 2013) datasets and profile point artefacts and defects; however scattering profiles of the THz interacting with the sample and structures are also available when a time-of-flight measurement is performed. These profiles contain complex information on the sample that can be used to infer parameters such as the 2-D distribution of the absorption coefficient and the complex refractive index (Francis et al., 2020) over the sample. The methodology, as first conceived, is analogous to confocal microscopy with sample translation. Terahertz radiation is focused with specialised optical components and the sample is placed in the focal point (Hu and Nuss, 1995). To create an image the sample can be moved through this focal point, with a TDS taken at each position. This type of image is known as a hyperspectral image because of the vast range of frequencies contained in each pixel, as opposed to a multispectral image which is usually only taken at a limited number of bands per pixel (Goetz et al., 1985) (red, green, and blue for a full-colour image). Only the former type is truly suitable for spectroscopic applications. The first example of the THz-TDS image was taken in 1995 by Hu and Nuss (1995), and interestingly was a biological image of a leaf that displayed the excellent contrast that water-containing tissues have in the THz spectrum. This methodology is, however, not the first image taken at THz frequencies - as an example, THz imaging via an interferometric setup that utilised bolometer detection was demonstrated in 1984 by Lash and Yundev (1984). Raster scanning a sample imposes limitations on the speed and resolution of the image acquisition (Cui et al., 2012), motivating the development of modern THz imaging methods to improve the applications of the field. Around the turn of the century, near-field methods (Wynne and Jaroszynski, 1999) and aperture methods for confocal microscopy (Hunsche, 1998) were introduced to THz imaging to improve the spatial resolution. A few years later large-area illumination methods (Wang et al., 2008) drastically reduced the imaging time, pushing THz microscopy closer to real-time function. In recent years, there has been much focus on applying compressive imaging methods to THz imaging; perhaps the earliest of these was a concept by Chan et al. (2008). These compressive methods generally allow for faster electrical sampling compared to ordinary synchronous sampling; perhaps they will soon allow for effective real-time THz applications.

1.2.1 Near-Field Imaging Method with Terahertz Pulses

To measure 'in the near-field' is a well established method in optical microscopy, involving imaging the field perturbations that occur close to the sample (Wynne and Jaroszynski, 1999). Though offering vastly improved image resolution when compared to confocal microscopy, it often requires little modification to adopt the changes required to allow a confocal microscope to take near-field images (Hunsche, 1998). It is therefore unsurprising that near-field imaging is often considered standard practice in the field THz imaging. To understand the motivations of near-field THz imaging it is important to first consider some of the limits that confocal microscopy can apply to the images it produces when operated in the THz domain.

Diffraction Limited Imaging

The concept of diffraction limited images refers to the nature of image reconstructed via system of limited numerical aperture where the diffraction limits our ability to represent an image, i.e. the image resolution. Although the basic elements are a already part of scholarly literature Born and Wolf (1999), it is useful to recall some key concepts as they are important in understanding the relevancy of this work. A perfect focusing system can represent the Spatial Fourier Spectrum of an impinging light wave. However, the system always samples a limited amount of the wavefront. Said differently, an impinging plane wave is actually multiplied in space by the aperture of focusing system, which alters the spatial spectrum. Because the focusing system is focusing a wavefront of limited dimension, the ability to focus it is also limited by the diffraction of the input beam. Diffraction (Fowle, 1989) takes place in any real optical system which focuses the wave to an Airy disc instead of the 2D Fourier transform shape of a periodic plane wave – a Dirac delta. This is the same as saying that the image of two distinct adjacent point sources can overlap in the image plane, making them indistinguishable.

The distance from the centre of the Airy disc to the first minimum is proportional to the wavelength of the incident light and the numerical aperture – the ratio of the lens focal length to the aperture diameter (Fowle, 1989). This can be seen in Figure 1.4. If another source is located within this radius then Rayleigh diffraction states that it cannot be resolved, as also seen in Fig. 1.4. This is the main contributing factor to 'diffraction limited resolution' and the limit itself in microscopy applications is known as the Abbe limit. This limit generally depends on the aperture width, wavelength range and bandwidth of the incident field (Siemion, 2021).

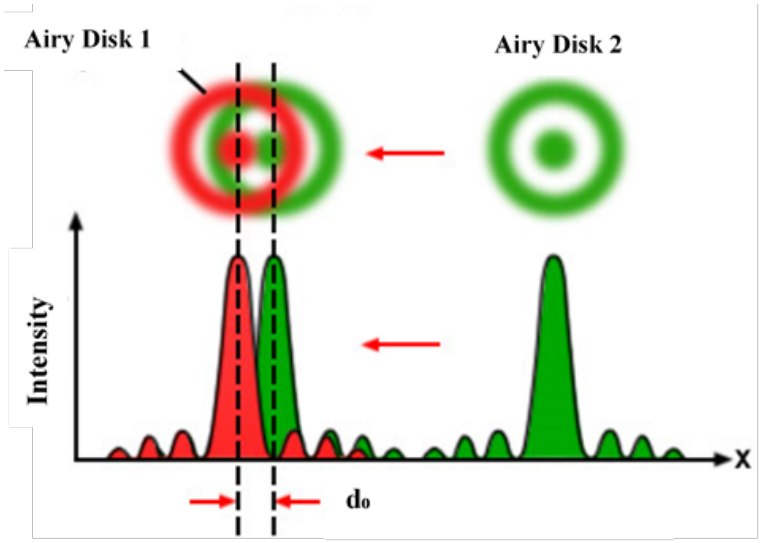

Figure 1.4: Rottenfusser et al. (2021) (left) Overlapping airy disks are just resolved when the first minimum coincide, the resolved distance is d_0 (right) A single point diffraction creates an Airy Disk.

Near Field Perturbation

Diffraction-limited imaging struggles to resolve small features either physical or in field dynamics. However, these small features can contain important sample information. In-

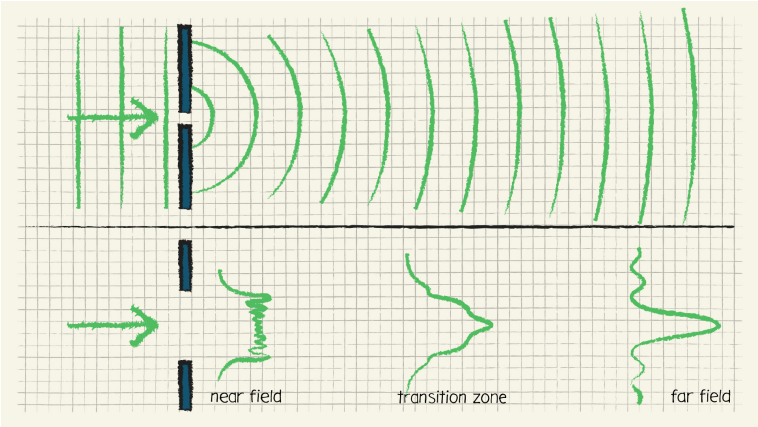

Figure 1.5: Tomandl (2021) The interaction of a plane wave with an object, in this case a slit. After some wavelengths of propagation the near field perturbations are invisible.

terestingly, when an aperture made of a perfectly shielding conducting material is placed in the path of an incident plane wave, the transmission of the wave is dependent on the size of the aperture relative to its wavelength. If the aperture (or more generally an object) is small compared to the wavelength, then any perturbation it induces in the wave will become undetectable (Fowle, 1989) after a few wavelengths' distance. This effect is

visualised in Fig 1.5.

To measure 'in the near field' is to probe the perturbation that a small object induces in a plane wave of comparable wavelength to its size (Lewis et al., 2003), which must be done close to the object. Said differently, the object can be imaged as soon as we are able to perceive the spatial perturbation of the local field.

Exceeding the Diffraction Limit in THz

Unfortunately THz radiation diffracts significantly in the far-field (Baillergeau et al., 2016) when compared to optical radiation over the same distance. The diffraction limit for THz radiation tends to be large (Lee, 2009b); it therefore makes sense that diffraction-limited THz microscopy fails to resolve small features, even when near-field perturbations are not considered. However, near field perturbations are of great interest in sample analysis because they contain information on physical phenomena occurring at the sample surface (Courjon and Bainier, 1994). Like larger features, the resolving limit of the equipment directly affects their visibility when using a microscope to attempt to measure them. An insufficient resolving limit is often expressed as a wavelength-dependent lateral resolution, either the Abbe limit or the related Rayleigh limit, that exceeds the feature size(Chen et al., 2003). If the small feature is visible then the resolving limit of the microscopy equipment can instead be expressed as better than the size of the feature's smallest dimension. There are several methods that can reduce the effects of diffraction on the resolution, and additional methods that can allow the microscope to access near field perturbations. Both of these goals, in the THz domain, have historically contributed to the development of near-field THz microscopy.

The resolution of diffraction limited imaging can be improved with an aperture (Macfaden et al., 2014), both in the optical and THz bands (Wynne and Jaroszynski, 1999). This is because the conjugate image (of a plane wave) is a point in theory (Fowle, 1989) at the focus of the confocal microscope so a circular aperture placed in this focal plane can block the diffraction rings of the Airy disc (Mitrofanov, 2000) formed in experiment. However, a small aperture decreases the transmitted field especially when it is smaller than the wavelength (Mitrofanov et al., 2001). This means that although an aperture is an effective method of image improvement the aperture size cannot be reduced indefinitely to increase THz resolution. The aperture can filter lower frequencies because the cut-off frequency of the field modes that can be transmitted through it is inversely proportional (Macfaden et al., 2014) to its diameter. The sub-wavelength aperture also allows for near-

field access by scattering the evanescent field component (Hunsche, 1998) at the sample, allowing for limited sensing of the phenomena at the sample. This scattering methodology was well established in optical near-field imaging (Greffet and Carminati, 1997) and was often performed with an Atomic Force Microscopy cantilever tip scatterer (Zenhausern et al., 1994) or even optical fibre tip (Lewis and Lieberman, 1991), itself acting as an optical source or detector. These sub-wavelength tips are placed close to the sample. Placing objects close to the emitter or detector allows the near-field perturbations in the THz domain to be sampled directly as well (Federici et al., 2002); this placement is often combined with focusing optics to increase the peak THz field at the sample. Often a focused probing pulse is used to sample the region or alternately a focused optical pulse at the THz generation plane (Wang et al., 2004). This pulse can emulate the effects of a real aperture (Chen et al., 2000) on the image. (Mitrofanov, 2000). To maximise the resolution of a near field measurement the active region of the detector(Lai et al., 2015) must be small. This can be achieved by not only using a tightly focused incident pulse but also a thin detector region (Blanchard et al., 2011).

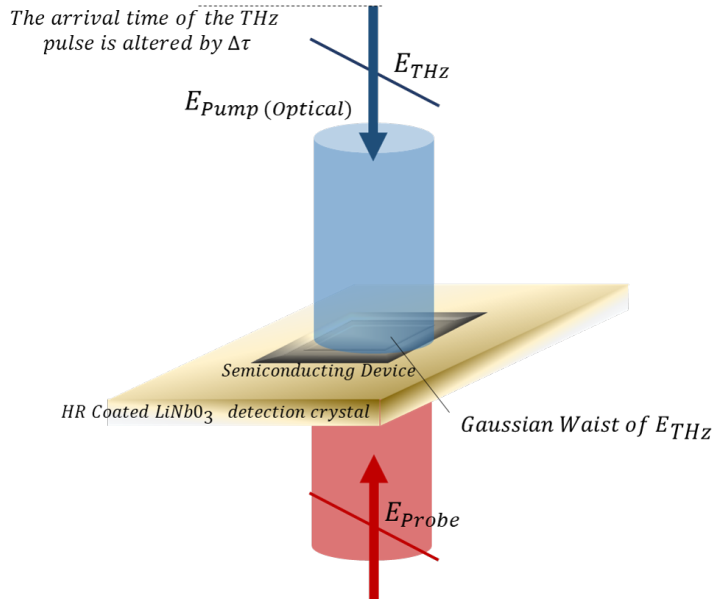

Figure 1.6: A method of near field Terahertz Imaging involves placement of the sample semiconducting device on a detector.

One form of this popular method is visualised in Fig. 1.6, where the detector - a large-area electro-optic crystal - contacts a sample at the THz focus (Blanchard et al., 2011). The probing pulse, incident on a detection crystal can act as an aperture generating a local polarisation 'pulse' – (a changing polarisation density) (Wang et al., 2010) which interacts with the polarisation rotation caused by the incident THz. The implementation of near

field-imaging by bringing the emitter into contact with a sample (Wynne and Jaroszynski, 1999) is an equivalently effective method (Courjon and Bainier, 1994), provided that the active area of the source is sufficiently small compared to the wavelength of the radiation (Lecaque et al., 2011), allowing the emission source to act as the aperture. A good example of such a source is a femtosecond laser focused onto a nonlinear quadratic crystal, generating THz radiation by optical rectification (Rice et al., 1994), or onto a narrow bandgap semiconductor (Peters et al., 2017) producing THz by carrier acceleration. To obtain a two-dimensional THz image the THz field detected with a large-area detection can be imaged with a pixel array and a set of imaging optics (Blanchard et al., 2011). The large area of high-strength optical-to-THz conversion probed with a focused pulse and imaged onto the pixel array allows the pixel to act as the minimum probing aperture, leading to maximised THz lateral resolution. The development of the near-field method is complex but after many iterations the technology has developed and progressed in an attempt to meet the maturity of optical near-field imaging technology.

1.2.2 Compressive Imaging

As previously mentioned, the fundamental form of imaging based on single-pixel detection is the raster-scan approach, which generally involves lateral translation of the sample in respect to focal point, aperture, or other spatial sampling technique. This is also true for THz-TDS system as most commercial embodiments allow the retrieval of the time-domain spectrum of each point of an object via scanning. As most common TDS approaches require seconds or fraction of seconds for the extraction of a single waveform, normally dictated by the system signal-to-noise ratio, raster-scans are also possibly the slowest solution in the field (Hu and Nuss, 1995), and scale badly on large surfaces (Chan et al., 2008). The extremely long acquisition time was a major motivation in the adoption of compressive imaging techniques into the field of THz imaging, in which the challenge of achieving effective real-time imaging still exists today.

Compressive sensing is a domain that investigates ways to reduce the amount of meaningful information content to represent an image. In an experimental setting, this corresponds to performing fewer measurements than the number of pixels (Augustin et al., 2018). For the sake of historic accuracy, compressive imaging in the optical domain has a background that spans more then a century and vastly predates pixel arrays. Perhaps the first popular embodiment and early example of compressive imaging has been reported by Prof. Arthur Korn (Times, 1907) where an image was transmitted by telegraph

encoding and the varying intensity profile was obtained through a revolving drum with apertures. The detector in this case was a galvanometer with a similar drum and provided a true method of single pixel detection that produces a line-by-line image. The method of encoding with a spinning Nipkow disk (a disk with multiple carefully placed apertures seen in Fig.1.7) was behind the first television and even predated the demonstration of a prototype by Korn (Shiers, 1997).

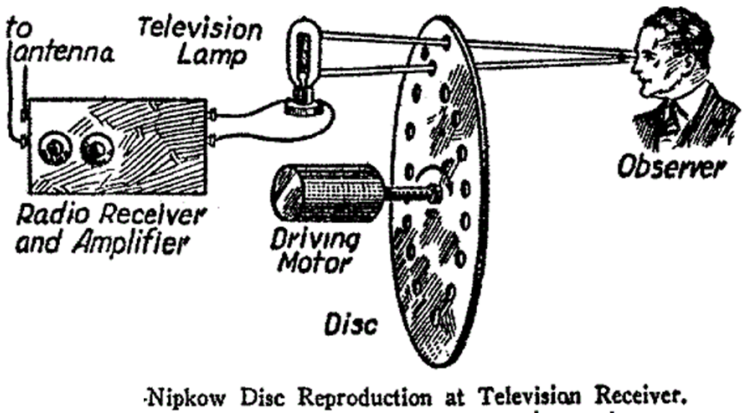

Figure 1.7: Manly and Gorder (1951) A setup allowing the Nipkow Disk to act as an image receiver, encoding the images line-by-line to the output screen, in this case labelled 'Observer'.

Actually, this type of imaging approach is quite relevant to modern approaches requiring a 'dynamic aperture', as the Nipkow Disc acts as a spatial light modulator (SLM). The SLM encodes a 'pattern' or 'mask' into the beam, applying an intensity or phase map (Shrekenhamer et al., 2013) that can be projected onto the object. A set of patterns can be chosen to 'encode' the full set of pixels, and the image can be reconstructed by solving a linear combinatory equation (Chan et al., 2008). Thinking outside the pixel-by-pixel description, we can consider the sampling to occur over the momentum space (k-space) (Hu et al., 2019) as the pattern samples the spatial impulse response via a sum of plane waves with different wavevectors. Here the necessary condition for the image reconstruction is the coverage of a sufficiently large k-space, imposed by the Nyquist -Shannon sampling (Weingarten et al., 1988). The image matrix can be assumed to be sparse to reduce the computational power required for the reconstruction (Augustin et al., 2018). The reconstruction problem is ill-conditioned under this assumption and has no exact solution when there are fewer patterns than pixels (Jiang et al., 2021), but an approximate one can be found when utilising an appropriate choice of masks with known transmission functions. This enables the reconstruction of a modern computational 'compressive image' which is

the numerical solution to the posed reconstruction issue. Compressive imaging as applied to the experimental extraction of images is normally referred as 'computational imaging' when deterministic masks are used to encode the beam (Gibson et al., 2020). Interestingly, this form of imaging can operate with random patterns (for example originating from specific physical mechanisms), although the low-relative orthogonality of the patterns implies a much larger number of illumnations.

To achieve deterministic light encoding spatial light modulators or dynamic mirror devices (Chan et al., 2008) are widely available photonics devices (at the basis of many modern image projectors).

The image can be reconstructed by performing a summation of iterative images where each is a calculated field intensity at the object plane (Shapiro and Boyd, 2012); an intensity that is correlated with the measured intensity at the single-pixel detector that corresponds to the beam overlap of the mask and object transmission. Because the trans-

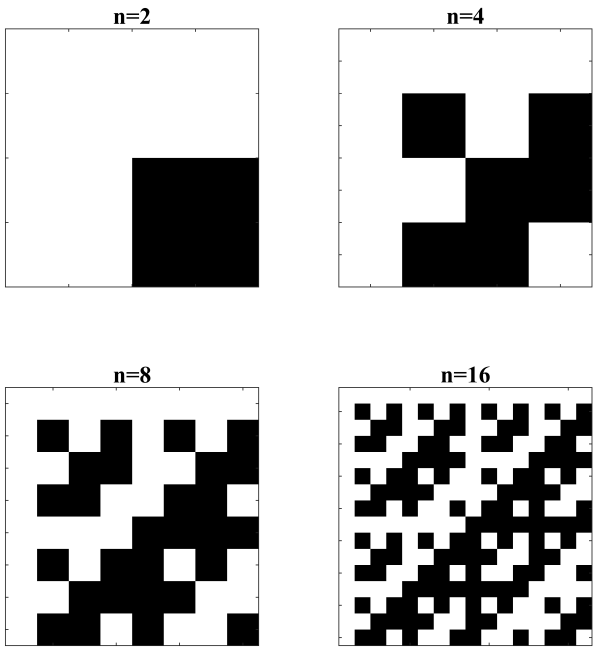

Figure 1.8: Hawes (2015) The first four orders of Hadamard matrices, generated by algorithm from the lowest order matrix which solves Hadamard's determinant problem.

mission function of the masks is directly used when computing the solution to the matrix equation the type of mask chosen affects signal-to-noise ratio, resolution, and computation speed (Augustin et al., 2018). A mask can have two major characterising properties – binary/greyscale, and random/deterministic (Wei et al., 2020) that are intrinsic to its

make-up. A random mask could be rotating ground glass that produces pseudo-thermal light. A binary mask only has 'black' and 'white' pixels like a multiplicative matrix containing only 0 or 1, whereas a greyscale mask can have any number of possible values. A binary mask, for example the deterministic Hadamard mask or the (pseudo-) random Bernoulli mask, has the advantage of each pixel being either fully- transmissive or non-transmissive (Gibson et al., 2020); this can ease the determination of the transmission function as there are many vanishing elements. A greyscale mask for THz radiation is very difficult to implement in experiment (Augustin et al., 2018) but can in theory offer a greater bit-depth for sample encoding. The ordering of masks has a significant effect on the quality of the reconstructed image (Vaz et al., 2020), but the most effective ordering algorithm depends on the level of compression that the reconstruction uses.

1.2.3 Ghost Imaging

Ghost imaging (GI) has a history in optics that is linked experimentally with the demonstration of a thought experiment that was designed to challenge the uncertainty principle (Kim and Shih, 1999) - Popper's experiment. Popper believed that correlation in entangled photons allows for the precise determination of one photon's position and momentum through interference when the other is measured.

Though many iterations of GI have been reported, the optical setup (Pittman et al., 1995) measured the correlation signal between two entangled photons measured with distant bucket detectors. One photon passes through a sample causing a correlation signal in the other bucket detector as the sample is moved. Strangely, this phenomenon can be observed in the classical domain despite the entangled state being indescribable classically (Shapiro and Boyd, 2012) when the two photons are classically correlated. This correlation can be induced by transmitting light through rotating ground glass or another objects that induces an intensity pattern; subsequently one photon will pass through an object to a bucket detector and the other will have its intensity profile scanned. This particular measurement can be performed as a computational image with one bucket detector (Shapiro, 2008) if the intensity profile can be pre-determined, and therefore the phenomenon cannot be dependent on the non-local two-photon interference that defined the entangled photons' behaviour. The single bucket detector is what enables the Ghost image to be referred to as a single-pixel image. The field of ghost imaging, while fairly recent, has already demonstrated the intriguing power of classical spatial correlation. Ghost imaging has been demonstrated with a range of photon wavelengths (Gibson et al., 2020), and un-

surprisingly was proposed in the Terahertz domain shortly after the initial demonstrations of computational ghost imaging methodologies (Chan et al., 2008). Its demonstration in the Terahertz domain was eventually performed by Stantchev et al. (2016) and (Olivieri et al., 2018), utilising different methodologies, providing hyperspectral measurements of objects' field interaction along with morphological analysis. Time-domain THz images tend to consist of large array data sets, and the possibility of utilising compressed sensing with GI allows for the image set to be undersampled, drastically reducing the measurement time for this type of dataset. In both the optical and Terahertz domains the methodology is capable of spatially resolving hidden objects - objects that are completely concealed from modes of morphological feature detection (Shapiro, 2008) - despite only measuring the object interaction with a single pixel detector. With no imaging optics or spatial detector required, the prospect of GI as a single-pixel lensless imaging mode (Chen et al., 2009) indicates suitability for a much wider range of applications than any standard imaging. This is especially true outside of the field of optics, where bulky and delicate spatial detection setups are an inconvenience. However, when a THz imaging application requires a large number of TDS pixels in the set there are far quicker methods available, such as the parallel imaging method described in Fig. 1.6.

1.3 Optical Pulses and Matter

A distinctive aspect in optical absorption is the relatively high energy of involved photons when compared to terahertz photons. This is very important because in many substances, photons promotes carriers in to higher free-energy states (Fowle, 1989). Hence, while using optical photons is indeed an appropriate way to probe quantum transition-mediated absorption processes, we can argue that the access to other mechanism like free-electron absorption in dielectrics can be understandably inhibited by the photon energy. Said differently, probing using optical photons inherently alter the free-electron dynamics.

THz radiation offers a low-energy, classical interaction that is incapable of exciting the inter-band transitions that free carriers by absorption of optical radiation. The processes described in the later sections can be sensed with THz radiation (Joyce et al., 2018) which reveals crucial details about their complex properties (Afalla et al., 2019).

1.3.1 Material Classifications

Material interactions have always been a significant consideration in nonlinear optics; quantum interactions are difficult to observe and quantify therefore research often focuses

on measuring bulk effects. Basic solid state theory is largely sufficient to describe the processes of concern in this thesis - processes where energy is transferred between photon pulses and material carriers. There are many materials that could be considered to have interesting electronic properties, but due to the band structure and band gap properties it is semiconductors that were the focus of the experiments described in later chapters. Individual atoms and molecules posses energy levels - states in which electrons can reside stably - that are characteristic to them. Therefore it makes sense that any system that they are part of has a characteristic band structure. In a material this is often assumed to be spatially homogeneous, though unfortunately this assumption doesn't hold at the surface or at impurities. Because of this, a material's electronic properties can be subject to change depending on a variety of parameters. To recap, and following the argument by Ashcroft and Mermin (1976), the gap between the highest occupied level and the lowest unoccupied level is the band gap, where bands are occupied at room temperature up to the Fermi Level. The bands situated around the Fermi level are the valence (lower) and conduction (upper) bands. Carriers in the conduction band can contribute to the material conductivity.

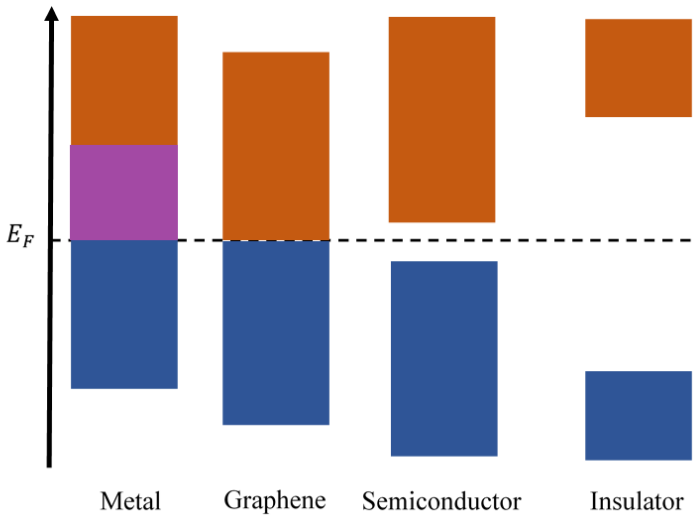

Figure 1.9: An illustration of energy bands and their relation to the Fermi Level.

The Fig. 1.9 shows the basic definitions that are utilised in this thesis for material classification, and the relation of the Fermi level to the bandgap. Large-bandgap materials like the insulator are transparent to lower energy photons and often specialist equipment is required to access their conduction properties. In the metal, the Fermi Level lies within a band and thus at room temperature the energetic carriers can be subject to a thermalisation process that is later explored in detail. Semiconductors, in this thesis, have

a bandgap that is around 2 eV and can be excited by photons within the near-infrared range. They then exhibit metallic behaviour after absorption that can be measured with THz radiation.

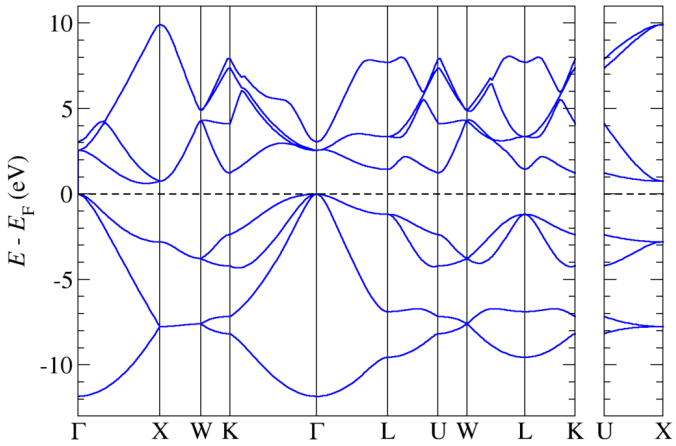

Figure 1.10: Parker (2012) The band structure of Silicon as generated from the Local Density Approximation The x-axis values are vector paths within the first Brillouin zone.

Figure 1.10 is a calculated band structure for silicon, representing an actual momentum-energy description of the bulk material (Parker, 2012). This particular material is a standard semiconductor used in electronic devices and is utilised in experiment in later chapters.

1.3.2 Carriers in Semiconductors

The energy of the absorbed photon can be spontaneously emitted from an excited system as a photon of energy $\hbar\omega$ (Rossler, 2009). In response to the impulse excitation this spontaneous emission has a temporal decay that equates to the characteristic lifetime of the excited level (Agarwal, 1975). Alternatively the recombination process can distribute energy through phononic interaction, or by interaction with a third carrier or trap centre (Bullis and Huff, 1996). The carrier recombines with the valence band and an electron and hole are exchanged again. This absorption and recombination is one of the basic carrier dynamic processes that is explored in this thesis.

The incidence of an ultrafast laser pulse upon a semiconductor creates a metallic region of hot carriers. The contribution of the hot carrier density to the medium's dielectric properties is rather complex, but its decay alters the conductivity. The dynamics of the

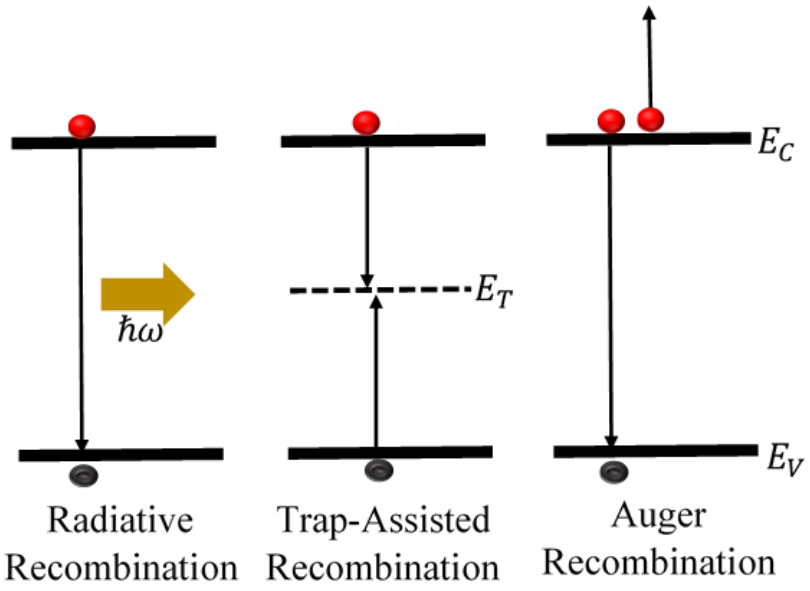

Figure 1.11: In radiative recombination an excited electron recombines with a hole in the valence band, releasing a photon. In trap-assisted recombination the electron and hole recombine at a trap-level, dissipating energy via phonons. In Auger recombination an excited electron recombines with a hole in the valence band, transferring energy to another excited electron.

conductivity can then reveal the recombination mechanisms that typically occur in the medium(Bullis and Huff, 1996). The processes seen in Fig. 1.11 are common recombination mechanisms seen in semiconductors (Rossler, 2009).

The measurement of this type of decay is known as transient carrier spectroscopy (Balland et al., 1986). When using certain techniques, including THz probing, (Kar et al., 2018) the form of the complex dielectric function can be unveiled too, which contains important information that can be used to predict the function of devices containing the material. Recombination effects seen in transient carrier measurements can be characterised as either surface or bulk depending (Heinz et al., 2017) on whether they can only occur within the small depth of material that the excitation field can penetrate or solely on the surface where there is a material boundary. Effects such as surface recombination can have a significant influence on the transient lifetime (Linnros, 1998) as does surface treatment and defects (Heinz et al., 2017); these are surface effects. Bulk effects include doping and impurities. If materials are layered with each other there can be further effects as energy is transferred between material layers and carriers diffuse (Proctor et al., 2013). This can cause multi-layer material samples to produce unusual transients (Kar et al.,

2018) when carrier spectroscopy is performed, provided the sample layer is sufficiently thin for the carrier diffusion process to occur. If the dielectric function of a material is known then new applications and devices can be proposed. There are a few popular device combinations that benefit from information on the material conductivity and involve interplay between the carrier-field dynamics of different materials. Doped semiconductors have different conductivity properties due to impurities (Sah et al., 1957), and the junction between different doping regions - the p-n junction - has special properties (Smith et al., 2018). Trapping and recombination between holes, electrons and the trap levels causes 2 currents: the drift current and the diffusion current that flow in different directions when part of a circuit. Because such a junction can only be manufactured through specialised processes, the conductivity properties of the material and dopant should be pre-estimated. A transient carrier measurement for each material is crucial in this case. This information can be used to model the conductivity properties of different regions across the p-n junction and aid in the estimation of the drift and diffusion currents. When operated in reverse bias, the mode in which current doesn't naturally flow through the carrier depleted central region (Mao et al., 2017) in it's resting state, the diode can generate current from optical absorption. This device is known as a solar diode, and its properties are based on the size of the depleted region (Proctor et al., 2013). Transient carrier spectroscopy can easily identify these depleted regions, again giving insight into the junction operations. This can be especially useful for more complex junctions and diodes that can consist of multiple doped layers and depleted regions. The premise of performing carrier spectroscopy on a multi-composite device is explored experimentally later on in the text.

1.4 About this Thesis

This thesis will introduce the reader to the field of Terahertz Imaging which lies within the larger discipline of nonlinear optics - a subset of the photonics methods used in modern research. The introduction has served as a background and the next chapter, Chapter 2, offers deeper technical insight into the processes that are crucial to this work. These include nonlinear field interactions, ultrashort pulses, optical rectification, and the electro-optic sampling process. The subsequent chapters contain practical and technical descriptions and results regarding the successful implementation of novel techniques; Chapter 3 presents what has been the central result of my PhD endeavour, which is the conception of an ultrafast Hot-Carrier Microscopy based on terahertz waves, which was largely my own work. Chapter 4 covers a novel and influential imaging methodology developed in the

deployment of this PhD work, the Nonlinear Ghost Imaging. I stress here that while my specific contribution to this technique is within the experimental implementation in a much larger team-work, the chapter will guide the reader through the background, the conception, the theory and the experimental results. Chapter 5 features a final reflection on work, its impact and also a reflection on my general experience during the development of my PhD a truly fun, inspirational and welcoming part of my career. In that, there is my hope that bits of wisdom (if any) could serve the next generation of PhD students.

Chapter 2

Methods in Terahertz Generation and Detection

Since its generation became possible in small-scale laboratories (Auston et al., 1980) the field of THz radiation has been evolving in steps that mark the development of crucial new methodologies. This chapter is about optical methodologies that were used in this work, methodologies which mainly concern the generation and detection of THz radiation. This includes some of the fundamental mathematical descriptions of photonics as well as justifications for the parameters that are linked via fundamental relations. The background of these methodologies can be complex and thus the descriptions in this thesis should not be considered exhaustive, however they are sufficient to cover the necessary background.

2.1 Optical Methods for Terahertz Generation

Terahertz generation technology has improved in recent years (Mittleman, 2017), (Papaioannou and Beigang, 2021) and now consists of a wide range of technologies; from ready-to-buy Continuous-Wave (CW) sources such as the Backward-wave Oscillator (Dayton et al., 1987) to ultrafast sources like the wide-aperture photoconductive antenna (Fattinger and Grischkowsky, 1988). This thesis will focus on the utilisation of nonlinear quadratic crystals to generate THz radiation via optical rectification for multiple practical reasons. Indeed, at the basis there is the need to operate with wide-bandwidth pulses to achieve the time-domain imaging targeted by this work. However, when compared to alternative technology, the combination of nonlinear crystals with high-energy ultrafast laser is a very accessible route to obtain the high terahertz fluence requires to illuminate relatively large targeted areas.

2.1.1 Ultrashort Pulses

Because of the inherently low conversion efficiency that characterises terahertz generation, high power ultrashort laser pulses are a general requirement for large area illuminations. A mode-locked regenerative amplifier (Regen) (Murray and Lowdermilk, 1980) is used to produce these pulses which are of millijoule energy, Gaussian in shape, and as transform limited pulses are well confined (Curley and Ferguson, 1991) in the frequency and time domain. The creation of this sort of pulse first occurred decades ago by a process called Chirped Pulse Amplification (CPA) (Strickland and Mourou, 1985) that was designed to increase the maximum field amplitude of the Regen pulse; this work later won the Nobel prize in Physics.

2.1.2 Nonlinear Optical Mechanisms

The term *nonlinear optics*, refers to the general observation that in a medium the polarisation field is in general non-linearly related to an exciting electric field. This means that assuming the relation between the medium polarisation density and the local electric field as $\tilde{P}(t) = \epsilon_0 \chi \tilde{E(t)}$, that susceptibility tensor χ also exhibits a dependence from the electric field. While this is a condition in most frameworks, nonlinear products are generally visible only for significantly large fields (Boyd, 2003). Because of the relatively high instantaneous electric field expressed in ultrashort pulses, they are a common means to excite significant electromagnetic nonlinear products. Relevant to this thesis, ultrafast electronic nonlinearities, i.e. nonlinear mechanism driven by a non-elastic displacement of the electrons bounded to atoms, are generally perturbative. This means that that susceptibility tensor can be expanded in a power series (Boyd (2003)). In a scalar representation for fields, this results in a standard expression for the polarisation density field

$$\tilde{P}(t) = \epsilon_0 \chi^{(1)} E(t) + \epsilon_0 \chi^{(2)} E^2(t) + \epsilon_0 \chi^{(3)} E^3(t) + ... \tag{2.1}$$

$$\tilde{P}(t) \equiv \tilde{P}^{(1)}(t) + \tilde{P}^{(2)}(t) + \tilde{P}^{(3)}(t) + ... \tag{2.2}$$

Interestingly, many optical materials exhibit microscopic inversion symmetry at atomic level. Because the polarisation must (Ito et al., 1975) preserve the electric field sign, this means that odd order susceptibility are in general vanishingly low. Conversely *quadratic* nonlinear crystals, as the typical media exploited for optical rectification, exhibit a very pronounced microscopic crystalline symmetry breaking, resulting in the $\chi^{(2)}$ being the sole most relevant contributor to the nonlinear polarisation response. Assuming a propagating

monochromatic we cast the identities

$$\tilde{E}(t) = Ee^{(-i\omega t)} + E^* e^{(i\omega t)} \tag{2.3}$$

$$\tilde{E}^2(t) = EE^* + E^*E + E^2 e^{(-2i\omega t)} + E^{*2} e^{(2i\omega t)} \tag{2.4}$$

We can observe that the quadratic product implies that resulting polarisation contains a static zero frequency component and a frequency doubled component.

The frequency doubling effect can be seen in the case of Lithium Niobate, where a pronounced blue beam is produced from the nonlinear conversion of an 800 nm pulse. This intense Second Harmonic generation is in this case an unintended effect.

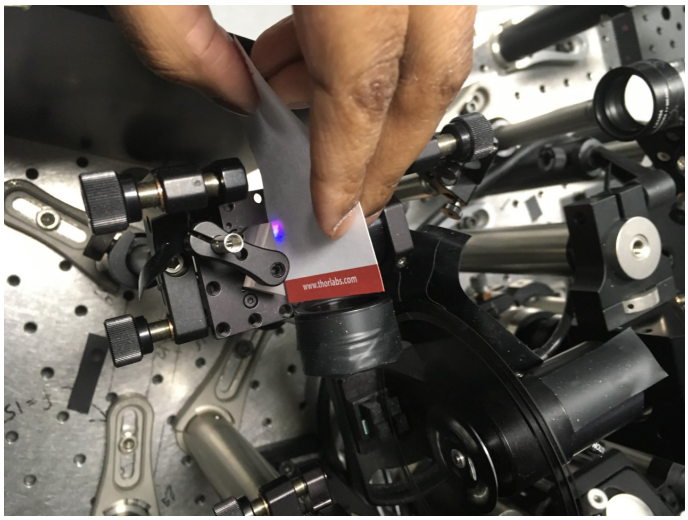

Figure 2.1: An image of the second harmonic of an 800 nm excitation of a prism-cut Lithium Niobate crystal.

The resulting static polarisation component

$$\tilde{P}(t) = \epsilon_0 \chi^{(2)} EE^* + c.c \tag{2.5}$$

is at the origin of the terahertz generation. This can be appreciated considering the multiple frequency components ω_j that make up the electric field spectrum of an ultrashort pulse. Focusing on the interaction between photons at frequencies ω_1 and ω_2 we can write the nonlinear polarisation product as

$$\tilde{E}(t) = E_1 e^{(-i\omega_1 t)} + E_1^* e^{(i\omega_1 t)} + E_2 e^{(-i\omega_2 t)} + E_2^* e^{(i\omega_2 t)} \tag{2.6}$$

$$\begin{aligned}\tilde{E}^2(t) =& E_1^2 e^{-i2\omega_1 t} + E_2^2 e^{-i2\omega_2 t} + (E_1 E_2 + E_2 E_1) e^{(-i(\omega_1+\omega_2)t)} + \\ & (E_2 E_1^* + E_1^* E_2) e^{(i(\omega_1-\omega_2)t)} + E_1 E_1^* + E_2 E_2^* + c.c\end{aligned} \tag{2.7}$$

This implies the existence of three distinct frequency transformations in the polarisation density that are source of electromagnetic field: $\omega_i \rightarrow 2\omega_i$, $\omega \rightarrow \omega_i - \omega_j$, $\omega \rightarrow \omega_i + \omega_j$,

These processes are the commonly referred to as Second Harmonic Generation (SHG), Difference Frequency Generation (DFG), Sum-Frequency Generation (SFG). The remaining terms are static field components that do not propagate. Because of the typical bandwidth of ultrafast pulses, the oscillation frequency of the DFG term is in the order of the THz scale. Hence, this term is the common source of the THz radiation and the all process takes the name of optical rectification (OR) when excited from a single optical pulse. They are known as second-order parametric processes, as the system preserves its quantum state after a 'three photon' interaction, represented in fig 2.2. The system in the Fig 2.2 comprises an initial state and virtual excited states. In these lossless processes frequency is transformed with proportionality to $\chi^{(2)}$. In the SHG process, two low energy photons with identical frequency interact within the material and are transformed into one high energy photon with a doubled frequency. Similarly in SFG, two non-identical photons interact and are transformed into a single photon with a frequency that is the sum of that of its constituent parts. DFG is a process wherein one photon can excite the material to virtual state, then decay emitting two photons.

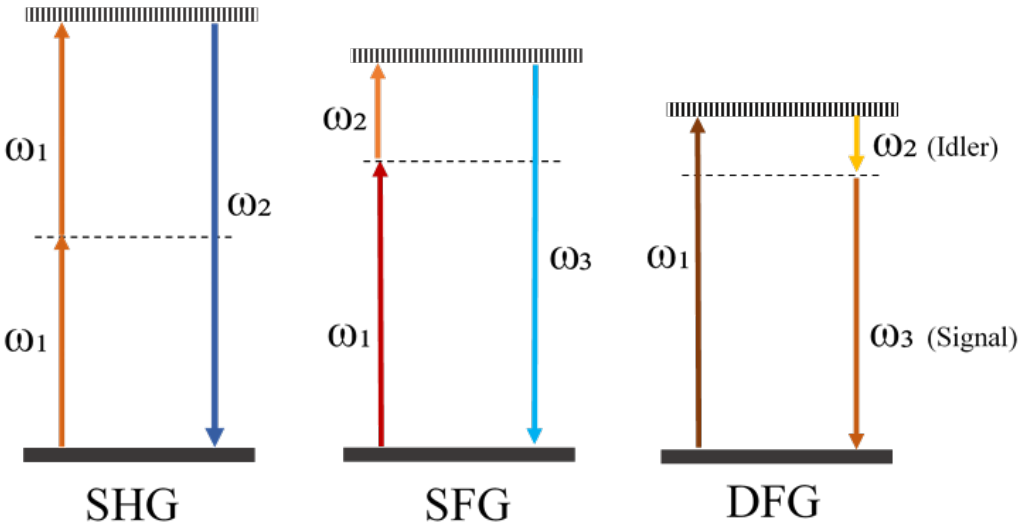

Figure 2.2: Illustration of the processes of Second Harmonic Generation, Sum Frequency Generation and Difference Frequency Generation. The dashed lines represent virtual energy levels.

Interestingly, the way the system exhibits inversion symmetry affects which process can be observed and in what specific propagation geometry. In fact, optical rectification is

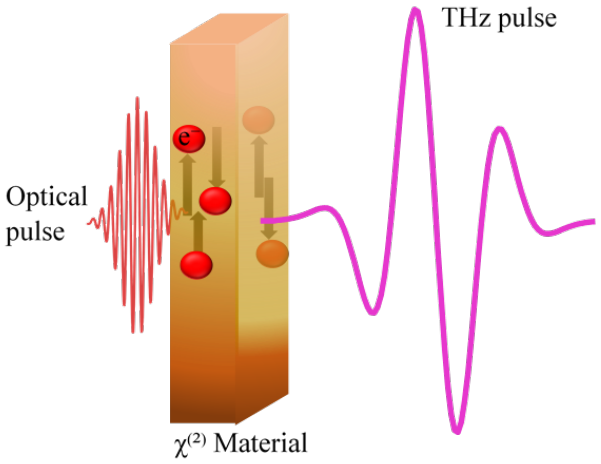

Figure 2.3: Illustration of an optical pulse causing an electronic transient while passing through a nonlinear quadratic crystal. Low frequency radiation in the THz region is produced as the optical pulse passes through.

often not allowed for propagation along crystal axes (Wyncke and Brehat, 1989). Changing the axis of transmission (Auston, 1983), or changing the desired propagation geometry to a non collinear type (Suizu et al., 2009), is used to circumvent these issues.

If all requirements are met then the optical pulse causes a changing polarisation density Bass et al. (1962), where energy is transferred to the material lattice and partial excitation and relaxation occurs due to the incidence of energy in the short wavepacket and its creation of a dipole distributed electronic transient (Rice et al., 1994). Ultrafast (or ultrashort) pulses are clearly better suited for this application than CW lasers due to the available instantaneous energy; CW lasers are inherently inappropriate for THz OR applications. The OR process is illustrated in Fig 2.3. To describe the optical rectification process it is important to consider the wavepacket itself to determine the nature of the polarisation created in the system. The wavepacket is considered to have a finite range of frequencies distributed around a central wavelength. Following the argument by Schneider et al. (2006) the polarisation created can be described by

$$P_i(\Omega) = \epsilon_0 \int_{\omega_0-\delta\omega/2}^{\omega_0+\delta\omega/2} d_{ijk}(-\Omega;\omega+\Omega;-\omega) \times E_j(\omega+\Omega)E_k^*(\omega)d(\omega) \tag{2.8}$$

where ω_0 is the central frequency of the optical pulse, $\delta\omega$ is its bandwidth, Ω is the frequency and d_{ijk} is the relevant element of the $\chi^{(2)}$ for collinear transmission at a selected material lattice rotation. The Fourier transformed elements of the electric field are $E_j(\omega+\Omega)$ and $E_k^*(\omega)$.

Because the nonlinear susceptibility tensor (Boyd, 2003) many repeating or empty

entries, the term $\chi^{(2)}$ with frequency dependence can usually be substituted for a scalar matching the desired element χ^{OR} (Ito et al., 1975). For a zinc-blende crystal this integral can be expressed in terms of the rotation angle around the axis of field propagation (Rice et al., 1994). The field emission strength is dependent on the axial angle with respect to the propagation direction.

The electric field that corresponds to this polarisation can be found analytically but is beyond the scope of this thesis.

2.1.3 Phase Matching

Momentum conservation in nonlinear processes is related to wavevector (Boyd, 2003) matching between the input and output photons of a single parametric process. For example, an SHG process will hold Wyncke and Brehat (1989) a requirement of $k^{2\omega} = k_1^{\omega} + k_2^{\omega}$ between photons 1 and 2, which have the same frequency. In optical rectification the phase matching can be basically stated as that of a DFG process (Schneider et al., 2006)

$$k(\omega_{optical} - \omega_{THz}) = k(\omega_{optical}) - k(\omega_{THz}) \tag{2.9}$$

The phase matching occurs between three frequency elements of the optical pulse where the THz is the 'signal' and the idler is the unwanted optical frequency component ($\omega_{optical} - \omega_{THz}$). This implies that THz generation by optical rectification has a limited efficiency (Yeh et al., 2007). The phase matching geometry is shown in parts (a) of Fig. 2.4. In practise, the issue of defining this scheme will depend on the isotropy Fiore et al. (1998) of the medium, which describes the symmetry of the interacting optical system. The momentum conservation inside the crystal often implies that different pulse elements have different phase velocities, which limits phase-matched nonlinear quadratic effects to anisotropic systems. For parametric processes, Type 1 phase matching allows frequency element 1 and 2 to have parallel polarisations and Type 2 allows them to have orthogonal polarisations Ito et al. (1975). When considering a THz DFG process, broadband phase matching maximises the conversion efficiency of OR processes across the frequency elements of the interacting system. In order to find this maximal efficiency the medium thickness must be limited to allow for absorptive effects. This concept can be visualised by considering the 1-D nonlinear wave equation in a material under excitation of a linearly polarised pulse

$$\begin{aligned} \frac{\partial E(\omega)}{\partial z} + \left[\frac{\omega^2 n^2(\omega)}{c^2} - i\omega\mu_0\sigma(\omega)\right] E = \\ -\omega^2\mu_0 \frac{\chi^{OR}(\omega;\omega_0)}{n(\omega_0)c} exp[-i(\omega n_g/c)z] exp(-\alpha_0 z) I_0(\omega), \end{aligned} \tag{2.10}$$

where α_0 is the absorption coefficient at ω_0, $n(\omega)$ is the phase index (of the THz) and n_g is the group index of the optical pulse, I_0 is the input pulse shape at frequency ω, μ_0 is the permeability of free space, z is the distance in the direction of the pulse propagation, c is the speed of light, χ^{OR} is the relevant element of the nonlinear susceptibility tensor, and σ is the conductivity at ω.

The generation length L_{gen} (Schneider et al., 2006) is the absolute value of the solution to the nonlinear wave equation of the rectified field and is a measure of the process efficiency in the direction of the pulse wavevector, z,

$$L_{gen}(\omega, z) = \left(\frac{\exp\left[-\alpha_T(\omega)z\right] + \exp\left(-2\alpha_0 z\right) - 2\exp\{-[\alpha_T(\omega)/2 + \alpha_0]z\}\cos\{\frac{\omega}{c}[n(\omega) - n_g]z\}}{[\frac{\alpha_T(\omega)}{2} - \alpha_0]^2 + \frac{\omega}{c}^2[n(\omega) - n_g]^2} \right)^{1/2} \tag{2.11}$$

where α_T is the absorption coefficient of the THz in the medium. This expression shows explicitly that the group index of the optical pulse must match the phase index of the THz pulse to maximise the expression for each element of the input frequency packet of ω.

2.1.4 Cherenkov Phase Matching

In order to maximise the efficiency of the OR process it is crucial to ensure that wide-band phase matching can occur(Suizu et al., 2009). The usual scheme for phase matching in a nonlinear quadratic crystal is collinear, which means that the pump wavevector and the THz wavevector are parallel. As seen in Fig 2.4, the momentum conservation can be

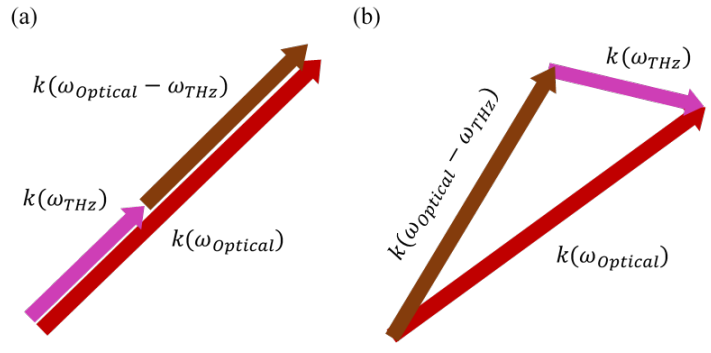

Figure 2.4: Two Phase Matching Schemes (a) A collinear scheme. (b) A non-collinear scheme.

achieved using non-collinear propagation of the interacting field. This is subject to the relevant $\chi^{(2)}$ element for the optical geometric arrangement to be non-zero. Historically,

as ultrashort pulses became shorter and shorter due to the improvement of mode-locked lasers, physicists sought to understand the effects of increasingly short electric field transients (Pessot et al., 1987) travelling though bulk crystals. Early on it was demonstrated Auston (1983) that the ultrashort polarisation transient caused by the incident pulse would radiate energy in a cone of plane wave frequencies much like an electron travelling at optical speeds in a material. This is because velocity matching in the system ensures that the DFG emission is excited as an off-axis propagating wave that constructively interferes in the direction of the Cherenkov angle. The matching condition requires the projection of the THz velocity on the optical propagation to be the same. As illustrated in Fig 2.5, the Cherenkov radiation (named after the analogous effect in electrons) is emitted from a $\chi^{(2)}$ material by an optical rectification process. The angle of the wavefront is the Cherenkov

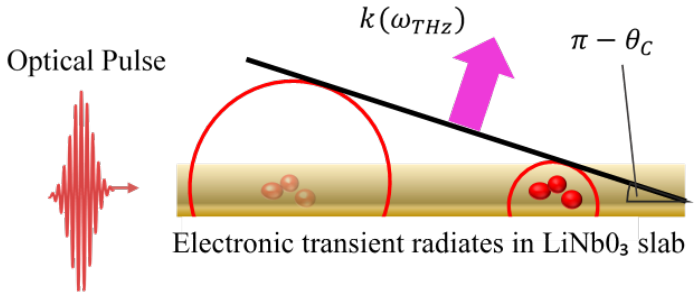

Figure 2.5: Cherenkov radiation emitted at the Cherenkov angle Θ_C.

angle Θ_C, can be expressed as Hirori et al. (2011)

$$\Theta_C = \gamma = \arccos \frac{n_g}{n_\omega} \tag{2.12}$$

where ω is the THz frequency. The emission is radial about the propagation axis and fully three-dimensional Auston et al. (1984). This means that the cut, size, and rotation of the crystal are the crucial element in directing the THz (Hirori et al., 2011), forming a stable planar wavefront, and allowing absorption to diminish the THz moving in unwanted directions through the crystal. For the purpose of non-collinear THz generation the nonlinear crystal is often prism-cut or prism-coupled (Tani et al., 2011); these diffractive elements are designed to allow for plane wave emission of the THz wave from the crystal facet. Selecting a prism-cut crystal cannot cause broadband phase matching or increase the Cherenkov generation efficiency.

2.1.5 Tilted Pulse Excitation

To achieve true broadband phase matching in a Cherenkov-type optical rectification process the pulse front can be manipulated (Auston et al., 1984). The group front of an ultrashort pulse emitted from a regenerative amplifier is flat (Maine et al., 1988), meaning that the entire lateral Gaussian spatial distribution arrives concurrently. This influences the front of the transient, though the arrival time can be distributed throughout the lateral pulse front by use of a diffractive optical element or optical chirping (Jiang and Zhang, 1998).

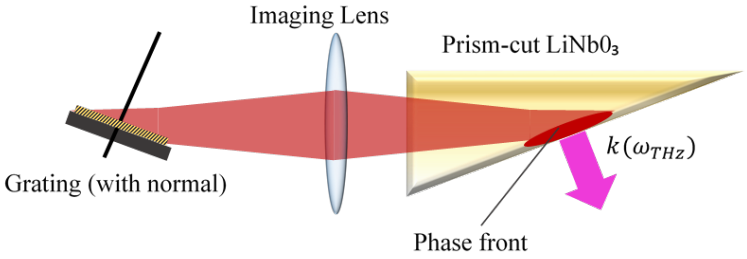

Figure 2.6: Tilted pulse excitation of $LiNb0_3$.

The tilted front can be created from the image of a beam that is incident on a diffractive optical element. The tilt angle is selected to match the Cherenkov angle of the nonlinear medium (Ravi et al., 2015), accounting for refraction if the medium is prism coupled. This tilted pulse-excitation greatly improves the efficiency of OR in many non-isotropic materials. Careful imaging of the tilted front (Hirori et al., 2011) can help to tune the size of the group front to further maximise the optical field in the crystal. The general schematic of this process is illustrated in Fig. 2.6.

The angle of the tilted front γ is matched to the image of the grating with angular parameters of incidence and diffraction θ Hirori et al. (2011). The degrees of freedom in this optimisation problem are the grating magnification factors, where the factor β_1 is a horizontal magnification factor for the pump pulse front and β_2 is the horizontal magnification factor for the grating. The first matching expression is

$$\tan\gamma = \frac{m\lambda_0 p}{n_g \beta_1 \cos\theta_d}, \tag{2.13}$$

where m is the diffraction order, θ_d is the diffracted angle, p is the grating groove density, λ_0 is the central pump pulse wavelength and n_p^{gr} is the group refractive index at the pump wavelength. The second expression is

$$\tan\theta = n\beta_2 \tan\theta_d, \tag{2.14}$$

where n is the pump pulse refractive index for the $\chi^{(2)}$ material. Horizontal magnification is used in $LiNb0_3$ tilted pulse excitation to avoid reaching the damaging threshold of the material (Hirori et al., 2011) by over-focusing in the 'un-tilted' directions that do not correspond to the desired phase matching arrangements. Tilted pulse excitation increases the width of the phase matching band for wavevectors that are firmly in the x-y plane, because of the chosen tilt orientation (Ravi et al., 2015). This helps to enhance THz emission in the desired flat, planar wavefront.

2.2 Electro-Optic Detection of Terahertz Radiation

This work exclusively utilises the Electro-optic detection method and other variations due to its many advantages. The method is phase coherent (Wu and Zhang, 1995) and used to detect long-wavelength radiation such as radiation in the Mid-Infrared (Keiber et al., 2016) to THz range; it requires limited special equipment and produces a large electronic signal with many modes of noise reduction available.

2.2.1 Electro-Optic Sampling

This method analyses the polarisation of a probe pulse that passes through a $\chi^{(2)}$ material that exhibits the linear electro-optic effect ie. Pockels' Effect (Gallot and Grischkowsky, 1999). A birefringence is generated in the medium upon incidence of a THz pulse (Jepsen et al., 2011) which alters the polarisation state of the optical pulse, which can then be read with polarisation analysis. In the case of Fig. 2.7 this analyser is a polariser, which rejects one component of the polarisation at a separate angle, after a quarter wave plate, which retards one polarisation component with respect to another. The wave plate transforms the linear polarisation to circular and the polariser spatially separates the components which then have their relative intensity read by balanced detection. The differential phase retardation shows the phase effect of the electro-optic modulation, indicating the effect of the THz field on a probe beam in a given medium. This time-dependent quantity is $\delta\phi$ (Wu and Zhang, 1995) and is found from a standard electro-optic detection. Birefringent and non-birefringent crystals had their theoretical responses compared by Leitenstorfer et al. (1999), who expressed the phase retardation imposed by a $< 110 >$ Zinc Telluride crystal as

$$\delta\phi_{THz}(t) = \frac{\omega}{c} n_o^3 r_{41} E_{THz}(t) \cdot dz \tag{2.15}$$

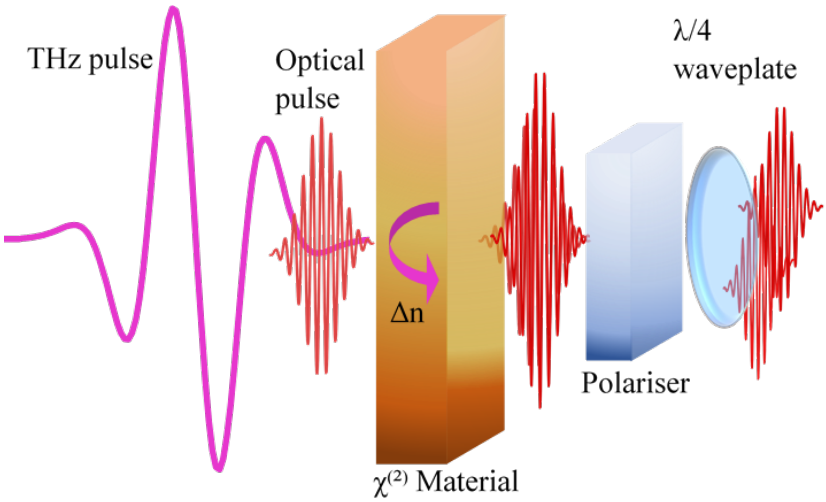

Figure 2.7: A THz pulse and an optical pulse interact in an nonlinear quadratic medium. THz birefringence alters the refractive index of the medium which alters the polarisation of the optical pulse.

for an infinitesimal propagation in z, where t is the differential time delay between the THz and probe, r_{41} is the relevant scaled constant from $\chi^{(2)}$, and n_o is the refractive index along the ordinary axis. For a crystal like b-cut Lithium Niobate the differential phase retardation can be expressed as

$$\delta\phi_{THz} = \frac{1}{2}\frac{\omega}{c}(n_o^3 r_{13} - n_e^3 r_{33})E_{THz}(t)\cdot dz \tag{2.16}$$

where the relevant elements of $\chi^{(2)}$ are different for the ordinary and extraordinary axes.

Lithium Niobate has an additional phase retardation contribution that originates from its' innate birefringence

$$\delta\phi_{nat} = \frac{\omega}{c}(n_e - n_o)dz \tag{2.17}$$

which is only dependent on the intrinsic properties of the crystal and its length. These expressions can be integrated over the crystal length, though Jones' Calculus is required to consider their effects on the polarisation components of an axial beam (Jones, 1941).

2.3 Optical Pump-Terahertz Probe Approaches

This section offers further technical detail into the processes covered in the background. Because our later methodology depends on the measurement of carrier processes, the effect of the light-matter interactions on material parameters such as the dielectric function is

explored also.

2.3.1 Optical Absorption and Carrier Excitation in Condensed Matter

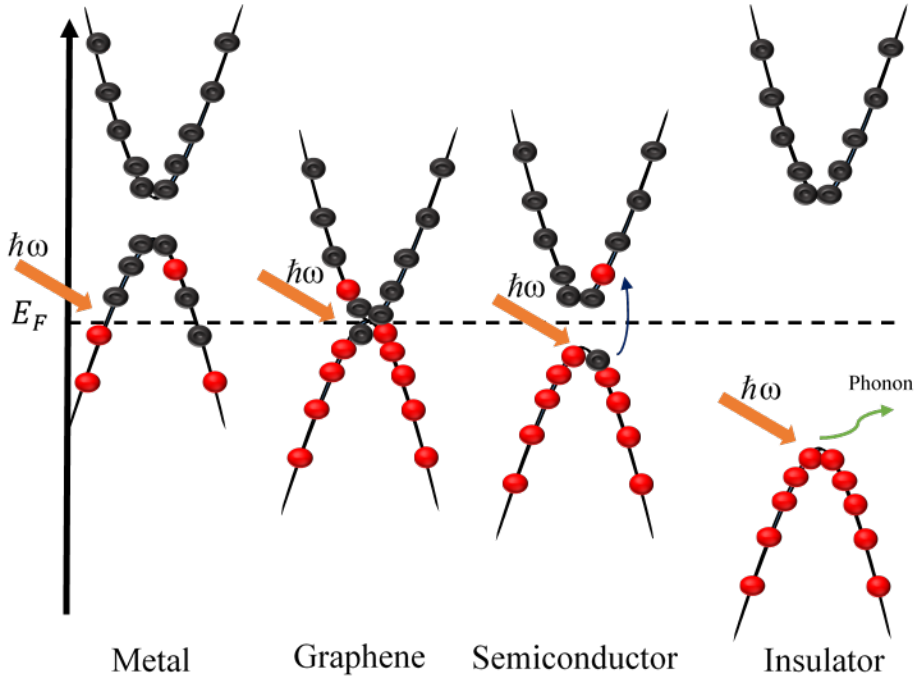

Figure 2.8: Materials absorbing a photon of energy. The available states are filled by electrons (red) and holes (black) $\hbar\omega$.

An illustration of carrier absorption can be seen in Fig.2.10. When a metal or metal-like material absorbs a photon an electron is excited to the conduction region causing the displacement of a hole. The energy of the photon doesn't inhibit the absorption process. For the semiconductor the photon again displaces the hole, but only if the energy is sufficient. In an insulator the photon energy is redistributed to the lattice because of the large bandgap energy.

This problem can be quantified by treating the perturbed hamiltonian of the system with Fermi's Golden Rule (Rossler, 2009). The probability of electron absorption in condensed matter resulting in a band transition between states is described in many texts; Bassani and Parravicini (1993) states it to be, per unit time

$$P_{\nu k_i s_f} = \frac{2\pi}{\hbar}\left(\frac{eA_0}{mc}\right)^2 \delta_{s_i,s_f}\left|\langle\psi_{c,k_f}|\hat{\epsilon}\cdot\mathbf{p}|\psi_{v,k_i}\rangle\right|^2 \delta(E_f(\mathbf{k}) - E_i(\mathbf{k}) - \hbar\omega) \tag{2.18}$$

where A_0 is the magnitude of the vector potential of the incoming light with polarisation $\hat{\epsilon}$, e is the magnitude of the electron charge, $\hbar$ is the reduced Planck's constant, c is the

speed of light, m is the free electron mass, $\mathbf{p}$ is the momentum operator and ψ_{v,k_i},ψ_{c,k_f} are the valence and conduction band wavefunctions that have energy $E_f(\mathbf{k})$, $E_i(\mathbf{k})$. The initial and final states are labelled i, f and the process conserves the spin s. This single-electron interaction is simplified when compared to a real case as it ignores the influence of the hole, which drops to the lower band in the case of absorption. The probability also gains an optical intensity dependence when the bands are considered to not be entirely full or empty (Lyon, 1986); band filling effects decrease the absorption in a given area of the material. The probability for a transition can be expressed in a simpler form by Bassani and Parravicini (1993) as

$$P_{\nu k_i s_f} = \frac{2\pi}{\hbar}\left(\frac{eA_0}{mc}\right)^2 \delta_{s_i,s_f} \left|\mathbf{e}\cdot\mathbf{M_{ev}}(\mathbf{k})\right|^2 \delta(E_f(\mathbf{k}) - E_i(\mathbf{k}) - \hbar\omega) \tag{2.19}$$

where $\mathbf{M_{ev}}(\mathbf{k})$ is the matrix element

$$\begin{aligned} \mathbf{e}\cdot\mathbf{M_{ev}}(\mathbf{k}) &= \left\langle \psi_{c,k_f} \middle| \hat{\epsilon}\cdot\mathbf{p} \middle| \psi_{v,k_i} \right\rangle \\ ... &= \hat{\epsilon}\cdot\int \psi_f^*(\mathbf{k},\mathbf{r})(-i\hbar\nabla)\psi_i(\mathbf{k},\mathbf{r})d\mathbf{r} \end{aligned} \tag{2.20}$$

where the integral is evaluated over the crystal volume. The wavevectors that are applicable for the transition are distributed with a density $V/(2\pi)^3$ in k-space where V is the crystal volume. Because of the approximations made these equations are valid for 'vertical' transitions only where $\mathbf{k_f} \approx \mathbf{k_i}$ (Bassani and Parravicini, 1993). The number of transitions induced by photons of $\hbar\omega$ per unit volume between all valence and conduction bands is

$$W(\omega) = \frac{2\pi}{\hbar}\left(\frac{eA_0}{mc}\right)^2 \sum_{i,f}\int \frac{2d\mathbf{k}}{2\pi^3} \left|\mathbf{e}\cdot\mathbf{M_{ev}}(\mathbf{k})\right|^2 \delta(E_f(\mathbf{k}) - E_i(\mathbf{k}) - \hbar\omega) \tag{2.21}$$

where the integral extends over the allowed wavevectors $\mathbf{k}$. The process of absorption alters the complex dielectric constant of the material,$\epsilon = \epsilon_1 + i\epsilon_2$, and as expressed by Bassani and Parravicini (1993) this constant is related to $W(\omega)$ by

$$\epsilon_2 = \frac{2\pi c^2\hbar}{A_0^2\omega^2} W(\omega) \tag{2.22}$$

where the real component of the dielectric function can be found by utilising the Kramers-Kronig relation, resulting in (Bassani and Parravicini, 1993)

$$\epsilon_1(\omega) = 1 + \frac{8\pi e^2}{m^2}\frac{2\pi}{\hbar}\left(\frac{eA_0}{mc}\right)^2 \sum_{i,f}\int \frac{2d\mathbf{k}}{2\pi^3} \frac{\left|\mathbf{e}\cdot\mathbf{M_{ev}}(\mathbf{k})\right|^2}{[E_c(\mathbf{k}) - E_v(\mathbf{k})]/\hbar} \frac{1}{[E_c(\mathbf{k}) - E_v(\mathbf{k})]^2/\hbar^2 - \omega^2} \tag{2.23}$$

To conclude, a photon absorption can induce changes in the real and imaginary parts of the dielectric function, thus changing the absorption and delay of the system.

2.3.2 Thermalisation and Recombination

The absorption process changes the dielectric function because of the formation of quasi-free hot carriers. Carriers thermalise towards the ground state, via different scattering processes. However, when the excitation is provided by ultrashort pulses, thermalisation processes can be even several order of magnitude slower (Agarwal, 1975). This means that it is possible to follow the track recombination response, revealing properties that mediate the carrier-recombination, and this can be done using a short pulse as excitation and a short pulse as a probe of the dielectric function.

Thermalisation of carriers is part of the bulk relaxation and recombination processes in excited semiconductors whereby the carrier dynamics are similar to that of conductors. Therefore this time is intrinsically related to the time constants of the recombination processes that were previously mentioned in Fig. 1.6. The major contributing transition is the band-to-band radiative transition which emits a photon of energy $\hbar\omega$, the trap-assisted recombination process which normally dissipates energy in phonons, and the Auger process which is an uncommon three-particle interaction between the electron, hole and a second electron which is excited within the conduction band (Bullis and Huff, 1996). However, the type of process that occurs is also dependent on the time that has elapsed since the initial absorption; directly after the absorption the electrons in the conduction band relax, releasing energy or phonons through electron-electron and electron-phonon processes (Lyon, 1986). These processes largely involve scattering (Rossi and Kuhn, 2002), allowing the electron distribution to reach the lowest available energy state in the band.

To consider the how the probability of any of the recombination processes occurring affects the dielectric properties of the material the constant can be expressed in its oscillator-mode based basic form (Hopfield, 1958) which excludes dissapitive interactions

$$\epsilon(\omega) = \sum_j \frac{4\pi\beta_i}{1 - (\omega^2/\omega_j^2) + i\gamma_j\omega} \tag{2.24}$$

where ω_j is the resonant frequency of a particular mode. γ_j is the transition probability for the jth decay mode, and β_j is the polarisability of the jth decay mode. These decay modes are carrier-photon or carrier-phonon interactions that lead to the loss of energy of a particular exciton - in the simplest case when a single type of decay occurs $\gamma^{-1} = \tau$, the lifetime of the exciton. These lifetimes are characteristic of the transition.

The immediate non-thermal (hot) carrier relaxation and activity in the conduction band can be characterised by a lifetime τ_0 that is dependent on the plasma oscillation frequency ω_p as Fann et al. (1992)

$$\tau_0 = \frac{128}{\pi\sqrt{3}} \frac{1}{\omega_p} \tag{2.25}$$

which is an ultrafast process of the order of fs (Fann et al., 1992). The subsequent thermalisation is the process alters the complex dielectric function of the material in the excited region also. There are some associated lifetimes, for example the time constant for radiative recombination is roughly inversely proportional to the carrier concentration of the material (Hall, 1959).

Hence, by mapping the dielectric constant and discerning the different decay dynamics occurring as the carrier relaxes, we can extrapolate the time-constants and associate them to the magnitude of the ongoing recombination processes, highlighting material properties.

2.3.3 Probing with Terahertz Fields

Once carriers are excited in a material there are multiple methods of profiling the subsequent dynamics, and even some of probing minute details in the thermalisation if everything is kept at 'ultrafast' limits (Joyce et al., 2018). It is possible to detect these transients using optical probe reflectance measurements or ellipsometry (Yoneda et al., 2003) wherein a weak, polarised optical pulse is directed onto the thermalised region and either transmitted through or reflected from the sample then analysed for polarisation change. By varying the arrival time of the pulse the full transient can be reconstructed, including the thermalisation and relaxation, and if given sufficient temporal resolution so can the carrier processes. These processes, as mentioned to be scattering, diffusion, surface recombination (Heinz et al., 2017), etc produce small changes in the transient that last between a couple of picoseconds and tens of picoseconds; the overall recovery can even last nanoseconds in bulk semiconductors like Silicon (Fossom et al., 1983). It can be deceptive to consider the polarisation analysis of this weak probe as indicative of polarisation sensitivity of the ellipsometry measurement. In fact, the measurement lacks phase coherence because the measured polarisation signal is an intensity, and only proportional to the intensity of the field attenuation caused by thermalised carriers. Because of this any complex parameters involved in the thermalisation process are effectively non-existent to the optical probe; this includes anything to do with an induced phase change such as the complex refractive index and complex dielectric function. In order to measure these

parameters a different approach is required therefore this is where THz probing comes in as a coherent approach to carrier dynamic measurement. To a THz wave the lattice is deeply subwavelength. THz probe is physically a 'THz Time Domain Spectroscopy' setup - it consists of a THz generation arm and a detection arm with space for a sample placed in a chosen region. In this arrangement it is the sample that is excited by the optical probe and is either placed confocally in the far-field or within the near or pseudo-near-field region. As with an ordinary THz spectroscopy setup a TDS is obtained of the sample space containing spectral details from the sample, and in the case of a thermalised sample excited by an optical pump these spectral details will include phase changes from which the previously mentioned complex parameters can be extracted.

Chapter 3

Terahertz Hot-Carrier Microscopy

As introduced in the previous chapter, the idea of mapping the recombination dynamics of hot carriers in order to infer physical/chemical properties of targets has been pursued within the framework of point-like probing. This means that, in the art, spatially resolved *videos* of the recombination dynamics mapped via terahertz scattering can be obtained by repeating the acquisition on different part of an object. By changing the delay between an optical pump pulse and a terahertz probe, the scattered terahertz field reveals the dynamics in each point of the object surface. However, although the literature is not always straightforward on this specific point, there are some underlining hypotheses on this process. (i) The carrier dynamics in a point of the object are completely uncoupled with the dynamics in a adjacent point. (ii) The effect of the pumping mechanism is fundamentally local, meaning that the excitation of a specific point relates only to the illumination impinging that specific point. (iii) The variation of the detected terahertz field directly relates only to the illuminated point.

While all conditions are easily fulfilled in homogeneous bulk under homogeneous pumping, we could argue that this is not necessarily true in presence of structured devices. Besides, we can also argue that this is exactly the case in which imaging becomes a necessary diagnostics. Last, it is indeed trivial that in imaging complex structures the coarse terahertz wavelength is not a desirable resolution limit, and that optical pumping allows for a significant more spatially resolved excitation morphology. Those elements are the main rationale behind my work on Optical Pump Near-Field Microscopy, which answers to the challenge of terahertz-imaging simultaneously the carrier recombination dynamics on large surfaces with arbitrary excitation dynamics and resolution approaching the optical diffraction limit.

3.1 Optical-Pump Near Field Terahertz Microscopy

Optical Pump-Near Field THz Microscopy (OP-TNFM) is our novel technique towards terahertz hot-carriers Microscopy, that allows for complex analysis of semiconducting materials. The basic idea of this approach is to fuse a large parallel terahertz imaging technique with sub-wavelength resolutions of large area excitation. The basic steps that are used to implement this methodology occur concurrently within the setup. A target is simultaneously illuminated by an ultrashort THz pulse and an intense ultrashort optical pulse. The latter causes photo-promotion of carriers in a semiconductor that has a bandgap smaller than the pulse energy. The relative time delay between the optical and THz pulse is then changed, allowing the mapping of the spatially-distributed optical carrier interaction in a set of images at specific delays. The image set shows the carrier distribution evolving with respect to the initial excitation. This target is an object placed in the near-field region of a large electro-optic sensor which results in the temporal dynamics of the terahertz field amplitude in different points being resolved in parallel over a large area. Due to the near-field detection, the field distribution can be resolved with sub-wavelength spatial resolution.

For the embodiment of the methodology that was realised in this thesis, high energy ultrafast laser pulses, centred at 800 nm, from a Coherent Libra He+ regenerative amplifier were used. This wavelength was chosen because it is suitable for THz generation via tilted pulse excitation in Lithium Niobate and is also an appropriate energy to excite carriers in semiconductors like Silicon. The THz radiation was generated by P_1 (see fig. 3.1) used for non-collinear tilted pulse excitation of prism-cut $LiNb0_3$, producing high energy pulses centred at 0.7 THz via the nonlinear quadratic process of optical rectification. These pulses were focused onto the detection crystal, a 20 μm thick x-cut $LiNb0_3$ mounted on a glass substrate. A low energy probe pulse, P_2, centred at 800 nm was imaged onto the lower surface of the detection crystal, with its corresponding imaging plane positioned at a $CMOS$ array. This allows a high-resolution image to be taken of the polarisation distribution region near the upper facet of the detection crystal, and therefore the sample is placed within this region. Concurrently, P_3 is magnified and imaged onto the plane of the detection crystal, freeing carriers in the sample and thus changing its conductivity, affecting the polarisation distribution that is recreated in the $CMOS$ plane. When a THz image is taken of a semiconductor or insulator, the THz pulse is imprinted with the spectral fingerprint of the material. When a series of THz images is taken the full THz waveform can be reconstructed in time by varying the delay of P_1 throughout the set, or

the recombination dynamics of the hot carriers on the sample surface can be reconstructed by varying the delay of P_3. The target on the detection crystal will have its field interaction spatially reproduced at the imaging plane reproduced at the camera plane by splitting the beam into polarisation components to detect the small birefringence change caused by electro-optic effect in the detection crystal under influence of the THz field. The process of electro optic detection is coherent, whether photodiode or $CMOS$ detection is used, as phase information of the field is preserved either way. Therefore a single $CMOS$ detector is used to take a differential measurement between the polarisation components of the beam, allowing the components to remain synchronised, and a dynamic subtraction technique is utilised to increase the signal-to-noise ratio. This dynamic subtraction was implemented by synchronising a chopper to block the THz pulses in every other frame, thus providing a set of background 'dark' frames to subtract noise from the 'light' frames.

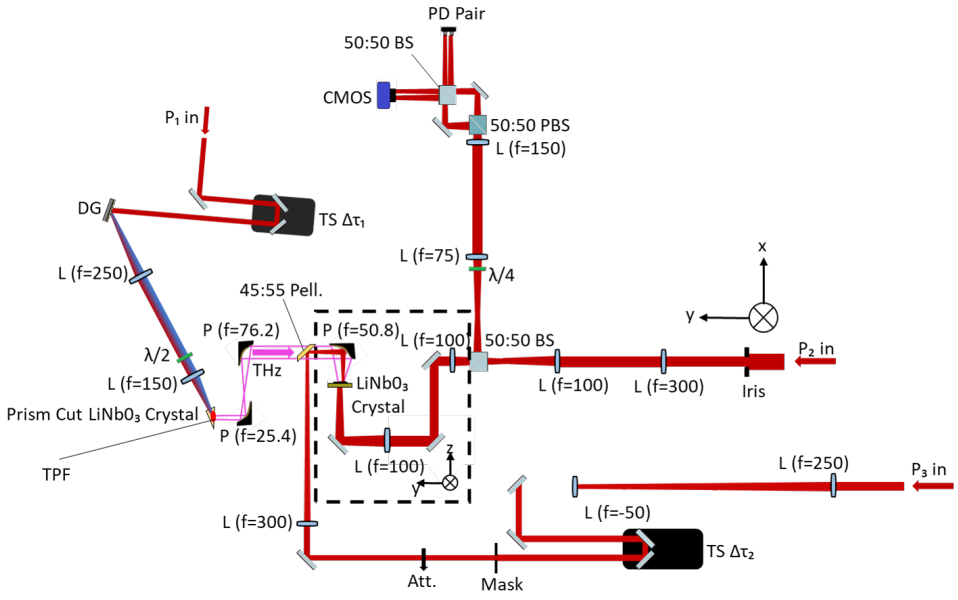

Figure 3.1: Full experimental diagram of the free space setup. All focal lengths stated are in mm.(DG – Diffraction Grating, BS – Beam Splitter, L – Lens, PBS – Polarising Beam Splitter, TS – Translation Stage, TPF – tilted Pulse Front, λ – waveplate, P – Gold Parabolic of 1 inch diameter, P_i are pulses described in the next paragraph.

The Terahertz Source

Tilted pulse excitation of prism-cut $LiNb0_3$ crystal in the Cherenkov geometry was utilised for THz generation. The pump that excites this process is Gaussian in shape and collimated and can be described as horizontally polarised. As seen in Fig 3.1 the sub-mJ

energy optical pulse, with a length of 105 fs, enters the setup where energy is deflected twice to create the screening pump arm and then the probe arm using a 0.1 neutral density filter and a 92 : 8 beam sampler respectively. The pump is then directed to a delay stage that offers 630 ps of variable delay. The next part of the arm creates a tilt in the phase front of the pulse the design of which is Hirori et al. (2011), and this tilt is created by first entering a holographic reflective grating of groove density 1800 cm^{-1} at incident angle of $\Theta_i = 35.3°$ creating a zeroth order diffraction at an angle $\Theta_d = 55.7°$ from the grating normal. The first order from the grating is discarded (which limits the efficiency of the process). The zeroth order pulse is allowed to propagate through a half wave plate set to rotate the polarization to a vertical orientation and a Keplerian telescope consisting of cylindrical lenses of focal length $f_1 = 250$ mm and $f_2 = 150$ mm arranged confocally to create a grating image at a distance f_2 from the second lens. This image coincides with a face of the prism cut $LiNb0_3$ which has prism angle 62 °; this angle coincides with the grating image angle because of the resizing from the lenses. To focus the THz plane wave that is emitted from the crystal face a system of 3, 1 inch gold coated parabolic mirrors are used with focal lengths $f_1 = 25.4$ mm, $f_2 = 76.2$ mm and $f_3 = 50.8$ mm that are arranged confocally with distances of separation f_1, $f_1 + f_2$, $f_2 + f_3$, f_3. The THz is chopped with a mechanical chopper placed between the final two parabolics so that both lock-in detection and dynamic subtraction imaging can be performed. This final section of the arm expands the THz beam and then focuses it down to a waist size of 1 mm on the horizontally-oriented crystal plane.

Electro-Optic Detection

The probe beam is reduced to 4 mm in size using an iris and then enters an $f = 300$ mm lens after 300 mm of propagation. After 400 mm of propagation the beam enters the first 100 mm lens of the periscope system which consists of 3, 100 mm lens confocally arranged (200 mm apart) with a final 100 mm of propagation between the final lens, called the imaging lens, and the detection crystal face. The system is designed to direct the beam to enter the crystal from below such that the crystal can be simultaneously exposed to optical and THz radiation from below and above respectively. Because of the 3× magnification applied at the entry to the system the size of the probe image on the crystal is 1.3 mm; the corresponding imaging plane is at the initial iris. A very thin detection crystal is placed at this plane to maximise the image resolution by limiting the size of the detector region. The detection crystal is a 20 μm thick b-cut $LiNb0_3$ crystal mounted on a 1 mm− thick

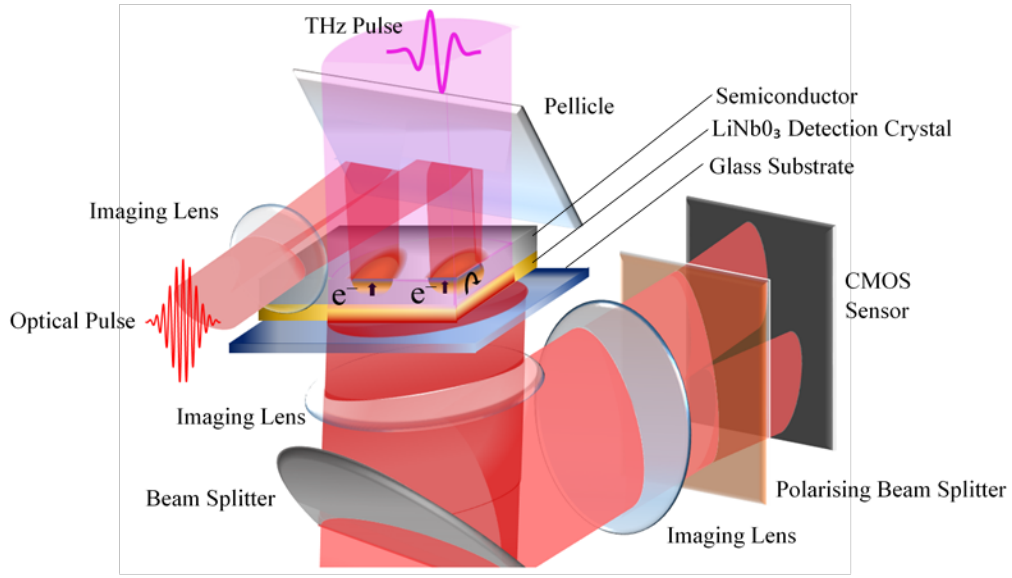

Figure 3.2: Stylised and labelled setup diagram.

glass substrate for mechanical stability, polished and coated on the top and bottom sides with HR-coating and AR-coating respectively. The coatings on the detection crystal are designed for minimum reflection of the probe pulse from the lower crystal facet upon entry and maximum reflection from the upper facet to prevent probe losses. The reflected pulse then re-enters two of the arranged 100 mm lenses but is deflected by a 50 : 50 beam splitter cube before reaching the initial periscope entry. The beam confocally enters a Keplerian telescope with two lenses of focal length $f_1 = 75\,\text{mm}$ and $f_2 = 150\,\text{mm}$ to expand its size, and a quarter wave plate to introduce phase retardation between the polarisation components of the probe. The orientation of the wave plate is set to balance the intensity of the polarisation components as detected by a balanced pair of photodiodes later in the setup but first the components are spatially separated by a 50 : 50 polarising beam splitter. Each polarisation is split again by 50 : 50 non polarising beam splitter which creates two pairs of polarisation components with each pair propagating at right angles with respect to each other. One pair is incident upon a $CMOS$ detector array (The Imaging Source DMK23UP1300) placed 150 mm optical distance from the final lens of the periscope, the lens described as $f_2 = 150\,\text{mm}$ from the final Keplerian telescope. This places the $CMOS$ sensor array at a corresponding imaging plane to the detection crystal and the initial iris. At the $CMOS$ plane, an image of the background-subtracted polarisation map of the THz induced birefringence is visible for each polarisation component of the probe pulse. The remaining pair of probe polarisation components are directed to the previously mentioned custom balanced photodiode pair.

Ultrafast Carrier Excitation

The energy deflected from the main pulse by the 0.1 neutral density filter is used to excite carriers in a sample placed near the crystal plane. This arm contains around 40 μJ of energy and is directed over the periscope setup into a Galilean telescope of $f_1 = 300$ mm and $f_2 = -75$ mm placed 225 mm apart. The beam is now tightly confined, allowing for more energy to pass through the later iris and be available for carrier excitation. The beam is then directed into a delay stage with approximately 200 ps of variable delay. It is then clipped by a mask and attenuated before entering a 300 mm lens placed 300 mm after the iris and directed into a 45 : 55 pellicle placed in the THz beam path 60 mm before the final $f = 50.8$ mm parabolic, causing 19 μJ of energy to be imaged onto the crystal plane. In order for the image to be formed the 300 mm lens and iris are carefully placed to ensure that the system is in focus, leaving around 350 mm of propagation distance between the lens and parabolic. The mask is recreated in the imaging plane as an optical intensity distribution, and an opaque sample that is also placed in this plane will undergo absorption of the optical field.

3.1.1 Spectroscopic Benchmark of the Microscope

For the purpose of the Optical Pump - Terahertz Near Field Imaging method three possible detection crystals were compared. The spectra seen in Fig. 3.3 were taken with the same THz pulse and only differ in their detection properties. It's clear from the Figure that an HR- coated crystal produces a spectrum with a higher SNR - this crystal was selected for experiment. The GaP could perhaps be a great choice for a Near-Field THz imaging application because it has fewer defects than the ZnTe but a larger bandwidth than the $LiNb0_3$.

3.2 Benchmark Examples of Terahertz Near-Field Microscopy

This section contains Terahertz time-domain near-field images taken with an electro-optic 2D detection utilising coated $LiNb0_3$ as the detection crystal.

The first sample is an unbiased spiral photoconductive micro-antenna; as seen in Fig.3.4 it is around 1 mm across and thus should be expected to scatter THz fields on the micron scale. The sample itself is thin: 300 nm of Au printed on a plastic substrate of around 300 μm. Ideally this sample can act as a photconductive emitter but it requires pumping

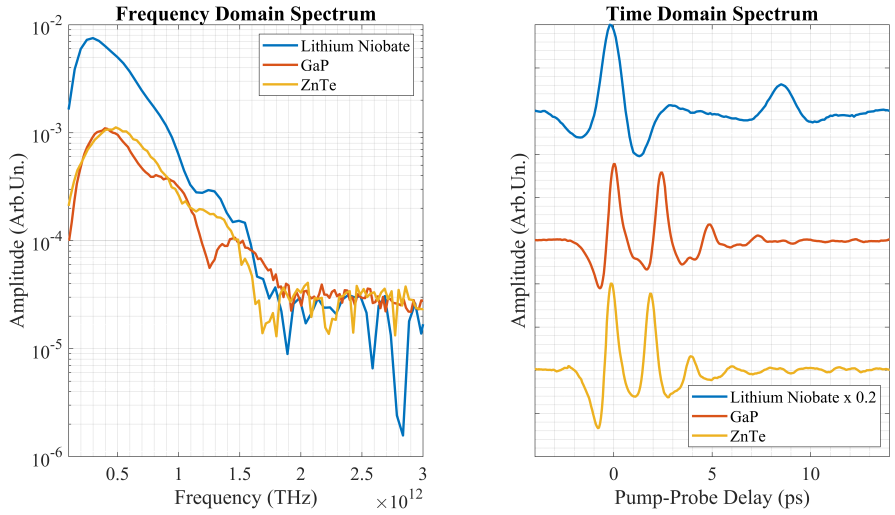

Figure 3.3: A THz trace taken with an uncoated 100 μm thick ZnTe $\langle 110 \rangle$ crystal, a single side AR- coated 100 μm thick GaP crystal $\langle 110 \rangle$, and a AR- coated and HR - coated 20 μm thick $LiNb0_3$ b-cut $\langle 100 \rangle$ crystal mounted on a 1 mm thick glass substrate.

that matches the absorption profile of the Germanium centre in the UV- range. The

Figure 3.4: Optical image of the spiral antenna with 300 nm thick gold printed on a plastic substrate. The ticks on the scale are 100 μm

Fig.3.4 shown is an optical image of the sample in Fig.3.5 which is an example of a partially opaque object to THz. It is sufficiently thin to lie in the near field region of the THz field detection region so its morphology can be revealed with THz imaging analysis. Although the gold is not transmissive to THz the sample scatters fields and thus after a certain time after the arrival of the THz the morphology of the sample is obscured by scattering. At times before the field peak at $t = 0$ ps, The THz field is absent in areas corresponding to the gold film. The scattered THz interferes throughout the image and

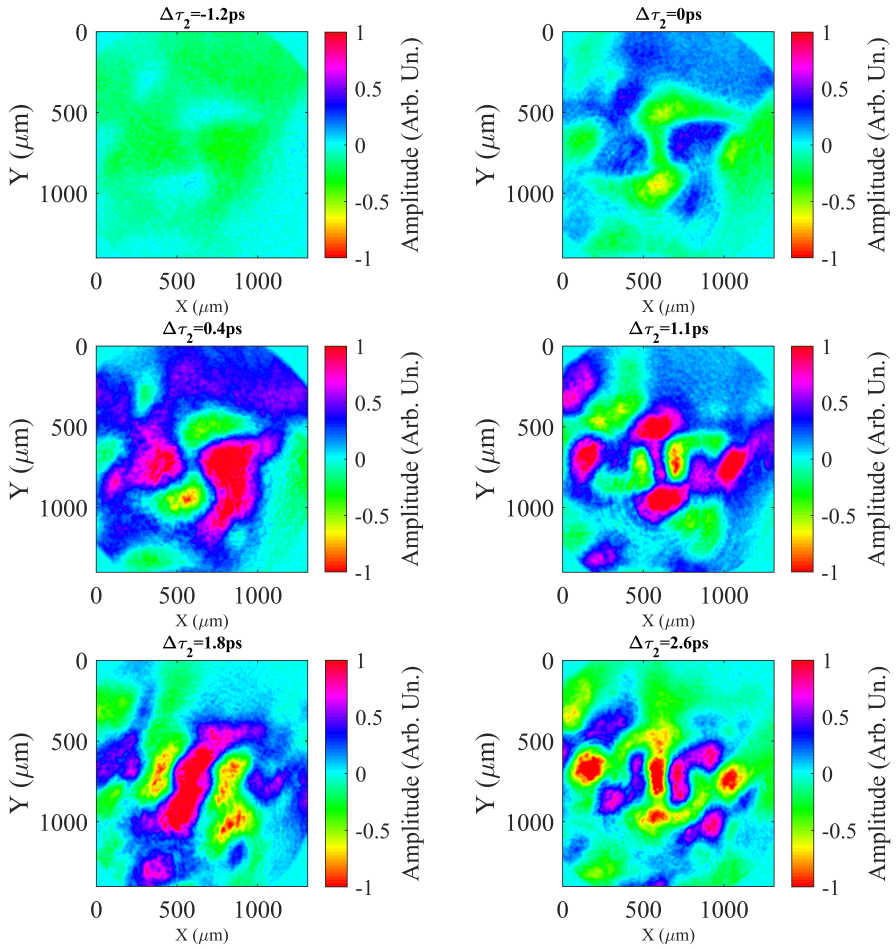

Figure 3.5: Background subtracted polarisation THz Time Domain images of gold 'Spiral' sample. The detection crystal used was HR@800 nm- and AR@800 nm- coated $LiNb0_3$ of 20 μm thickness.

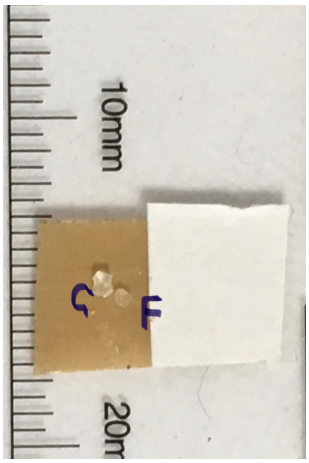

Figure 3.6: An optical image of the glucose and fructose crystals measured in experiment, on a tape substrate.

this coupled with further scattering from structures causes more complex patterns to form as time evolves. Of interest is the pattern at time around 1.1 ps where the THz scatters from the Ge in almost a 'square shape. In this way the sample morphology, like the Ge square, can be revealed at later times.

Sucrose crystals are an appropriate sample for benchmarking the spectroscopic capabilities of the THz microscope. Fructose and Glucose have distinct chemical signatures in the THz region but are indistinguishable optically. Additionally, the grain morphology can affect the reconstructed waveform via the THz scattering process. This scattering information cannot be measured with a standard spectrometer. This sample, seen in Fig. 3.6, was chosen to demonstrate that by using a wide area of parallel illumination a wide area of THz transmission spectra can be extracted even with binning. The Glucose and Fructose grains were collected from each sample and placed on a packing tape substrate that is nearly completely transparent to THz in terms of its low power absorption.

For this dataset in Fig. 3.7 the THz delay has been set to peak in the grain areas of the image; the THz that passes through the grains arrives slightly after the THz that does not. As seen in Fig. 3.7, the amplitude of the field in the grains varies between positive and negative values before scattering occurs several ps after the time of first incidence. The time between incidence and scattering is dependent on sample morphology, in this case the sample almost transmits THz uniformly and thus is cylindrical in shape, to the THz at least.

The Fig. 3.8 shows the extracted spectra, phase and transmission from the images. In referenced spectroscopy a reference is selected from the same spatial region of the THz but

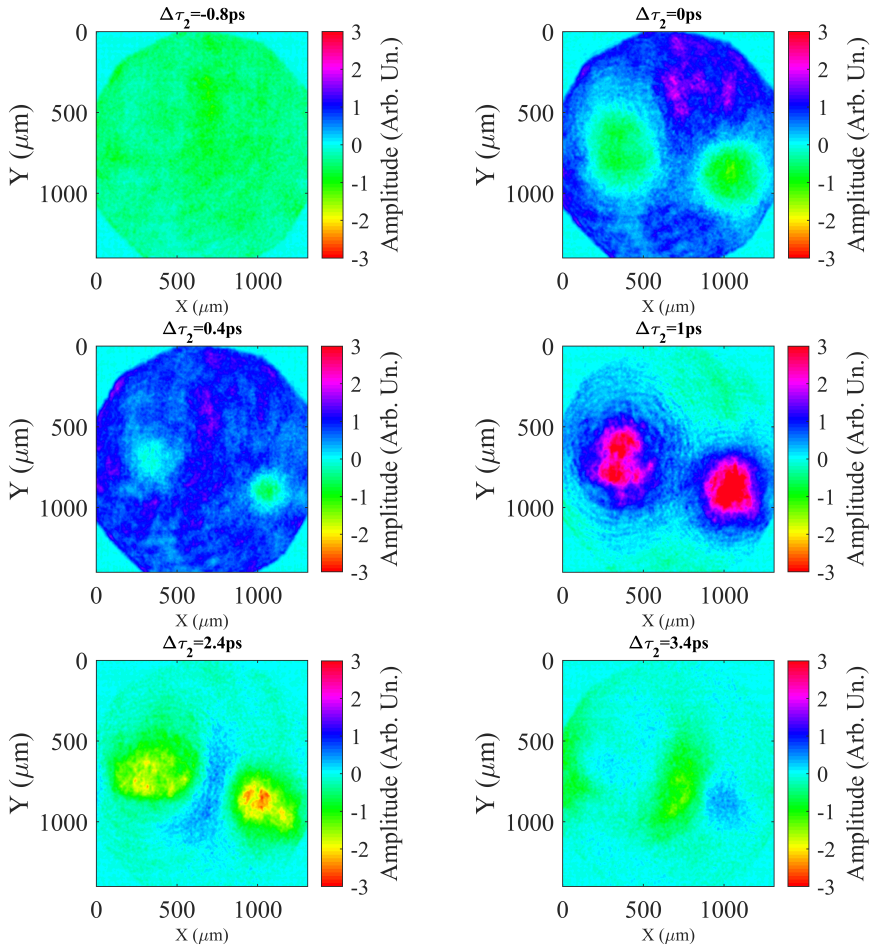

Figure 3.7: Background subtracted polarisation THz Time Domain images of sugar and fructose grain samples. The detection crystal used was HR@800 nm- and AR@800 nm-coated $LiNb0_3$ of 20 μm.

with a sample placed or removed. However, in this experiment the reference is taken from a separate region which was far from the Gaussian centre of the THz; this is an unfortunate reality of concurrent reference extraction. Imaging artefacts that are present in the probe beam also cause regional variations, and possible over- or under- probing if the beam is saturated or contains hot spots. Here these regional variations in the probe and the THz have contributed to an under-powered reference that is lower in amplitude than the probe. A possible solution is to create a Gaussian mask to 'multiply out' variations. The desired shape for this mask is slightly problematic because it should not conceal the time evolution of the THz, nor should it obscure its Gaussian shape and scattering profile. Back to the discussion of Fig. 3.8, the spectra should be noted not just for their amplitude but also their spectral shape. The reference contains multiple peaks due to Fabry-Perot reflections

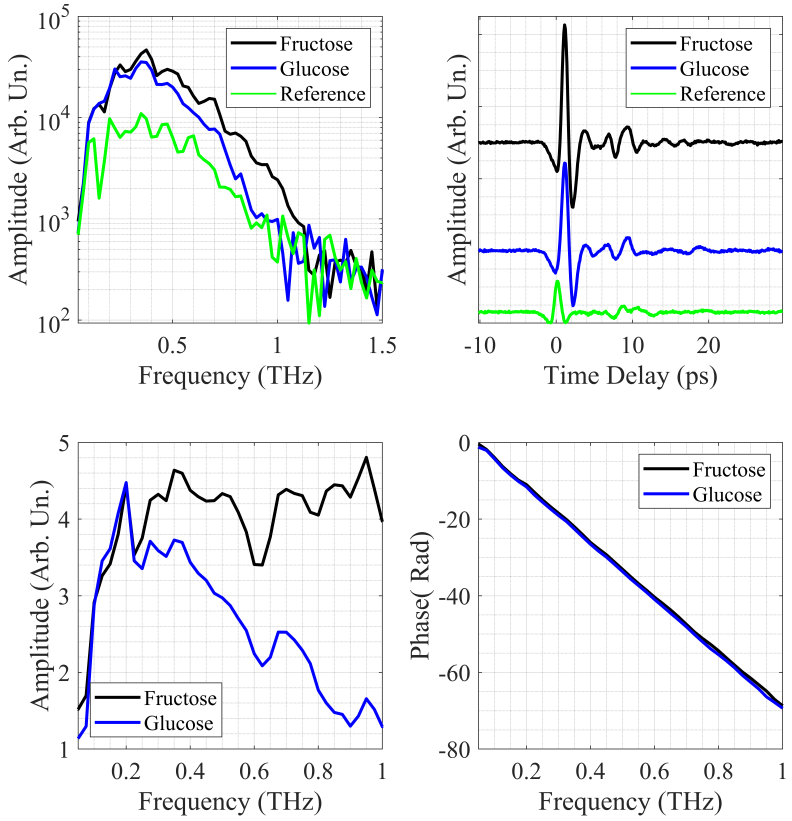

Figure 3.8: These graphs show (clockwise from top left) the frequency domain spectrum, time domain spectrum, transmission spectrum, and field phase of two regions of sample in the image set and one reference.

within the detection crystal. The low frequency peak is likely to be the result of an artefact in the probe sampling region. The THz time domain spectra show oscillations that are likely to correspond to THz scattered from the grains' outside structures arriving at the detector at slightly different times. All THz spectra taken in air have low amplitude water absorption lines (though in the case of the grain spectra the scattering is strong enough to conceal them) but when imaging with thin $LiNb0_3$ the low detection bandwidth can conceal features like this. The transmission spectra of the fructose and glucose show clear differentiation between the two grains at high THz frequencies. The shape of the crystal can have a contribution to transmission as can absorption features of the grain both chemical and morphological. In this measurement it appears that the transmission was most useful because the field phase is practically identical for the grains. This implies that the sampling region may be too large to distinguish any significant topographic differences in the grain as the phase is sensitive to the transmission path of the THz field.

3.3 Optical Pump-Terahertz Near Field Imaging: benchmarks

Creating a carrier distribution on a material wafer is the first step of Optical Pump Near Field Imaging; then obtaining an image of the THz interaction was achieved at a set time. Subsequently the thermalisation signal from carrier recombination was measured before a time-of-flight measurement of a multi-composite semiconductor sample was taken.

3.3.1 Spatially Distributing Thermal Carriers

One major goal in the project was parallel illumination of samples and the simultaneous illumination of different areas. Imaging masks onto the optical beam is the simplest method to achieve this because it eliminates issues with synchronisation.

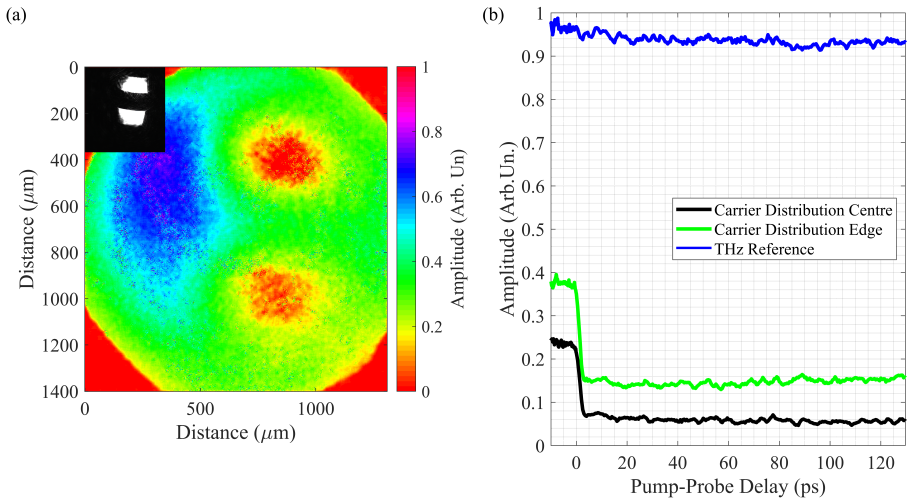

Figure 3.9: A distribution of thermal carriers was created on a 380 μm Silicon wafer. The transients were extracted from the image set.

In Fig. 3.9 part (a) the carrier distribution was created on a Float-Zone Silicon wafer that is far larger than the microscope field-of-view. The distribution closely follows the intended beam image but is affected by diffraction in the wafer. This allows for assessment of the resolution reduction that occurs due to diffraction of the THz between the wafer facet and the detector. The transients were extracted from the image set as seen in part (b) and exhibit the long transient recombination that is characteristic of low-energy pumped Silicon. The recombination times extracted from the dataset are of the order of ns. However the extraction long recombination time from the short dataset is not accurate enough to include in the results. A longer delay stage is crucial in extracting characteristic

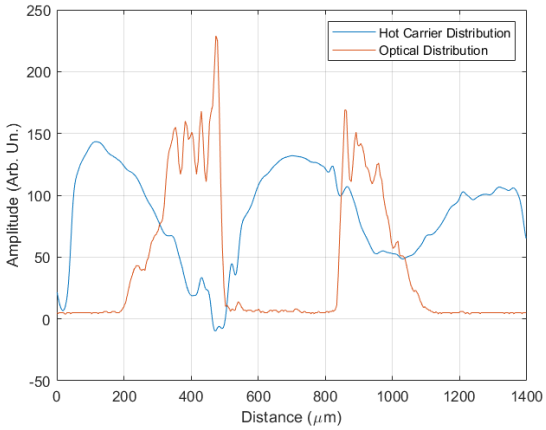

Figure 3.10: The line plot taken from the inset and THz image of the Fig. 3.9.

recombination times from the thermal carrier distribution. The two regions that have had their transients sampled show slight differences in recombination and absorption signal amplitude. The subtlety of these differences make it hard to determine whether they are due to truly unique dynamics in the region or probe sampling inaccuracies.

Assessment of the THz Diffraction

The plot in Fig 3.10 compares the line plots for an optical and THz carrier image with the sample a 380 μm Si wafer, leaving the image a full wafer thickness away from the imaging plane. The THz near-field image of this carrier distribution shouldn't necessarily be a 1:1 map because the propagation distance is of the order of the wavelength and this allows for Fraunhofer-style diffraction in the wafer.

3.3.2 Imaging of Thermal Multi-Composite Samples

Many target applications for the OP-TNFM methodology are multi-composite, such as micro-devices and solar cells. The above figure is a part of a multi-composite sample utilised for THz carrier imaging, where there is a 2D and height distribution of semiconducting materials. The target device consists of a 400 μm GaAs rod (seen in Fig. 3.11) placed on a 380 μm thick Si substrate; GaAs and Si both have distinctive carrier dynamics and show characteristic recombination dynamics with transient spectroscopy. The Fig. 3.12. shows the sample illuminated by THz radiation, with delay set to 1.6 ps post arrival of the main pulse, allowing for slight scattering of the THz as it peaks in the rod. Attenuation of the THz field in an area of the image is easier to detect when the amplitude of the THz in that area is not zero. The left image shows this THz distribution, while the right image

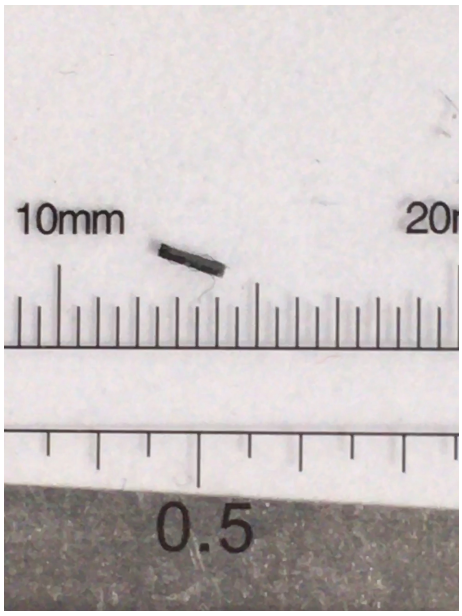

Figure 3.11: Optical image of GaAs rod used in experiment.

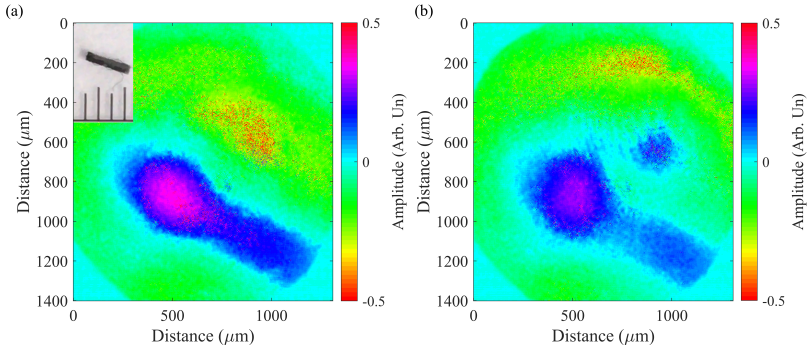

Figure 3.12: Static THz image of GaAs sample with and without contact with a thermal carrier distribution.

additionally has an area of thermal carriers liberated by the an optical pump pulse. This measurement involved the time delay of the optical pump over a large range of values, allowing for extraction of the carrier transients.

The Fig 3.13. Shows the transients extracted from different areas of the image set that each display a fairly complicated shape, however they do show the expected recombination after absorption with likely shape influence from THz scattering. It is possible to see the different absorption arrival times of the pump in each region that correspond to the vertical height of that region above the detector. This specific shape of the recovery makes it more difficult to extract a recombination time from the data because it does not neatly fit an exponential function. A significantly longer variable delay is required. The respective amplitudes of the transients are partially due to their different locations within the THz

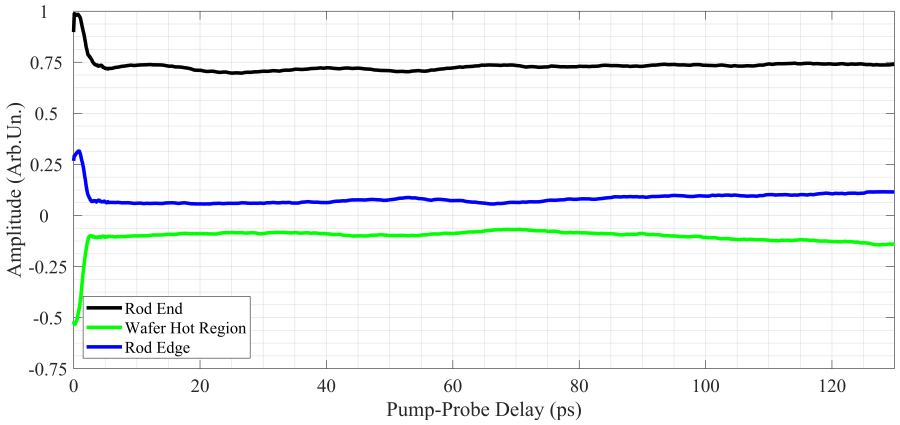

Figure 3.13: Carrier transients extracted from three 100-pixel areas of the image set: The centre of the thermalised carrier region 'Wafer Hot', the end of the rod seen at the centre of the image 'Rod Edge', and the edge of the rod that overlaps with the thermalised region. The reference 'Wafer Cold' is taken from the top of the image far from the thermal region.

Gaussian centre because there is a similar excitation energy within each sampling region. Another likely factor is the wafer and rod quality; while the wafer is high quality Float-zone manufactured and polished on both sides the GaAs rod has surface defected and is a lower quality offcut, thus detrimentally affecting the pump absorption at the surface due to optical scattering.

The time evolution of the THz is shown in Fig 3.14, by taking the static THz image with thermalised carriers and changing the THz time delay while keeping the time delay difference between the THz and the optical pump static. This allows for THz scattering from sample structures and the thermal carrier distribution which is seen as time evolves over this set of images. Terahertz scattering causes non-local interactions in images after the THz arrival time, which complicates the analysis. Terahertz spectra can be extracted from various areas of the full image set but due to sample scattering they will show a time-dependent non-local interaction which can be filtered from the spectrum restricting the Fourier transform to an early portion of the data.

The THz time domain spectra in Fig. 3.15 show distinct features between regions due to the interplay between THz scattering and thermal carriers. Similarly to the transients, the peaks show that the THz has different arrival times in each region. However, the deformed THz spectra complicate the determination of the central peak. The reference peak 'Wafer Cold' is clean and is essentially an attenuated THz field when compared to its source; there are no visible additional deformations or scattering oscillations. This

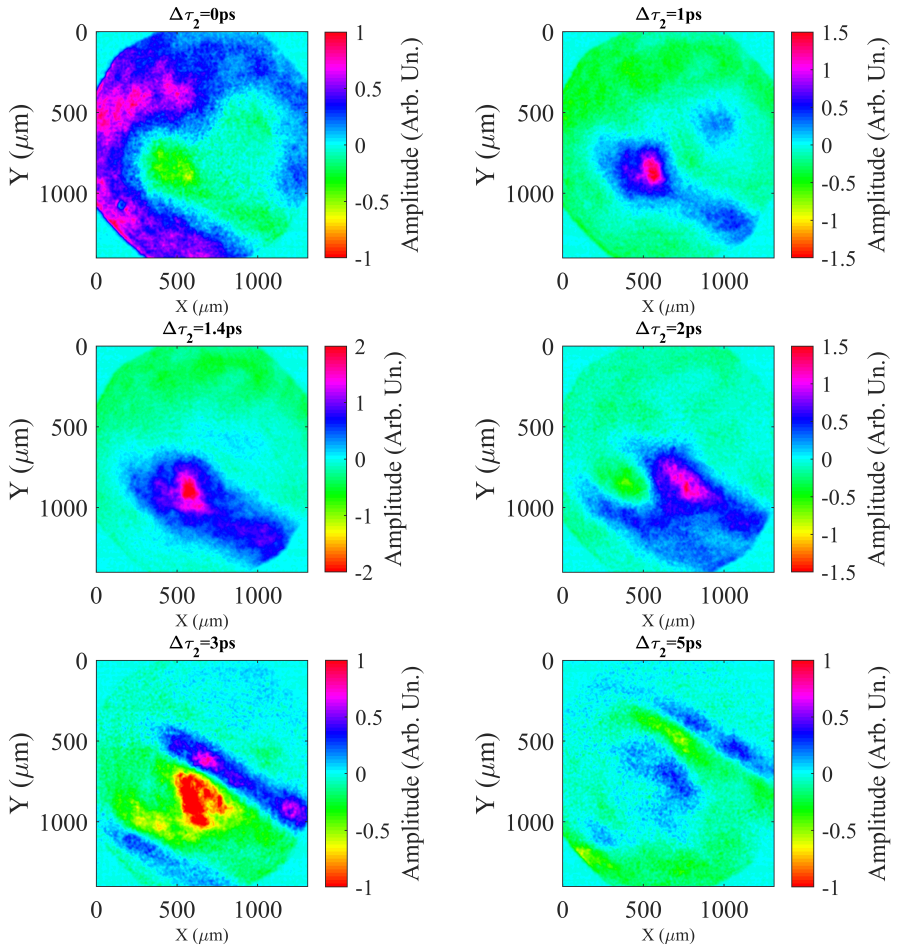

Figure 3.14: The static THz image with thermalised carriers that was previously shown.

pulse is the one with the widest bandwidth and comparatively the regions affected by the carrier distribution have fewer high frequency oscillations. Due to the high THz amplitude because of its central position the 'Rod End' region is double-peaked at the THz maximum, which in this case is caused by the edge of the rod lying in the sampling region so that two different path lengths are sampled. The 'Wafer Cold' section is hugely attenuated by the presence of hot carriers but its slight delay with respect to the peak is due to an angle in the THz wavevector rather than the carriers themselves inducing delay.

The frequency domain spectra seen in Fig. 3.16 compare the reference to other areas of the image set. It should be noted that the amplitudes of the THz in different areas are affected by their position in the THz Gaussian distribution so the THz reference peak is of the same magnitude as certain sample areas, but the transmission still shows some interesting features. The reference spectrum can be seen in part (a) of Fig. 3.16 where there are multiple peaks from Fabry Perot reflections in the detection crystal; despite this

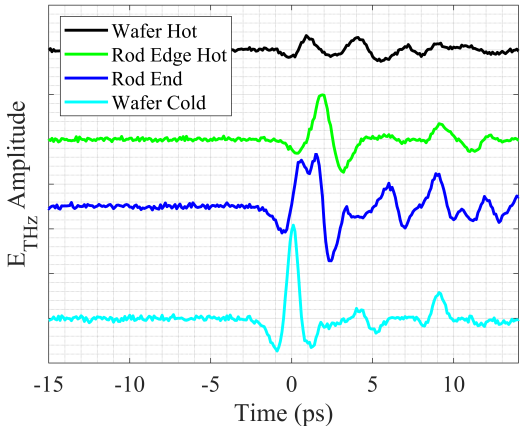

Figure 3.15: The set of time domain spectra is taken from the four regions of the image set that were previously described. The centre of the thermalised carrier region 'Wafer Hot', the end of the rod seen at the centre of the image 'Rod Edge', and the edge of the rod that overlaps with the thermalised region. The reference 'Wafer Cold' is taken from the top of the image far from the thermal region.

the bandwidth of the THz in this region is clearly the largest, comfortably covering the noise floor throughout its frequency range. The region of the hot wafer has significant absorption peaks as an effect of the thermalisation and a greatly restricted bandwidth. Considering that the reference is the same material without hot carriers this spectrum seems an extreme but important look at the effect of thermal carriers in a semiconductor. The rod edge has multiple contributions as evidenced by the many small peaks. The multiple above-crystal sample heights in this region mean that characteristic evidence of GaAs and Si should be present along with strong scattering from the rod edge. This region has a high THz amplitude throughout the frequency range but has a significant absorption peak. A close comparison between thermal GaAs and cold GaAs is seen in part (b). Both material regions have a restricted spectral profile in comparison to the plain wafer (which in this case can be considered a substrate) partly due to the thickness of material in this region attenuating the THz at higher frequencies. However, they each show appreciably unique absorption around the centre of the frequency range with the thermal GaAs having a pronounced lower field amplitude in this part of the frequency range. Onto the transmission spectra in (c) which show low transmission for the thermalised Si wafer across the whole frequency range. The 'Rod End' has an unusual transmission spectrum with huge variation in amplitude centred around the major absorption peak. This complicated shape is the result of the two materials sampled in the region. The

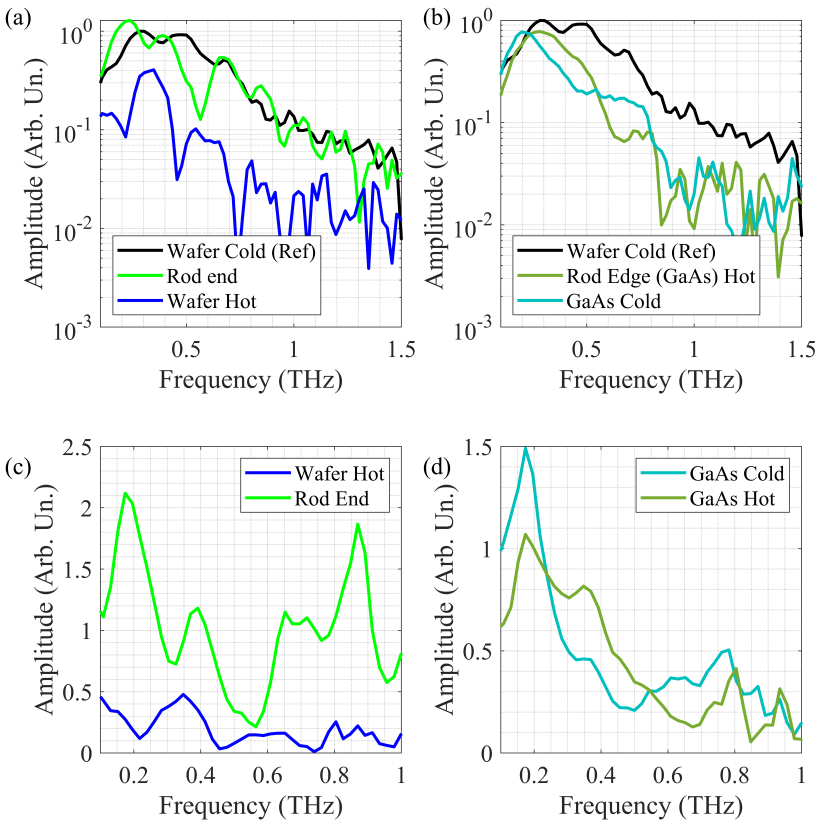

Figure 3.16: These graphs show (a)the frequency domain spectrum of the first 2 sample areas and reference,(b) the frequency domain spectrum of the second 2 areas and reference, (c) the transmission spectrum of the first 2 sample areas, and (d) the transmission spectrum of the second 2 sample areas.

transmission plot in (d) shows that the presence of thermal carriers in GaAs deforms the frequency spectrum, both attenuating it and shifting it slightly, allowing a higher amplitude of mid-frequency components to be transmitted. More detailed analysis of the frequency spectra is beyond the scope of this thesis, however would be very useful for the future of the carrier microscope project.

The Fourier Transform of each pixels' THz evolution can help to indicate the spatial distribution of the THz frequencies when viewed as an image evolution in the frequency domain. The resulting set of images has real and imaginary components but features visible in the real set are not necessarily visible in their corresponding imaginary THz image. The frequency images featured here are not comparisons between real and imaginary components but show where morphological features that can be seen in the time domain are visible in the frequency domain. This helps to indicate the spatial distribution of the

frequency profile without a video presentation of the image set.

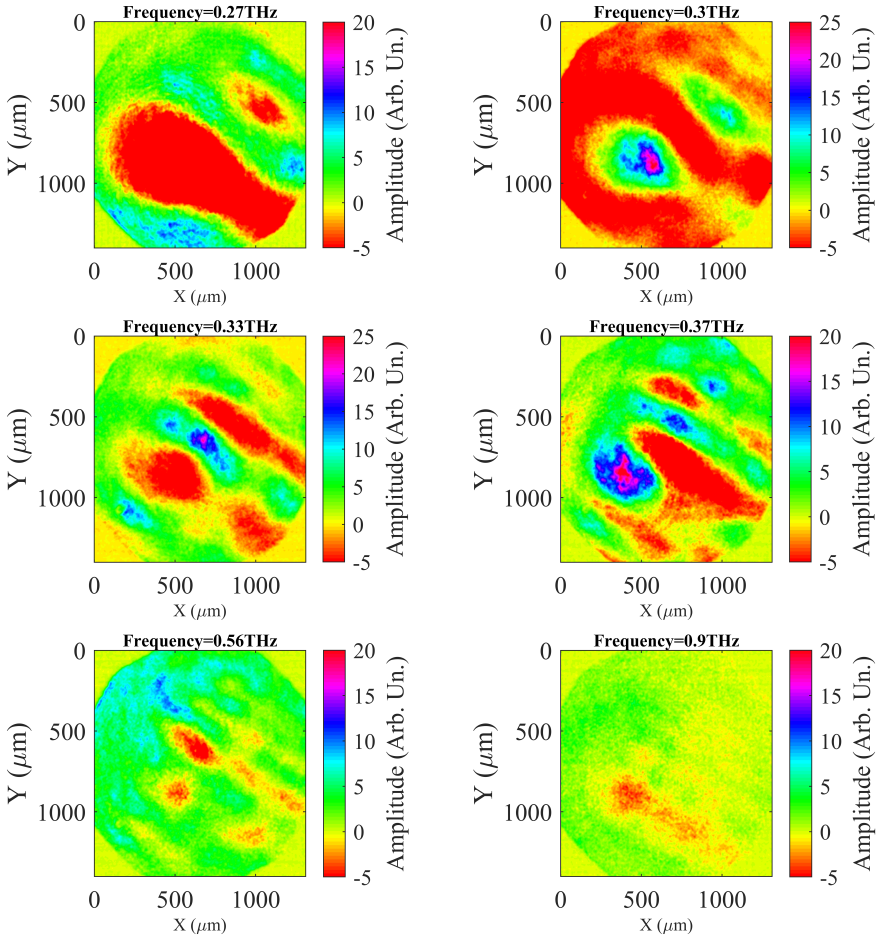

Figure 3.17: The set of images show distinct frequency bins in the real spatial distribution of the frequency profile constructed via pixel-by-pixel Fourier Transforms of the earlier THz time domain image dataset.

As expected the scattered THz is very visible at high frequencies in Fig. 3.17. Scattered components are easily detected in the near field and can be detected at the limits of the detection bandwidth. The imaginary set in Fig 3.18. also shows scattered THz dominating the high frequencies but appears to indicate that the THz regions that have been attenuated by thermal carriers consist of low frequency contributions.

3.3.3 Assessment of Lateral Resolution

In practice the resolution of any 2-D optical measurement is limited by both the diffraction limit of the optical radiation and the pixel size of the 2-D detector. The THz resolution

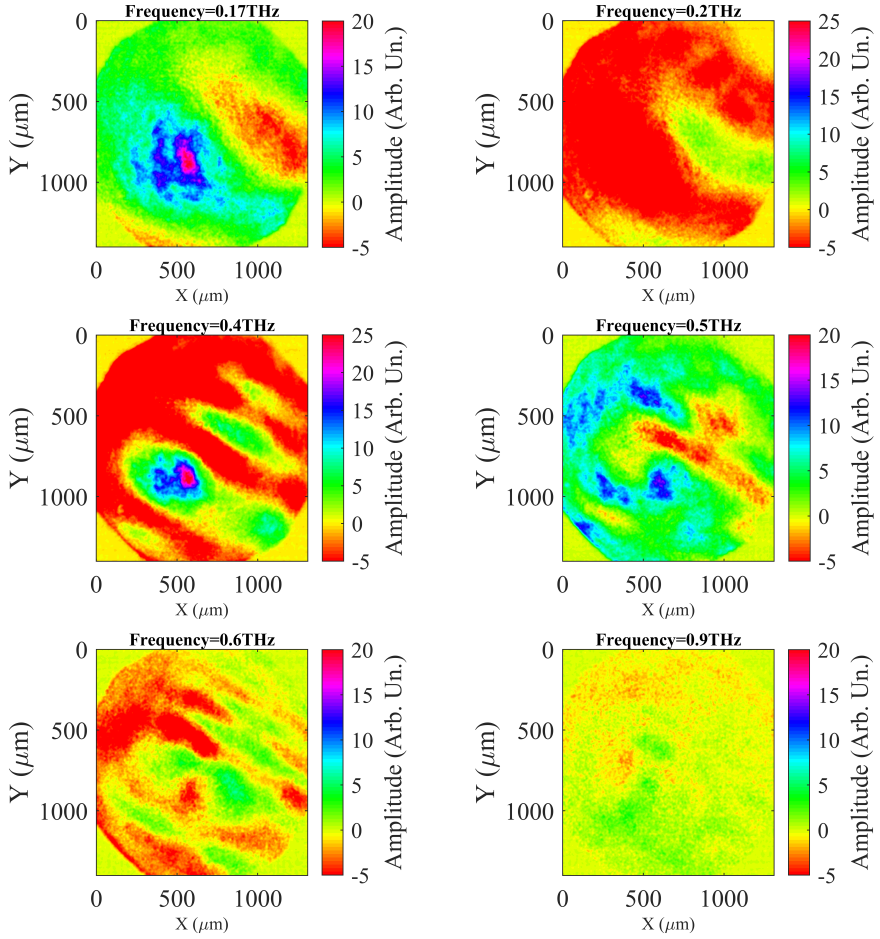

Figure 3.18: The set of images show distinct frequency bins in the imaginary spatial distribution of the frequency profile constructed via pixel-by-pixel Fourier Transforms of the earlier THz time domain image dataset.

can be estimated as a lower bound by selecting the FWHM of a known small feature in the THz image (Chen et al., 2003).

To understand the relationship between the diffraction limit and the sensor resolution it is best to compare the two (Totero-Gongora, 2019) and adjust possible parameters (Siemion, 2021) to match them.

Numerical aperture (NA) of the lens can be expressed as

$$NA = \frac{1}{2f_{\#}} \approx \frac{nD}{2f} \tag{3.1}$$

where $f_{\#}$ is the f-number of the system, n is the refractive index of the object space, D is the lens/aperture diameter and f is the lens focal length. This particular lens is the last lens of the imaging system, which images the beam onto the $CMOS$ detector with a

magnification factor of $M = 1/2$ due to the telescope it is part of (see Fig 2.7).

The Diffraction Limit is the resolution limit of optics as set by Airy diffraction of a two-point source; in a microscope setting it is known as the Abbe diffraction limit.

$$\delta_{x,optical} \approx 2.4\frac{\lambda}{2NA} \tag{3.2}$$

where the wavelength of the radiation is λ. The actual object resolution with magnification is the size of Airy disk after imaging system.

$$\Delta x_{optical} = M * \delta_{x,optical} \tag{3.3}$$

The sensor resolution is defined by Nyquist theorem (Weingarten et al., 1988) with respect to its sampling frequency, the minimum size of its sensor. The smallest object that can be imaged takes up by two pixels, so that

$$\delta_{x,camera} = 2 * \Delta x_{camera} \tag{3.4}$$

Therefore the number of pixels per Airy disk diffraction limit is

$$\frac{\Delta x_{optical}}{\Delta x_{camera}} = M * \frac{\delta_{optical}}{\Delta x_{camera}} \tag{3.5}$$

In the microscope system the value for $\Delta x_{camera} = 4.8\,\mu$m, the lens diameter is $D = 1$ inch, the focal length is $f = 150$ mm, the wavelength is $\lambda = 800$ nm and the refractive index of the glass lens is $n_{lens} = 1.5$. This leaves $NA = 0.127$ and the optical diffraction $\delta_{x,optical} = 7.685\,\mu$m which gives a $\Delta x_{optical} = 3.843\,\mu$m.

By this logic the THz diffraction limit can be written as

$$\Delta x_{THz} = M * \frac{1.22\lambda}{NA} = M * \frac{2.4\lambda f}{nD} \tag{3.6}$$

and assuming the THz wavelength is 4.3×10^{-4} m, $n = 1$ because the focusing optics are parabolic mirrors, the final lens has $f = 50.8$ mm, and once again $D = 1$ inch. The magnification factor of the triple-parabolic lens system (see Fig. 3.1) is $M = 0.042$ in theory $\Delta_{THz} \approx 90\,\mu$m for the THz microscope. This resolution limit is slightly bigger than $\lambda/5$.

3.3.4 THz Microscope Resolution

The measured THz resolution of the THz microscope was extracted from the near-field image of the sample seen in Fig. 3.19. This sample contains sub-wavelength features when

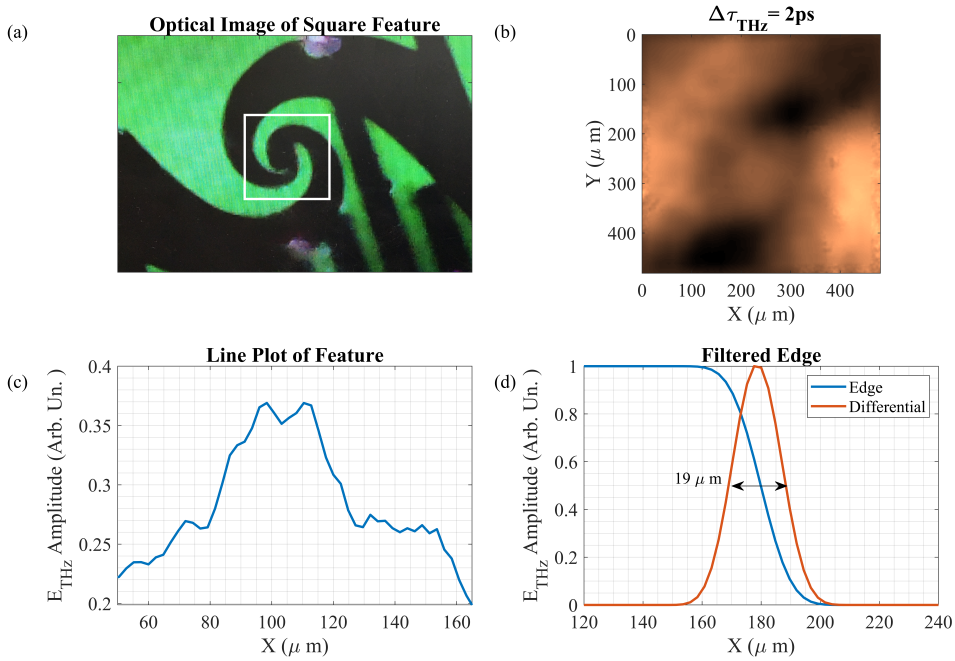

Figure 3.19: An evaluation of features and edges in a THz Microscope image (a) An optical image showing the Germanium square at the centre of a spiral antenna. (b) A THz image of the same feature (c) A line plot of the feature taken from a central cross section of the THz image (d) A plot of the feature's edge along with a differential that indicates the edges' blur.

compared to the peak wavelength of 430 nm including a Germanium square of approximately 30 μm in width and length. From the THz image of this deeply sub-wavelength feature, in Fig 3.16 (b), the lateral resolution was calculated to be $\lambda/22$.

Edge profile analysis of line plots extracted from the THz image set was used to determine the resolution utilising the theory of blurred edges. First the small features of the antenna were found in the THz image set by manually searching through the delayed images. The features were in an unexpected temporal delay - a huge 2 ps after the arrival of the THz pulse. This again illustrates the complexity of THz scattering interactions in subwavelength samples and the problems that can arise from temporal filtering of THz datasets, which could have completely hidden the image. The line plot of the edge was filtered heavily and then bulked at either side with straight line data to help create a neat differential plot. After more smoothing the line plot resembled a blurred Heaviside step function and was then differentiated to create a blurred Dirac delta which in this case resembled a Gaussian function. As the theory goes, the width of this blurred delta gives an indication of the resolution reduction when compared to a perfect edge. This

method is widely used and fairly robust though does only provide an approximation of the resolution. The measured resolution is subwavelength and in line with that of state-of-the-art technologies.

3.4 General Physical Trade-offs in Large-Area Time-Domain Imaging

There are multiple constraints that are involved with building a time-domain imaging system. The first choice made in a field detection setup is often the electro-optic crystal, of which a multitude are available. There are many parameters that a given crystal is selected for including bandwidth, and relevant nonlinear susceptibility coefficient.

As discussed in the introduction, near-field imaging in general requires a small active detection region. With near-field electro-optic sampling this region is formed by a tightly imaged optical pulse upon a thin nonlinear crystal. This can result in trade-offs that are fundamental to operating with THz radiation and nonlinear crystals. There are several factors that influence a user's choice of crystal, and several further factors that influence the choice of length and cut. The mechanism of phononic absorption of THz radiation (Gallot et al., 1999) is often the limiting factor in crystal size. This absorption has a significant limiting effect on the bandwidth of the measurement, though a thicker crystal allows for a stronger signal because the sensitivity of the measurement is greatly improved. This is the basis of the trade-off - measurement sensitivity versus bandwidth. Another significant factor is phase matching of the nonlinear process, where the negative effects of phase mismatch on the frequency response of electro-optic crystals are smaller for thinner crystals (Schall and Jepsen, 2000).

With these factors in mind, an implementation of electro-optic detection with the thin-cut nonlinear crystal Zinc Telluride is fairly appropriate. The crystal is a semiconducting crystal that is only grown at thicknesses larger than 0.1 mm, and exhibits phase matching in a collinear geometry. The crystal texture is unfortunately 'crispy' texture; its growth process results in large air bubbles (Niessen and Markelz, 2013) throughout the crystals.

It is extremely delicate for this reason and small accidental force on its facet causes it to shatter, as seen in Fig. 3.20. Fortunately it is strong enough to support most light microscopy samples. With those factors in mind the crystal is still an excellent electro-optic detection crystal (Wu and Zhang, 1995) and as an emitter provides a large THz bandwidth (Liu et al., 2009). Thin crystals tend to be completely inappropriate for

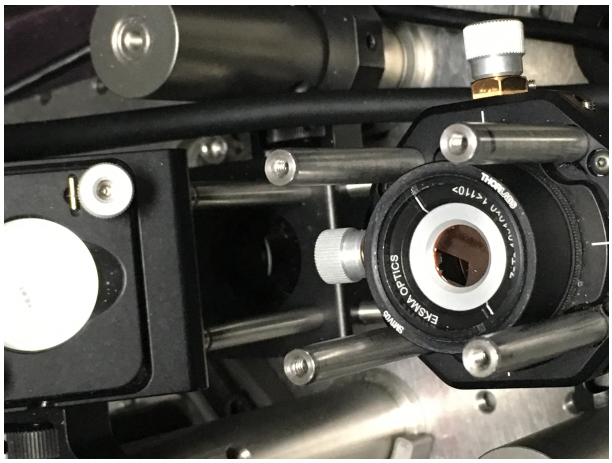

Figure 3.20: An uncoated 0.1 mm ZnTe crystal shattered by a small force on the facet.

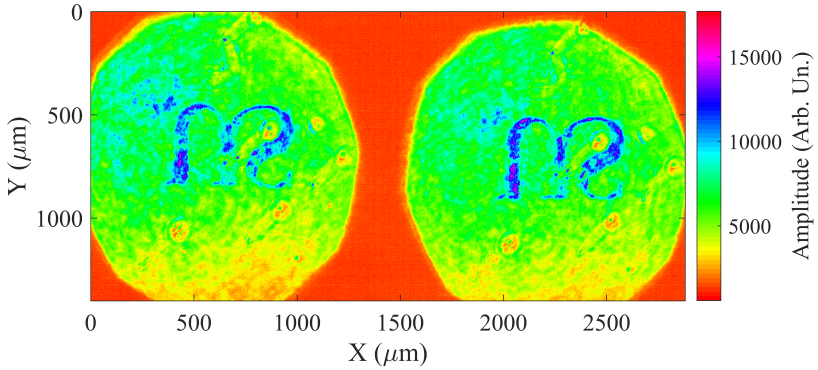

Figure 3.21: Left and Right- circularly polarised probe components imaged into a CMOS. The detection crystal used was uncoated 0.1 mm ZnTe. The sample was gold 'US' printed on a Kapkon substrate.

applied optical coatings due to their fragility. Sampling with an uncoated ZnTe presents a significant problem for 2-D electro-optic sampling because it allows for transmissive propagation of the optical probe in what is by necessity a reflection-geometry setup. In Fig. 3.21 the largest contribution to uneven 2-D electro-optic sampling in uncoated crystals is reflection of the probe from metallic samples when probing the sample in reflection geometry. The morphology of a gold 'University of Sussex' logo is visible in the sub-frames but has significant optical energy present even after background subtraction, which should in theory remove optical contribution before the left-right sub-frame subtraction. Of interest also in this figure are the 'bubble' like ZnTe artefacts which are genuine air bubbles in the crystal that scatter both optical and THz fields due to their shape and structure. In theory metallic samples are opaque to THz (Walther et al., 2007) and this is

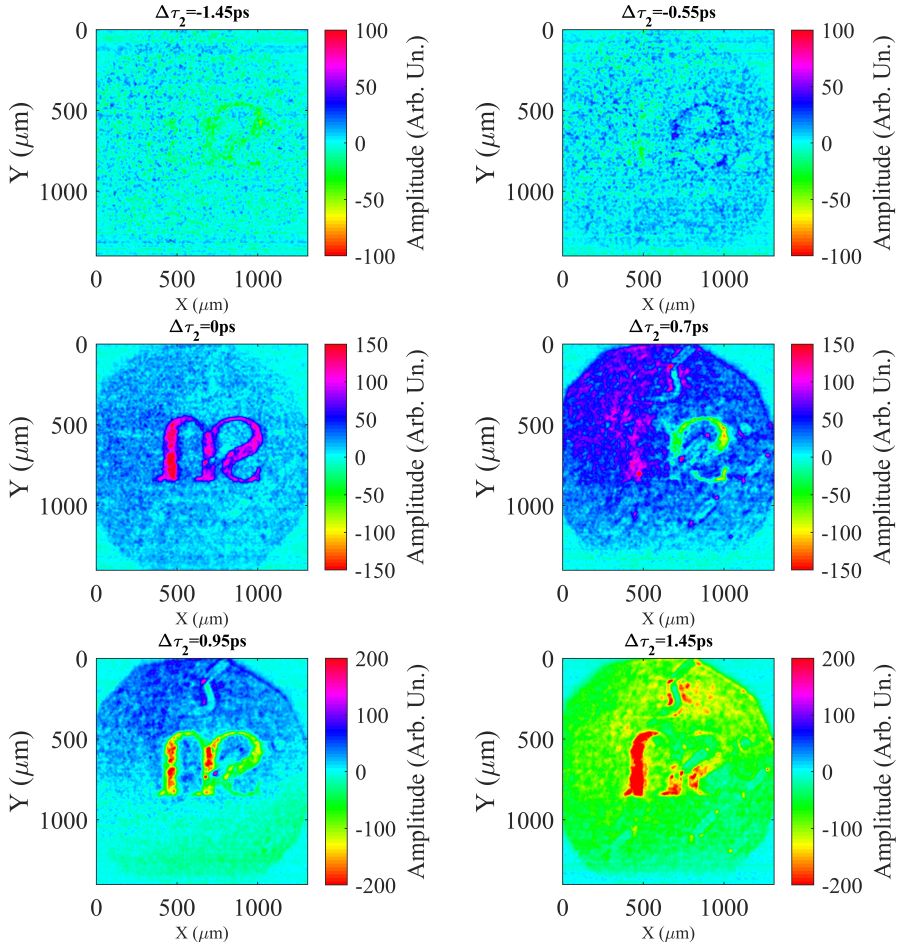

Figure 3.22: Background subtracted polarisation THz Time Domain images of gold 'US' sample. The detection crystal used was an uncoated 0.1 mm ZnTe.

true in practice for a sample of above −nm thickness that is in contact with the detection crystal; it is the latter requirement that is most often not met especially when using thin metallic samples on a plastic substrate. When THz leaks under the substrate it can appear that electro-optic sampling is occurring in the nanometre-thick gold layer, though when this was tested it turned out not to be true. Needless to say, the resulting THz image is not representative of the THz field (Chen et al., 2000), but because of the optical enhancement often represents the sample itself to a high degree of accuracy.

The Fig 3.22 illustrates the time evolution of the THz as it transmits through this sample and undergoes electro-optic probing. The first panel of the Fig. 3.22 shows very little signal at a significant level above the noise floor and therefore indicates that left-right subtraction is effective in eliminating the signal where there is no THz and leaves only a small DC-error component. The logo is immediately visible upon incidence of the THz

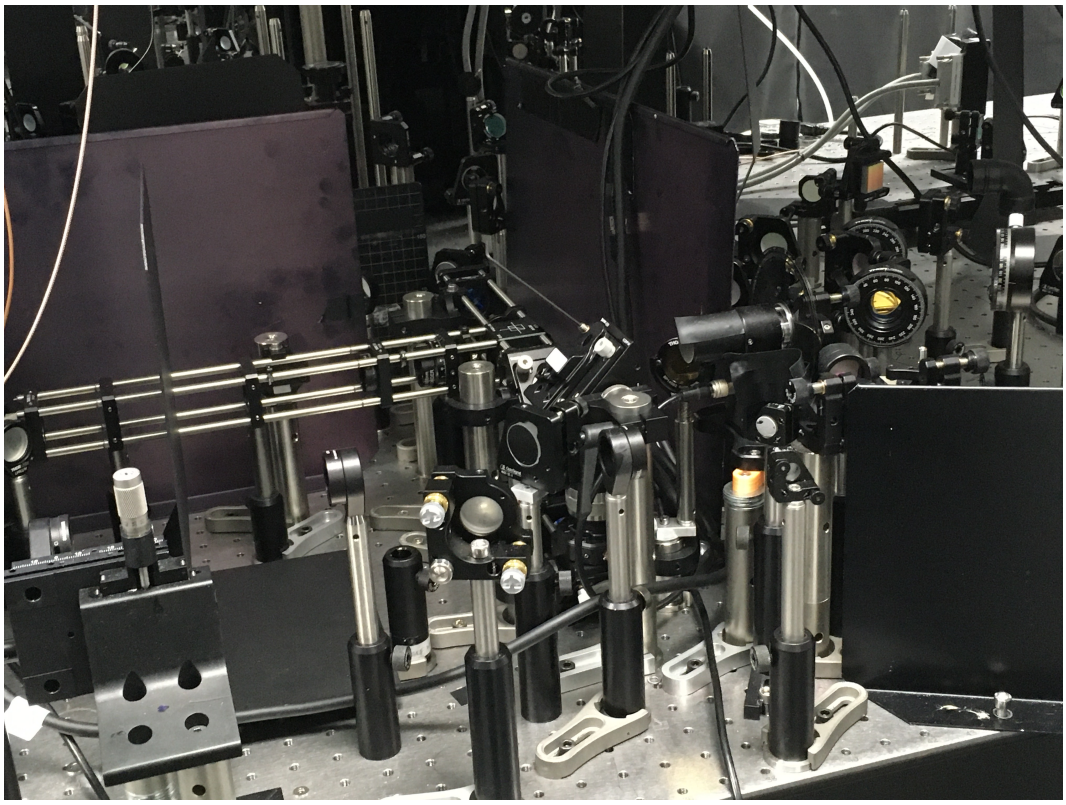

Figure 3.23: Elements of the OP-TNFM microscope setup.

radiation and is significantly brighter than the surrounding regions. The time evolution of the THz shows that the logo itself, which should be opaque to THz, is displaying apparent THz transmission that temporally precedes the field peak and possesses a signal level that lies consistently at a higher amplitude than the surrounding plastic region.

3.4.1 Imaging Artefacts

In highly monochromatic optical images artefacts can be present from a number of sources. Periscope and reflection imaging setups contain hundreds of glass and silver-coated components - some are shown in Fig.3.23 - which can end up covered in statically attracted dust and particles from the room.

In a semi-clean environment without air filtration uncovered components can become physically marked over time by the presence of these contaminants especially when dust is blown between setups by users. Dust and related particles are often barely visible optically in the near field but if interacting light is allowed to propagate then contaminants will be present as point (Airy) diffraction patterns in a confocal image. Because the Airy pattern is clearly visible this means that the image contains visible intensity rings, introducing a non-Gaussian intensity profile. Similarly, there are other causes of artefacts. When

imaging with Zinc Telluride the materials characteristic 'bubbles' are visible in the optical and THz image (Niessen and Markelz, 2013) due to their diffractive properties. Other crystals will contain air as part of their growth process and these will leave a similar small round profile in the image because the crystal itself lies in the imaging plane. The only way to avoid this type of artefact is manual removal in post processing or careful selection of the crystal sampling area. Sometimes high-strength optical fields will thermally damage glass components (Marouf, 2021); this can occur when accidentally focusing the field in a material. This artefact is often too large to manually remove and the component must be replaced. Similarly scratches on optical components will result in linear diffraction patterns. Each of the described artefacts results in intensity fringes when viewed in a distant imaging plane, or distinct shapes when close to a focal plane, as seen in Fig. 3.22. In this work the artefacts present in THz carrier images are corrected in post processing by creating a model of the true field which is assumed to be Gaussian. In a rather brute-force fashion a Gaussian filter is applied to the carrier-free image and treated as a representation of the true field. This filtered image is used to create a multiplicative mask for the subsequent images and introduces a significant visual improvement.

3.4.2 Extracting Transmission and Spectral Properties

Utilising large area illumination can cause challenges when extracting transmission and spectral properties from THz Images. Regions far from the Gaussian centre may have lower field amplitude than regions in the centre; this is unfortunate if the sample causes scattering from a central location as the only clean reference is located at the image edge. A map of the THz Gaussian distribution at the peak field would be useful in removing the amplitude effect and allowing spectral transmission to be calculated. The problem is that samples and scattering obscure the true shape of the THz. This poses fewer problems if the reference scalar value is taken far from the sample; at the peak of the THz and before the scattering occurs this area can be compared to the peak in the image distribution. This method is used in later analysis to correct transmission values. Another potential approach to this is frequency analysis of the imaging set. Assuming that the scattered elements will occupy the high frequencies of the image set in the frequency domain it is prudent to assume that spectral filtering will remove scattered elements. Frequency analysis of the THz images is included in a later chapter which confirms that scattered elements occupy the high frequencies of the spectrum. Unfortunately low-order scattering is present in the low frequency images. More complex analysis would be required to approximate the area

covered by the sample and without it the spectrally filtered THz is not useful in correcting the transmission.

3.4.3 Implementation of Synchronous Sampling

In order to take an electro-optic measurement at the time of pulse interaction several measures are taken both in hardware and software. The pulses are temporally aligned at the detection system by careful placement of the translation stages, the distances between each pulses respective origin and the detection system being set as equal, to 50 μm accuracy. Any time delay measurement needs to have multiple points in time, surrounding the time of interception between the pulses and at least enough in number to reach the Nyquist-Shannon sampling limit. Sampling a repeating waveform is known as synchronous sampling if it is time-domain (or harmonic mixing if frequency domain) Weingarten et al. (1988) where the repeating waveform is in this case the 1 kHz output of a regenerative amplifier. Averaging is a simple way to increase the SNR of a measurement system (Jiang et al., 2000), and by retarding the probe pulse by the variable delay $\Delta\tau_2$ subsequent parts of the waveform can be sampled. The sampling frequency of the THz waveform must be chosen carefully Keiber et al. (2016) to accurately reconstruct the physical field dynamics. According to the Nyquist-Shannon rate, the fundamental minimum rate that electronic sampling can be performed at to accurately reconstruct a signal (Weingarten et al., 1988), a THz pulse can be sampled at

$$SamplingRate = 2 \times Bandwidth_{THz} \tag{3.7}$$

which in practice is around 1 ps of temporal sampling distance for the type of pulse used in this work. This limit refers to the sampling rate required to accurately reconstruct a signal; disregarding techniques that are designed to achieve under-sampling this is a fundamental property of electronic sampling, especially when attempting to electronically sample optical fields. The exposure setting on a camera determines the length of its sampling window. As a $CMOS$ array sensor, it is merely sampling the intensity of a set number of pulses, which is determined by the sampling window length. Maximising the number of pulses in the sampling window allows for noise reduction through averaging, one of the simplest techniques to increase signal-to-noise ratio. The cue for the camera to start the sampling window is an electronic trigger, a square pulse of around 5 V peak to peak.

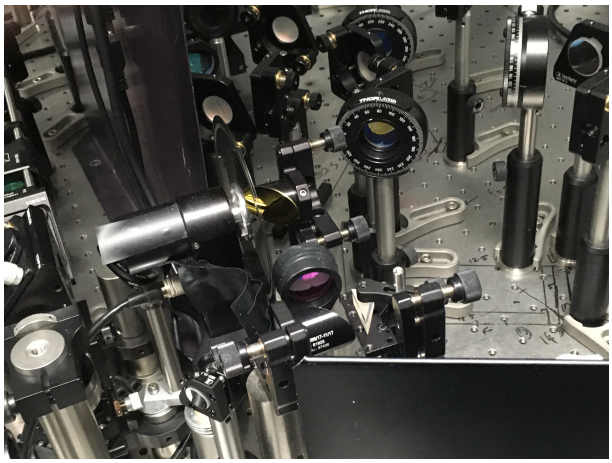

Figure 3.24: A mechanical chopper placed in the path of a THz beam to allow for dynamic subtraction.

If this electronic pulse is synchronised to the laser pulse and has a frequency that is a a multiple of the laser pulse frequency, then there will be a set number of laser pulses per electronic trigger, and thus per camera sampling window. If this is equal then it provides a long term consistent sampling of binned pulse intensity. The bin size being a 1 to 16 bit value, which can be scaled by a calibrated measurement with a power meter. However, the noise inherent in the camera system makes up a large portion of the bits in each array pixel. Thus, averaging is needed to ensure that each 'bin is filled' past this dead value, preferably significantly enough that the value of the bin can be said to be due to the energy on the sensor array rather than random electronic or thermal fluctuations.

3.4.4 Noise reduction in Electro-Optic Sampling

Even a dynamic subtraction technique - a 'differential measurement' between the beam under the influence of an electro-optic effect and the beam free of this influence - can show some evidence of second order processes. Using a dynamic subtraction method (Jiang et al., 2000) assumes that subtraction between the left and right images is sufficient to remove the optical beam influence in theory. This is the same as assuming a linear relationship between the electro-optic response to the THz in the crystal and the optical field from the probe pulse, which is a fundamental assumption to dynamic subtraction, discounting the term corresponding to long-term optical drift (Jiang et al., 2000). This assumption ensures that only the birefringence contribution from the THz field is recorded in the final image, and the optical morphology is of the order of the noise floor. Dynamic subtraction offers a massive reduction in the noise of the final image, effectively subtracting

the noise of the probing beam by use of a large chopping blade as seen in Fig. 3.24. This can be extremely useful when the probing beam is inhomogeneous due to far-field scattering from objects in the beam path. This is just one technique for reduction of noise in these images, the main other being averaging and filtering, in order to also reduce scattered light that can cause noise. Unfortunately lock-in detection cannot be used with an array sensor, even in theory, because the noise has the same chopping frequency as the desired signal (Mickan et al., 2000). In general lock-in detection applies a strict bandpass filter around the signal which has frequency matching a separate reference, and therefore is one of the most effective pre-processing strategies to reduce noise in a single pixel measurement. In post-processing, bandpass filtering a set of THz images is possible. The 'wrong' frequencies to cut out would include high frequency components, as although these can be present due to noise they often contain diffracted elements from various parts of the sample-field interaction region. This type of filtering produced modest effects on the results of this experiment, perhaps indication that the reduction of physical noise sources from other parts of the experiment would be more effective at improving image quality.

Chapter 4

Nonlinear Ghost Imaging

In the introduction we presented the Ghost Imaging as a technique that fundamentally translates the complexity of an imaging process in space in the way a sample is illuminated, as opposed to regular array-sensor that allows the detection of the spatial feature of an object scattering an homogeneous illumination. In a sketch-example, the principle is often referred as the ability to perform the imaging of tree taking a picture of the sun. By sampling an object with *patterns* of light and collecting some average scattering properties (e.g. the average power), it is possible to infer the object image. The computational GI algorithm can be expressed as

$$G^{(2)} = \frac{1}{N}\sum_{i=1}^{N}(Io_i - \langle Io\rangle)Ii(x,y) \tag{4.1}$$

Liu (2020) where Io_i is the single pixel object signal,$Ii(x,y)$ is the pre-computed intensity spatial distribution and $\langle Io\rangle$ is the object DC background average. The sum over N is the ensemble average of patterns. In terms of information theory, this process trivially represents the determination of the value of the scalar product of several orthogonal (or quasi-orthogonal) distributions with the image (Ragy and Adesso, 2012).

From an experimental point, we observe immediately that the application of the GI implies the ability of spatially-modulating illuminations. This is not trivial at terahertz frequency because of the lack of a standard spatial-light-modulator technology (Chan et al., 2008). Most importantly, terahertz time-domain spectroscopy detects fields and not intensities, which means that a GI application in this domain is fundamentally challenged by significantly different physics. Last, the terahertz diffraction length is relatively short (Baillergeau et al., 2016), which means that the resolution of any diffracting system applying the GI to obtain an image would be coarser than the large terahertz wavelength. Although implementation of the GI has been proposed to access the near-field domain

(Stantchev et al., 2016), they are generally challenged by limited fidelity in collecting the spectral fingerprint of microscopic features, objective at the very core of terahertz microscopy. This problem descends from the physics of propagation at sub-wavelength scales, which mixes spatial and temporal information in a remarkably complex fashion (Olivieri et al., 2018). The nonlinear ghost imaging is a GI-inspired methodology that embeds nonlinear transformations in order to address all those challenges.

4.1 Terahertz Ghost Imaging Implementation

The NGI operates on the following hypotheses: (i) an object is placed in the proximity of a terahertz source distribution obtained via optical rectification from an optical field distribution (ii) the source is sufficiently thin for the terahertz spatial morphology to maintain features spatially defined within the optical diffraction limit, i.e. much smaller than the terahertz wavelength (iii) an electro-optic field detection allows for the time-domain spectroscopy of the average field scattered (iv) an imaging system transfers a spatial mask onto the pump at the generation plane of the crystal. The spatial patterns are applied to the pump beam by use of a Digital Micromirror Device (DMD), i.e. implementing a binary encoding of the intensity, i.e. of the terahertz pattern.

The algorithm is a crucial component and is modified for NGI with respect to the normal GI; it utilises a TDS measurement and replaces the field intensity with a time-dependent average The reconstruction of the image can be expressed analytically via the spatiotemporal transfer function $T(x, y, t)$

$$T(x, y, t) = \langle C_n(t) P_n(x, y) \rangle_n - \langle C_n(t) \rangle_n \langle P_n(x, y) \rangle_n \tag{4.2}$$

where $P_n(x, y)$ is the $n-th$ spatial pattern and the angled brackets represent the ensemble average. $C_n(t)$ represents the average of the field detected after transmission through the sample, i.e.

$$C_n(t) = \int dx\, dy\, T(x, y, t) * E_n^-(x, y, t) \tag{4.3}$$

and contain dependencies on the term $E_n^-(x, y, t)$ which is the electromagnetic field impinging on the object. The integrand is in this case the direct measurement of the electric field via electro-optic sampling, performed at the center of an optical Fourier plane, which corresponds to the field component of transverse momentum $k_x = k_y = 0$.

4.1.1 Nonlinear Ghost Imaging Experimental Setting

The NGI setup is designed to imprint binary patterns onto an ultrafast optical beam which is projected onto a nonlinear crystal surface. Although there are a number of possible implementations, probably the most straightforward implies placing an spatial intensity modulator intercepting a large collimated beam and then project the image of the modulator surface plane onto the crystal. The Fig. 4.1 shows a typical embodiment of

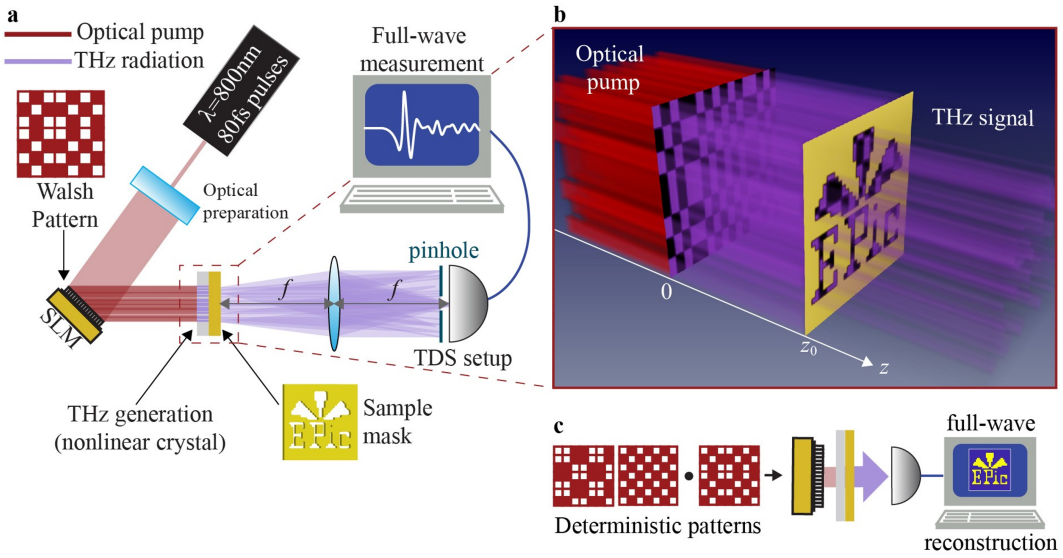

Figure 4.1: (a) Basic equipment setup and THz patterning methodology for Nonlinear Ghost Imaging (b) Illustration of THz patterning and algorithmic reconstruction.

a NGI setup, showing the basic elements that are required to produce an image, including the DMD and the full wave reconstruction (the assembly of the projection system is not sketched to avoid cluttering).

Interestingly, the optical rectification process exploited for terahertz generation, imposes that the generated terahertz field is linearly dependent from the optical intensity in a specific generation plane.

$$E_{THz}(x,y,t) \propto \chi^{(2)} I_{opt}(x,y,t) \tag{4.4}$$

where the intensity mask of the optical pump is $I_{opt}(x,y,t)$. To optically create the patterned pump, optical pulses of sub- mJ energy were first clipped with an iris to create a profile close to a flat-top. While maintaining focal geometry, the beam is enlarged with a Galilean telescope and imaged onto the Dynamic Mirror Device, then imaged once again and enlarged with a magnifying lens pair onto a 0.2 mm ZnTe crystal to generate THz by optical rectification. To understand the issues that sub-wavelength illumination can

introduce, a visual graphic can be useful. The Fig. 4.2. is an illustration of this patterned THz propagating through air, which occurs in the setup between the generation and detection. The plot shows the spatio-temporal coupling that occurs when THz radiation, especially patterned THz, is allowed to propagate. This propagation encodes information on the medium. The generated THz is collected by a large aperture parabolic mirrorand

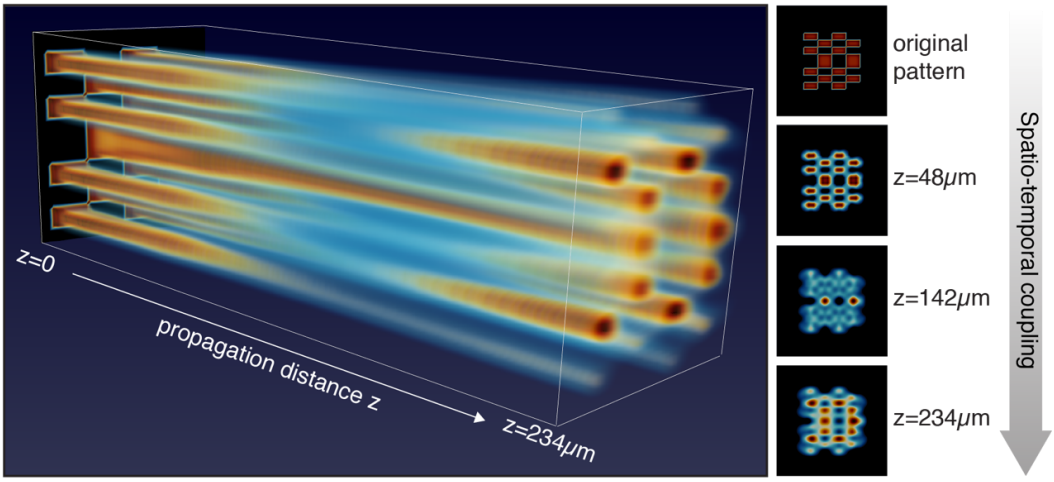

Figure 4.2: Volumetric plot illustrating the generation the essence of the sub-wavelength spatio-temporal coupling. Insets showing the pattern spatial features at different propagation length.

collimated, where it is measured at the point of the profile's conjugate transform. This ensures that the 'zeroth-order' element in the plane of the conjugate transform is measured. In this plane higher order frequency-space or k-space elements are distributed away from the axial centre of the focal distribution. The central element is considered to contain the average field and can be sampled with a small lateral detection region. This enables for single-pixel measurement which is in this case performed with standard electro-optic sampling, using a ZnTe crystal of medium thickness to account for the tradeoff between measurement sensitivity and bandwidth that was mentioned in the previous chapter.

The DMD is an intensity modulator that consists of mirror pixels which can be set to an 'on' or 'off' state. This directs or diverts energy in a desired direction. Replacing the DMD with a Spatial Light Modulator (SLM) allows for full phase modulation of the incident optical pulse (Turtaev et al., 2017) which prevents the losses that occur from the non-zero diffractive orders and 'off' pixels of the DMD. Though the liquid crystal modulator of the SLM is generally slower that the DMD, it potentially allows for a higher generation efficiency and greater control over the THz profile. The SLM exploits phase modulation that is converted to amplitude modulation in a far-field Fourier plane, so

the input masks need to be transformed before input in order to be reproduced at the far plane. This problem generally involves a Fourier propagation problem which can be computationally taxing, making the SLM a more difficult module to implement.

4.1.2 Spatio-Temporal Coupling and Inverse Propagation

The general modeling of the NGI starts from the assumption of a pure spatial light modulation of a ultrashort optical pulse of temporal waveform $f(t)$, i.e. an optical illumination $\vec{E}_n^{opt}(x,y,t)$ (Olivieri et al. (2018)) of the form:

$$\vec{E}_n^{opt}(x,y,t) = H_n(x,y)f(t)\hat{\mathbf{p}} \tag{4.5}$$

$H_n(x,y)$ is the Walsh-ordered Hadamard pattern, $f(t)$ is the temporal profile and $\hat{\mathbf{p}}$ is the beam polarisation unit vector. This type of pattern was mentioned and demonstrated in the Introduction, but the specific Walsh ordering was selected for image quality in this application (Vaz et al., 2020). At the crystal plane, where nonlinear generation occurs the optical beam induces a nonlinear polarisation of the form

$$\overleftrightarrow{P}_n(x,y,t) = \epsilon_0 \chi^{(2)}(\Omega; \omega+\Omega, -\omega)|\vec{E}_n^{opt}(x,y,t)|^2 \tag{4.6}$$

for a generation co-polarised with the impinging beam, the terahertz field can be expressed as

$$\vec{E}_n^{THz}(x,y,z=0,t) \propto \partial_t^2 \vec{P}_n(x,y,t) \tag{4.7}$$

From the generation plane, the THz wave undergoes a transformation via propagation driven by the local point spread function expressed in the near-field domain

$$\vec{E}_n^{-}(x,y,z,t) = \overleftrightarrow{G} * \vec{E}_n^{THz}(x,y,z=0,t). \tag{4.8}$$

$\overleftrightarrow{G}(x,y,z,t)$ is the Dyadic Green's tensor, and shows that the field dynamics involved the full spatio-temporal domain. The field transmitted through the object is then

$$\vec{E}_n^{+}(x,y,z_0+\epsilon,t) = T(x,y,t) * \vec{E}_n^{-}(x,y,z_0-\epsilon,t). \tag{4.9}$$

$\vec{E}_n^{-}$ is, then, the field immediately before the sample, $\vec{E}_n^{+}$ is the field immediately after, and ϵ represents a perturbative spatial displacement. Under these conditions the TDS signal for the transmitted field is

$$\vec{E}_n^{TDS}(t) = \int dx\, dy\, \mathbf{p}_{TDS} \cdot \vec{E}_n^{+}(x,y,t). \tag{4.10}$$

$\mathbf{p}_{TDS}$ is the detection polarisation state, controllable by rotation of a waveplate when the propagated field is detected with electro-optic sampling. The substitution of (4.9) and (4.8) into (4.3) yields

$$C_n(t) = \int dx\, dy\, \mathbf{p}_{TDS} \cdot T(x,y,t) * [\overleftrightarrow{G}(x,y,z,t) * \vec{E}_n^{THz}(x,y,z=0,t)]. \tag{4.11}$$

$C_n(t)$ coincides with single pixel TDS signal at the centre of a Fourier plane. Its specific form implies that it is the distance-propagated pattern that generate the THz field exploited at the measuring plane, causing the interacted THz field to significantly differ from the simple spatial modulation imposed to the pump beam. The reconstructed transfer function should be considered to be

$$T' = T * G \tag{4.12}$$

which includes the effect of this propagation. It is easy to conclude that T' (the measurement) does not represent the sample fingerprint, and the approximation $T' = T$ brings in a complex aberrations of the signal which is negligible for extremely thin sample and emitter, but it is not trivially quantifiable in a given measurement.

Interestingly, in equations (4.9) and (4.10) can be inverted, executing what it is in jargon known as *back-propagation*. In essence T' still contains the full space-time information. This inversion originates a relation in the form of a Wiener-like filter applied to the measured THz field Olivieri et al. (2018).

$$W(K_x,k_y,k_z,\omega) = \frac{\overleftrightarrow{G}(k_x,k_y,k_z,\omega)^*}{|\overleftrightarrow{G}(k_x,k_y,k_z,\omega)|^2 + \alpha * NSR(k_x,k_y,k_z,\omega)} \tag{4.13}$$

$\overleftrightarrow{G}(k_x,k_y,k_z,\omega)$ is the Dyadic Green's Function in the Fourier Domain, NSR is the average noise-to-signal ratio, and α is a scaling factor. The NSR term has the role of quenching the back propagation (introducing inaccuracies) in order to avoid the amplification of noise components in the reconstructed field.

4.2 Nonlinear Ghost Imaging Demonstrations

The demonstrations included in this section are part of published works on the NGI methodology. The figure 4.3 shows the basic concept of the NGI in a visual format that re-emphasises the steps that the methodology consists of and the stages within the experimental cycle at which they are implemented. Figure 4.4 is the spatiotemporal image of a

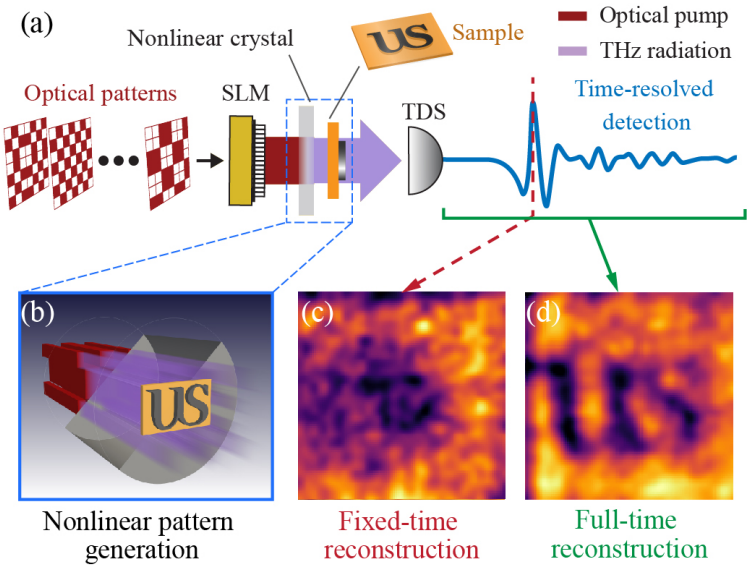

Figure 4.3: Conceptual description of the TNGI approach from Olivieri et al. (2020). (a) Key experimental components and methodology; (b) volumetric representation of the nonlinear generation of THz patterns; (c) fixed-time reconstruction with a field of view 2mm × 2mm and 32 × 32 spatial sampling; (d) backpropagated hyperspectral image, averaged between 1 and 2 THz.

gold structure on a 50 μm Kapkon plastic substrate. The fixed-time images demonstrate complex THz resonances that can be seen to develop over time. The resolution achieved in the image set is between 50 μm and 100 μm, which is lower than the pixel size at 125 μm; this means that the NGI method has successfully demonstrated the proposed spatial undersampling in the image plane. This is despite the 1 mm thick ZnTe detection crystal limiting the resolution. Fig. 4.5 shows an NGI image of a leaf, a semi-transparent sample, through various stages of dehydration at room-temperature. A hyperspectral intensity and phase image of the leaf is achieved by fixed-time reconstruction and fixed-frequency reconstruction. This image demonstrates the changes in spectral phase and intensity that result from changes in hydration of fresh samples.

Fig. 4.6 is taken with a slightly altered sample placement. The sample is now placed a distance z from the emitting crystal. Now the propagation of the THz pulse after the sample affects the fixed-time reconstructed image, obscuring sample morphology. Even the hyperspectral image is affected due to the pattern propagation - a direct consequence of spatio-temporal coupling. The reversal of spatio-temporal coupling that results from applying the inverse-propagation filter allows for an accurate resolution of the field morphology in the region of the sample.

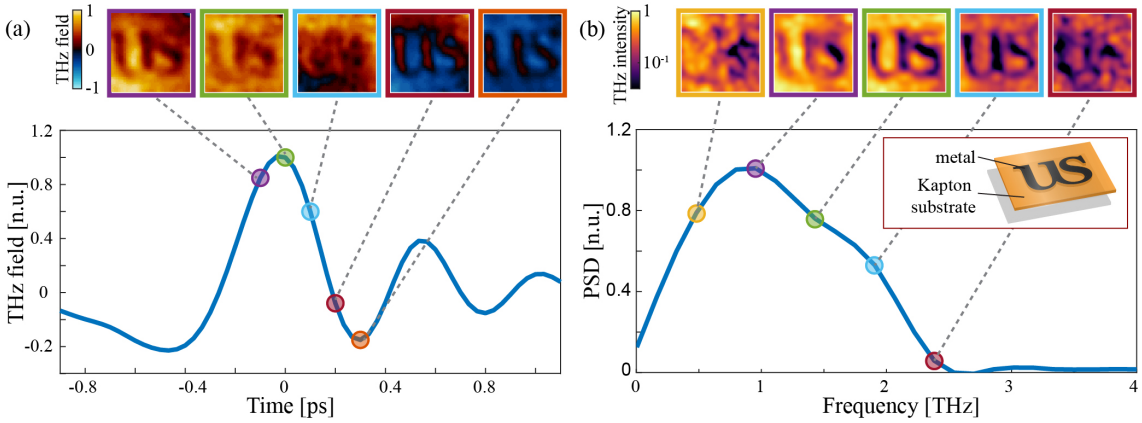

Figure 4.4: Spatiotemporal image of a metallic sample from Olivieri et al. (2020). (a) Temporal response of the metallic sample with fixed-time image reconstructions. It is worth noting that field evolution (color change) can be appreciated underneath the metallic mask as the structure resonance produces a secondary emission. (b) Spectral response with hyperspectral images. The field of view was 2 mm $\times$ 2 mm with a 16×16 spatial sampling.

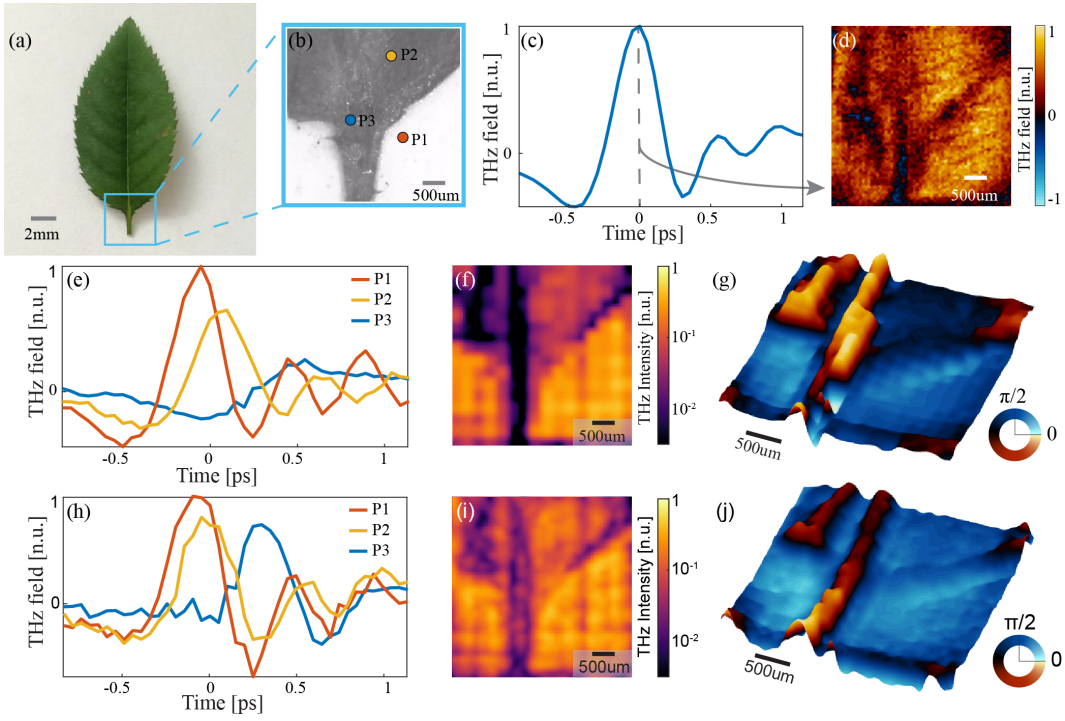

Figure 4.5: Hyperspectral image of a leaf From Olivieri et al. (2020). (a) Optical image of the leaf; (b) microscope image; (c) temporal response of the field transmitted by the leaf; (d) fixed-time reconstruction (128 pixels × 128 pixels); (e) local temporal response of the fresh leaf in the points indicated in (b); (f) hyperspectral image of a fresh leaf at 1.5 THz (16 pixels × 16 pixels); (g) phase image of the fresh leaf, obtained without phase unwrapping of the experimental data; (h)–(j) same as the previous panel for a dried leaf (32 pixel × 32 pixel images). All the images correspond to a field of view of 4 mm × 4 mm.

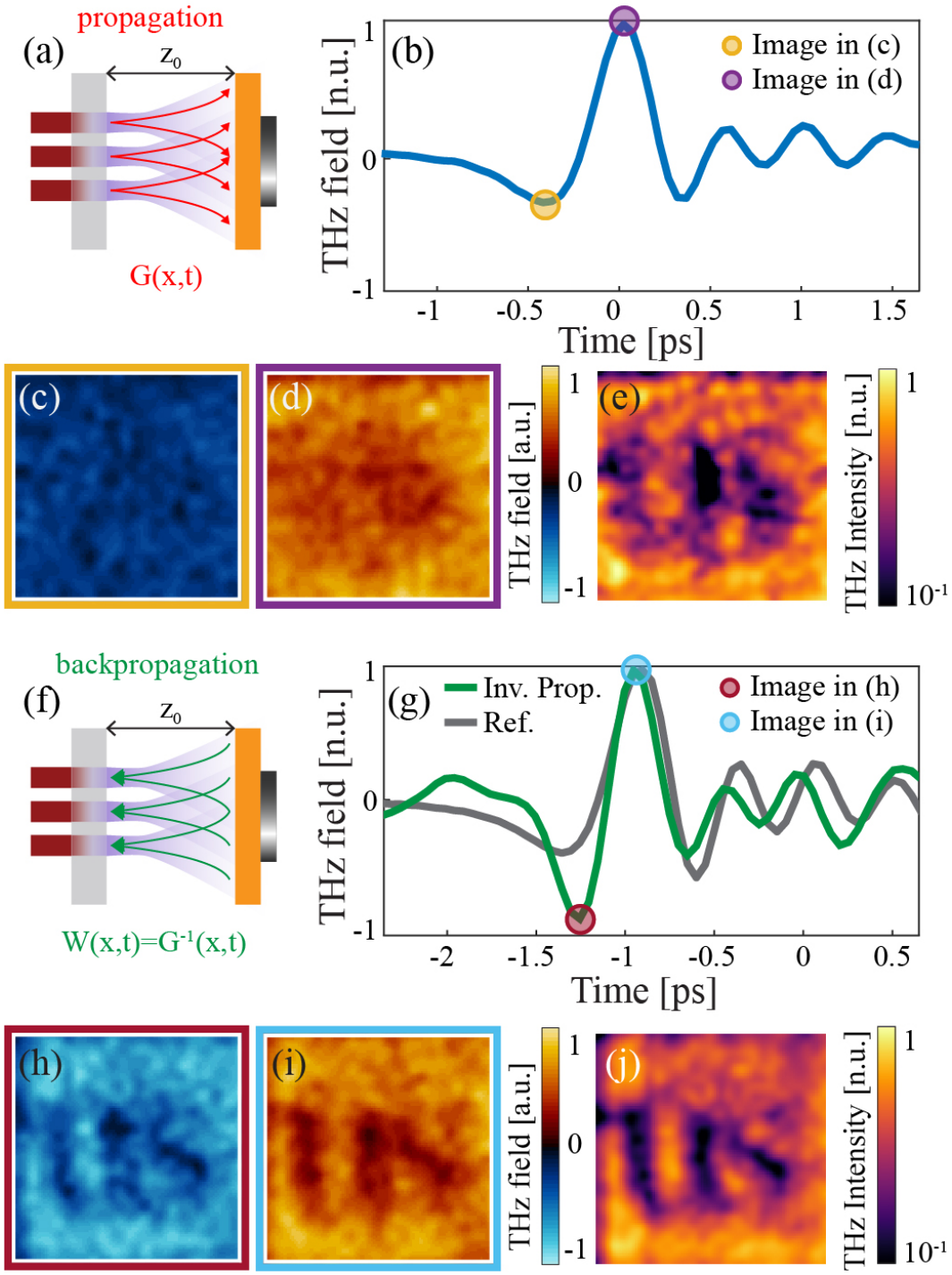

Figure 4.6: Time-resolved image reconstruction (from Olivieri et al. (2020)): inverse propagation approach. (a) Conceptual illustration of the propagating imaging scheme: the sample is placed at $z_0 = 300\,\mu$m from the crystal. (b) Temporal response of the sample; (c)–(d) fixed-time reconstructed images at the points indicated in (b); (e) hyperspectral image averaged between 1 and 2 THz; (f) conceptual illustration of the back-propagation scheme; (g) temporal response of the back-propagated image (green) and the temporal response without the sample (gray); (h)–(i) fixed-time reconstruction of the back-propagated image at the points indicated in (g); (j) back-propagated hyperspectral image, averaged between 1 and 2 THz. In all panels, the field of view was 2 mm × 2 mm with a 32 × 32 spatial sampling.

Chapter 5

Conclusions and Perspective

5.1 The Impact of Terahertz Time-Domain Imaging

In order to appreciate the impact of the progress in Terahertz Time-Domain imaging and, more specifically, the role of this work in advancing the state of the art, a parallel with the evolution of optical imaging (and more in general of the Photonics field at large) might be able to provide some insight.

As many other technologies, Time-Domain Spectroscopy has been driven by the ability of terahertz to see beyond prior technological limits. TDS did not simply cover a new portion of the spectrum; besides, THz spectroscopy using incoherent or synchrotron light sources largely predates TDS. What TDS did was to expose the electric field as a measurable quantity. Hence, although those techniques clearly descend from the photonics of ultrafast pulses, this specific quality immediately identified a very different experimental framework. The possibility of measuring fields in ultra-fast transients along the *time* axis enabled new abilities and therefore applications. In Photonics jargon, we refer to this as the ability to reconstruct spectral amplitude and phase of a field, generally quite challenging in Photonics. Interestingly, we can argue that *time* is epistemologically broader than *phase*. This gave time-domain terahertz all the specifications of an alternative research topics. We can appreciate the same difference between Terahertz Time-Domain imaging, which is fundamentally a 3-dimensional space-time methodology, and classical imaging approaches.

Following this trend, we can discern how Terahertz Time-Domain Microscopy is conceptually very different in construction when compared to optical microscopy, although carrying similar name. From a traditional photonics position, to exploit terahertz microscopy we need to circumvent the diffraction limit imposed by the long wavelength. From another

and less traditional perspective, we are imaging fields, which means that any reference to standard microscopy, based on collecting light intensity, is dropped. This implies the need of novel physical understanding (which this thesis contributes to).

5.2 The impact and the future of the Optical Pump-Terahertz Near-Field Microscopy

The Optical Pump-Terahertz Near-Field Microscopy is the first imaging technique of its kind but responds to a very common need of physical probing in material science: the ability to image hot-carrier dynamics. The methodology offers (i) the ability of terahertz to interact classically with free carriers (ii) the sub-wavelength resolution required to discern technological devices (iii) the speed to process around one million pixels per frame at video frame-rate (iv) the ability to excite hot electrons in an arbitrary geometry. All of those properties exists in previous embodiments, but not together. Yet, we can argue that removing even a single one requires acceptance of a restricted hypothesis and we can certainly argue that (ii) is required to actually resolve small devices with terahertz. Some of the carrier images produced in this thesis are, in fact, the first images available in the art with all these features and, therefore, novel scientific and technical questions arise from this achievement. As the nonlinear ghost imaging spot-lighted, the image of carriers dynamics at very high resolution is fundamentally entangled in the space-time. This means that when you look at the scattered terahertz field as expression of the transient of the local dielectric response, some of the information might not be directly visible. The NGI can retrieve the spectral fingerprint of scattered field even in this scenario. Hence a valid scientific question is whether this approach can increase the fidelity in reconstructing the carrier dynamics of spatial distribution in heterogeneous structures. In my view, this is the next challenge for this topic. At the time of writing, my main publication on the topic is still in preparation, hence it might contain a more developed vision of this aspect.

5.3 The impact and the future of the Nonlinear Ghost Imaging

The Nonlinear Ghost Imaging is not only the proof that a Ghost Imaging protocol can be used to reconstruct terahertz images using a single-pixel setting. It is the demonstration that when we exceed the diffraction limit, the information of the field scattered from an object has a complex entanglement in space-time. This has enormous practical

consequences. Simply stated, every time we measure a spectrum originating from a sub-wavelength feature of an object, **that spectrum does not directly represent the spectral fingerprint of that feature**. Hence, in general terms, the NGI highlights that (i) there are structural challenges in the way hyper-spectral imaging of very small objects is done (ii) those challenges are an exception in Photonics but the rule in the terahertz domain, because of the long wavelength (iii) the proper information is scrambled in space-time, but it is not lost. Interestingly, in order to retrieve the correct information, the NGI places the assumption that a field of interest is emitted from a specific plane and that the field emitted from any other plane is sufficiently dispersed in the space time to represent just a background. This concept is not dissimilar from the operating mechanism of the optical confocal microscope and it is proficiently used to image single planes in a thick object. it is then conceivable that the NGI could operate as a 3-D time-domain microscope (essentially a 4-dimensional imaging system). This fascinating perspective is currently under discussion at the EPic Lab and it might represent a uniquely disruptive development in the field.

5.4 Reflection on my PhD work

Initially, I expected the body of my PhD to contain implementations of near-field imaging, mainly based on the development of the NGI methodology. However, the project title was 'Nonlinear Terahertz Imaging' which is a rather vast term. It meant that I had some options in terms of the methods that I could explore, and I ended up focusing my time on the development of a methodology that I did not foresaw, the OP-TNFM. Incidentally, I had spent some weeks taking Optical-Pump-Optical-Probe transients of novel material structures as training at the beginning of my PhD; I had considered this 'wasted time' until years later it came to the time to demonstrate OP-TNFM methodology from the basis of near-field THz imaging. The time I had spent taking these transients was crucial to the relatively short turn around of the OP-TNFM project. There were many points like this - often research tasks aren't completed in a completely successive fashion. At the beginning, it is often an educated guess what preparations are critical to a research objective. This can give the timelines some unpredictability. Experimental physics projects can change and evolve due to constant re-assessment of their viability and progress. This progress is often impacted by technical issues that range from equipment wear-and-tear to requisition times from companies leading to modifications to the timeline. Because a PhD work needs to provide a genuine contribution to its field or specialty in a quite limited temporal span,

any change in the timeline represents a risk to this achievement. Due to the COVID-19 pandemic and other unforeseen circumstances my own completion was delayed. At times the creation of a thesis seemed like an impossible task, but then again so did many of the experimental tasks. Outside of the day-to-day of experimental physics, progress can come in leaps if a certain problem gets solved on a particular day. The process of design and assembly can often be cyclical because of the complexity of optical setups and the inter-dependencies between large numbers of elements. This meant that a lot of my time was devoted to understanding how to work with these systems and the best methods of implementing nonlinear processes. Over time, I became well-attuned to the alignment of optical setups and able to manually diagnose issues with high precision. This gradual skill development was also helpful in the final demonstration of the carrier methodologies. Work is generally highly collaborative in the Emergent Photonics Lab, though over the years I found myself collaborating less because I was so focused on the THz microscope methodology, and on developing the scope of that project. Perhaps I was a slave to familiarity, though I am glad that I developed the microscope as far as I did and achieving the OP-TNFM. I didn't expect the amount of preparation that would be required to bring a project to fruition, or realise that the seeds of success are planted years in advance. I think if there's any wisdom to be shared it's not to be afraid of wasting time on experiments that are only tangentially related to the PhD topic. A wide range of practical skills is instrumental to success.

Chapter 6

Publications and Conferences

Publications and Talks

J. S. Totero Gongora, L. Olivieri, L. Peters, J. Tunesi, V. Cecconi, A. Cutrona, R. Tucker, V. Kumar, A. Pasquazi, and M. Peccianti, "Route to Intelligent Imaging Reconstruction via Terahertz Nonlinear Ghost Imaging," Micromachines 11(5), 521 (2020).

L. Olivieri, J. S. T. Gongora, L. Peters, V. Cecconi, A. Cutrona, J. Tunesi, R. Tucker, A. Pasquazi, and M. Peccianti, "Hyperspectral terahertz microscopy via nonlinear ghost imaging," Optica 7(2), 186–191 (2020).

Robyn Tucker, Luke Peters, Juan S Totero Gongora, Jacob Tunesi, Maxwell Rowley, Alessia Pasquazi, Marco Peccianti "Video-Rate Terahertz Carrier Microscopy" (In Submission)

Invited Talks

J. S. Totero Gongora, L. Olivieri, L. Peters, V. Cecconi, A. Cutrona, J. Tunesi, R. Tucker, V. Kumar, A. Pasquazi, and M. Peccianti "Time-resolved nonlinear ghost imaging," SPb-POEM 2021 (St. Peterburg, Russia) (25-28/05/2021) (keynote).

L. Olivieri, J. S. Totero Gongora, L. Peters, V. Cecconi, A. Cutrona, J. Tunesi, R. Tucker, A. Pasquazi, and M. Peccianti "Terahertz Hyperspectral Nonlinear Ghost Imaging," SPb-POEM 2020 (St. Peterburg, Russia) (27-30/04/2021).

J. S. Totero Gongora, Luana Olivieri, Luke. Peters, Vittorio Cecconi, Antonio Cutrona, Jacob Tunesi, Robyn Tucker, Alessia Pasquazi, and Marco Peccianti , "Terahertz Hyperspectral Computational Microscopy", 2nd International Optics N.I.C.E. conference (12/10 – 14/10/2020) (keynote)

J. S. Totero Gongora, L. Olivieri, V. Cecconi, R. Tucker, L. Peters, J. Tunesi, A. Pasquazi, and M. Peccianti "Time-resolved nonlinear Ghost imaging: route to hyperspectral single-pixel characterisation at THz frequencies," EMN Prague Meeting on Terahertz,

(2019) A59, (Prague, Czech Republic) (10-14/06/2019)

CONFERENCES

Robyn Tucker, Luke Peters, Juan Sebastian Totero Gongora, Jacob Tunesi, Maxwell Rowley, Alessia Pasquazi, Marco Peccianti "Terahertz Near-Field Hot Carrier Microscopy", OSA Advanced Photonics Congress (AP)(26/07/2021) pIM1A.3

Robyn Tucker, Luke Peters, Juan S Totero Gongora, Jacob Tunesi, Maxwell Rowley, Alessia Pasquazi, Marco Peccianti "Subwavelength Video-Rate Terahertz Carrier Microscopy" CLEO/Europe-EQEC 2021. (23/06/2021) (Awarded) CH-7.3

J. S. Totero Gongora, L. Olivieri, L. Peters, V. Cecconi, A. Cutrona, J. Tunesi, R. Tucker, A. Pasquazi, and M. Peccianti, "Terahertz Hyperspectral Microscopy via Nonlinear Ghost Imaging," in OSA Advanced Photonics Congress (AP) 2020 (IPR, NP, NOMA, Networks, PVLED, PSC, SPPCom, SOF) (OSA, 2020), p. JM2E.6.

J. S. Totero Gongora, L. Olivieri, L. Peters, V. Cecconi, A. Cutrona, J. Tunesi, R. Tucker, A. Pasquazi, and M. Peccianti, "Hyperspectral THz Microscopy via Time-resolved Nonlinear Ghost Imaging," in Conference on Lasers and Electro-Optics (OSA, 2020), p. SM2F.4.

L. Olivieri, J. S. Totero Gongora, L. Peters, V. Cecconi, A. Cutrona, J. Tunesi, R. Tucker, A. Pasquazi and M. Peccianti "3D THz ghost-imaging via coherent spatio-temporal refocusing," Teranet-NPL 2019 (4-5/12/2019) (Awarded)

L. Olivieri, J. S. Totero Gongora, L. Peters, V. Cecconi, A. Cutrona, J. Tunesi, R. Tucker, A. Pasquazi and M. Peccianti "Terahertz Nonlinear Ghost Imaging," UK-THz Meeting, Warwick University, UK (11/12/2018)

L. Olivieri, J. S. T. Gongora, V. Cecconi, R. Tucker, L. Peters, J. Tunesi, A. Pasquazi, and M. Peccianti, "Time-Resolved Nonlinear Ghost Imaging," in PIERS 2019 (Rome, Italy) – SC2 (17–20/06/2019)

L. Olivieri, J. S. T. Gongora, V. Cecconi, R. Tucker, L. Peters, A. Pasquazi, and M. Peccianti, "Time-Resolved Nonlinear Ghost Imaging," in OSA Advanced Photonics Congress (AP) 2019 (IPR, Networks, NOMA, SPPCom, PVLED) (Optical Society of America, 2019), p. ITh2A.6. (29/07–1/08/2019)

L. Olivieri, J. S. Totero Gongora, V. Cecconi, R. Tucker, L. Peters, J. Tunesi, A. Pasquazi, and M. Peccianti "Hyperspectral single-pixel reconstruction at THz frequencies using Time-Resolved Nonlinear Ghost Imaging," CLEO/Europe-EQEC (2019), CC-3.4 WED, (23 – 27/06/2019)

Bibliography

Achenbach, J. (2000). Quantitative nondestructive evaluation. *International Journal of Solids and Structures*, 37(1-2):13–27. 3

Afalla, J., Gonzales, K. C., Prieto, E. A., Catindig, G., Vasquez, J. D., Husay, H. A., Tumanguil-Quitoras, M. A., Muldera, J., Kitahara, H., Somintac, A., Salvador, A., Estacio, E., and Tani, M. (2019). Photoconductivity, carrier lifetime and mobility evaluation of gaas films on si $<100>$ using optical pump terahertz probe measurements. *Semiconductor Science and Technology*, 34:035031. 15

Agarwal, G. S. (1975). Quantum electrodynamics in the presence of dielectrics and conductors. iv. general theory for spontaneous emission in finite geometries. *Physical Review A*, 12(4):1475–1497. 17, 34

Ashcroft, N. W. and Mermin, N. D. (1976). *Solid State Physics*. Harcourt College Publishers. 16

Augustin, S., Frohmann, S., Jung, P., and Hübers, H.-W. (2018). Mask responses for single-pixel terahertz imaging. *Scientific Reports*, 8(4886). 11, 12, 13, 14

Auston, D. H. (1983). Subpicosecond electro-optic shock waves. *Applied Physics Letters*, 43(8):713–715. 25, 28

Auston, D. H., Cheung, K. P., Valdmanis, J. A., and Kleinman, D. A. (1984). Cherenkov radiation from femtosecond optical pulses in electro-optic media. *Physical Review Letters*, 53(16):1555–1558. 28, 29

Auston, D. H., Johnson, A. M., Smith, P. R., and Bean, J. C. (1980). Picosecond optoelectronic detection, sampling, and correlation measurements in amorphous semiconductors. *Applied Physics Letters*, 37(4):371–373. 4, 21

Baillergeau, M., Maussang, K., Nirrengarten, T., Palomo, J., Li, L. H., Linfield, E. H.,

Davies, A. G., Dhillon, S., Tignon, J., and Mangeney, J. (2016). Diffraction-limited ultrabroadband terahertz spectroscopy. *Scientific Reports*, 6(24811). 9, 67

Balland, J. C., Zielinger, J. P., Noguet, C., and Tapiero, M. (1986). Investigation of deep levels in high-resistivity bulk materials by photo-induced current transient spectroscopy i. review and analysis of some basic problems. *Journal of Physics D: Applied Physics*, 19(57):57–70. 18

Bass, M., Franken, P. A., Ward, J. F., and Weinreich, G. (1962). Optical rectification. *Physical Review Letters*, 9(11):446–448. 25

Bassani, G. F. and Parravicini, G. P. (1993). *Electronic states and optical transitions in solids*. International series of monographs in the science of the solid state. Franklin Book Co., Elkin's Park, PA. 32, 33

Blanchard, F., Doi, A., Tanaka, T., Hirori, H., Tanaka, H., Kadoya, Y., and Tanaka, K. (2011). Real-time terahertz near-field microscope. *Optics Express*, 19(9):8277. 10, 11

Born, M. and Wolf, E. (1999). *Principles of Optics: Electromagnetic Theory of Propagation, Interference and Diffraction of Light (7th Edition)*. Cambridge University Press, 7th edition. 7

Boyd, R. W. (2003). *Nonlinear Optics*. Academic Press, San Diego, CA, 2nd edition. 22, 25, 26

Bullis, W. M. and Huff, H. R. (1996). Interpretation of carrier recombination lifetime and diffusion length measurements in silicon. *Journal of the Electrochemical Society*, 143(4):1399–1405. 17, 18, 34

Chan, W. L., Charan, K., Takhar, D., Kelly, K. F., Baraniuk, R. G., and Mittleman, D. M. (2008). A single-pixel terahertz imaging system based on compressed sensing. *Applied Physics Letters*, 93(121105). 6, 11, 12, 13, 15, 67

Chen, H.-T., Kersting, R., and Cho, G. C. (2003). Terahertz imaging with nanometer resolution. *Applied Physics Letters*, 83(15):3009–3011. 9, 56

Chen, Q., Jiang, Z., Xu, G. X., and Zhang, X. C. (2000). Near-field terahertz imaging with a dynamic aperture. *Optics Letters*, 25(15):1122–1124. 10, 61

Chen, X.-H., Liu, Q., Luo, K.-H., and Wu, L.-A. (2009). Lensless ghost imaging with true thermal light. *Optics Letters*, 34(5):695–697. 15

Courjon, D. and Bainier, C. (1994). Reports on progress in physics near field microscopy and near field optic. *Reports on Progress in Physics*, 57(10):989–1028. 9, 11

Cui, Y., Fu, W., Guan, X., Hu, M., Yan, Y., and Liu, S. (2012). Experiment studies on two-dimension terahertz raster scan imaging. *Journal of Infrared, Millimeter, and Terahertz Waves*, 33:513–521. 6

Curley, P. F. and Ferguson, A. I. (1991). Actively mode-locked ti:sapphire laser producing transform-limited pulses of 150-fs duration. *Optics Letters*, 16(13):1016–1018. 22

Dayton, J. A., Heinen, V. O., Stankiewicz, N., and Wallett, T. M. (1987). Submillimeter backward wave oscillators. *International Journal of Infrared and Millimeter Waves volume*, 8(10):1257–1268. 21

Fabian, D. J., Watson, L. M., and Marshall, C. A. W. (1971). Soft x ray spectroscopy and the electronic structure of solids. *Reports on Progress in Physics*, 34(2):601. 3

Fann, W. S., Storz, R., Tom, H. W. K., and Bokor, J. (1992). Electron thermalization in gold. *Physical Review B*, 46(20):592–595. 35

Fattinger, C. and Grischkowsky, D. (1988). Point source terahertz optics. *Applied Physics Letters*, 53:1480. 21

Federici, J. F., Mitrofanov, O., Lee, M., Hsu, J. W. P., Brener, I., Harel, R., Wynn, J., Pfeiffer, L. N., and West, K. W. (2002). Thz near-field imaging. *Physics in Medicine and Biology*, 47(21):3727–3734. 10

Fiore, A., Berger, V., Rosencher, E., Bravetti, P., and Nagle, J. (1998). Phase matching using an isotropic nonlinear optical material. *Nature*, 391:463–466. 26

Fischer, B., Hoffmann, M., Helm, H., Modjesch, G., and Jepsen, P. U. (2005). Chemical recognition in terahertz time-domain spectroscopy and imaging. *Semiconductor Science and Technology*, 20:S246–S253. 2

Fossom, J. G., Mertens, R. P., Lee, D. S., and Nijs, J. F. (1983). Carrier recombination and lifetime in highly doped silicon. *Solid State Electronics*, 26(6):569–576. 35

Fowle, G. R. (1989). *Introduction to Modern Optics*. Dover Publications, New York, dover edition (2nd) edition. 7, 8, 9, 15

Francis, K. J. G., Chong, M. L. P., E, Y., and Zhang, X.-C. (2020). Terahertz nonlinear index extraction via full-phase analysis. *Optics Letters*, 45(20). 5, 6

Gallot, G. and Grischkowsky, D. (1999). Electro optic detection of terahertz radiation. *Journal of the Optical Society of America B*, 16(8):1204–1212. 30

Gallot, G., Zhang, J., McGowan, R. W., Jeon, T.-I., and Grischkowsky, D. (1999). Measurements of the thz absorption and dispersion of znte and their relevance to the electro-optic detection of thz radiation. *Applied Physics Letters*, 74(23):3450–3452. 59

Garmire, E. M. and Yariv, A. (1967). Laser mode-locking with saturable absorbers. *IEEE Journal of Quantum Electronics*, QE-3(6):222–226. 1

Gente, R., Born, N., Voß, N., Sannemann, W., Leon, J., Koch, M., and Castro-Camus, E. (2013). Determination of leaf water content from terahertz time-domain spectroscopic data. *Journal of Infrared, Millimeter and Terahertz Waves*, 34:316–323. 4, 6

Gibson, G. M., Johnson, S. D., and Padgett, M. J. (2020). Single-pixel imaging 12 years on: a review. *Optics Express*, 28(19):28190–28208. 13, 14

Goetz, A. F. H., Gregg Vane, J. E. S., , and Rock, B. N. (1985). Imaging spectrometry for earth remote sensing. *Science*, 228(4704):1147–1153. 6

Greffet, J.-J. and Carminati, R. (1997). Image formation in near-field optics. *Progress in Surface Science*, 56(3):133–237. 10

Gu, X., Kockum, A. F., Miranowicz, A., xi Liu, Y., and Nori, F. (2017). Microwave photonics with superconducting quantum circuits. *Physics Reports*, 718-719:1–102. 2

Hall, R. N. (1959). Recombination processes in semiconductors. *Proceedings of the IEE - Part B: Electronic and Communication Engineering*, 106(17S):923–931. 35

Hawes, J. T. (2015). How mechanical tv works. http://www.hawestv.com/mtv_howMTVwks/howMTVwks.htm. 13

Heinz, F. D., Warta, W., and Schubert, M. C. (2017). Separation of the surface and bulk recombination in silicon by means of transient photoluminescence. *Applied Physics Letters*, 110(042105). 18, 35

Helminger, P., K.Messer, J., and Lucia, F. C. D. (1983). Continuously tunable coherent spectroscopy for the 0.1-1.0-thz region. *Applied Physics Letters*, 42(4):309–310. 2

Hirori, H., Doi, A., Blanchard, F., and Tanaka, K. (2011). Single cycle terahertz pulses with amplitudes exceeding 1 mv/cm generated by optical rectification in lithium niobate. *Applied Physics Letters*, 98:091106. 28, 29, 30, 40

Hopfield, J. (1958). Theory of the contribution of excitons to the complex dielectric constant of crystals. *Physical Review*, 112(5):1555–1567. 34

Hu, B. B. and Nuss, M. C. (1995). Imaging with terahertz waves. *Optics Letters*, 20(16):1716–1718. 6, 11

Hu, X., Zhang, H., Zhao, Q., Yu, P., Li, Y., and Gong, L. (2019). Single-pixel phase imaging by fourier spectrum sampling. *Applied Physics Letters*, 114(051102). 12

Hunsche, S. (1998). Thz near-field imaging. *Optics Communications*, 150:22–26. 6, 7, 10

Ito, H., Naito, H., and Inaba, H. (1975). Generalized study on angular dependence of induced second-order nonlinear optical polarizations and phase matching in biaxial crystals. *Journal of Applied Physics*, 46(9):3992–3998. 22, 26

Jepsen, P. U., Cooke, D. G., and Koch, M. (2011). Terahertz spectroscopy and imaging – modern techniques and applications. *Laser & Photonics Review*, 5(1):124–166. 3, 30

Jiang, T., Tan, W., Huang, X., Nan, S., Bai, Y., and Fu, X. (2021). Detail reconstruction in ghost imaging with undersampling. *Journal of Optics*, 23(075201). 12

Jiang, Z., Xu, X. G., and Zhang, X. C. (2000). Improvement of terahertz imaging with a dynamic subtraction technique. *Applied Optics*, 39(17):2982–2987. 64, 65

Jiang, Z. and Zhang, X. C. (1998). Single-shot spatiotemporal terahertz field imaging. *Optics Letters*, 23(14):1114–1116. 29

Jones, R. C. (1941). A new calculus for the treatment of optical systems i. description and discussion of the calculus. *Journal of the Optical Society of America*, 31(7):488–493. 31

Joyce, H. J., Eyre, L., Adeyemo, S. O., Baig, S. A., Boland, J. L., Davies, C. L., Johnston, M. B., Deschler, F., Tan, H. H., and Jagadish, C. (2018). Probing the photophysics of semiconductor nanomaterials using optical pump-terahertz probe spectroscopy: from nanowires to perovskites. volume 5805 of *(Proc. SPIE 10724)*. Physical Chemistry of Semiconductor materials and Interfaces XVII. 15, 35

Jung, D., Bank, S., Lee, M. L., and Wasserman, D. (2017). Next-generation mid-infrared sources. *Journal of Optics*, 19(12):123001. 2

Kar, S., Nguyen, V. L., Mohapatra, D. R., Lee, Y. H., and Sood, A. K. (2018). Ultrafast spectral photoresponse of bilayer graphene: Optical pump–terahertz probe spectroscopy. *ACS Nano*, 12(2):1785–1792. 18

Keiber, S., Sederberg, S., Schwarz, A., Trubetskov, M., Pervak, V., Krausz, F., and Karpowicz, N. (2016). Electro-optic sampling of near-infrared waveforms. *Nature Photonics*, 10:159–163. 30, 64

Kim, Y.-H. and Shih, Y. (1999). Experimental realization of popper's experiment: Violation of the uncertainty principle? *Foundations of Physics*, 29:1849–1861. 14

Lai, X.-J., Tu, H.-Y., Wu, C.-H., Lin, Y.-C., and Cheng, C.-J. (2015). Resolution enhancement of spectrum normalization in synthetic aperture digital holographic microscopy. *Applied Optics*, 54(1):A52–A58. 10

Lash, A. A. and Yundev, D. N. (1984). Submillimeter laser interferometry with pyroelectric image recording. *International Journal of Infrared and Millimeter Waves*, 5(8):1153–1163. 6

Lecaque, R., Grésillon, S., Barbey, N., Peretti, R., Rivoal, J.-C., and Boccara, C. (2011). Thz near-field optical imaging by a local source. *Optics Communications*, 262(1):125–128. 11

Lee, Y.-S. (2009a). *Basic Theories of Terahertz Interaction with Matter. In: Principles of Terahertz Science and Technology*. Springer. Boston, MA. 1

Lee, Y.-S. (2009b). *Principles of Terahertz Science and Technology*, volume 170. Springer Science & Business Media, 1st edition. 9

Leitenstorfer, A., Hunsche, S., Shah, J., Nuss, M. C., and Knox, W. H. (1999). Detectors and sources for ultrabroadband electro-optic sampling: Experiment and theory. *Applied Physics Letters*, 74(11):1516–1518. 30

Leonhardt, R., Holzapfel, W., .Zinth, W., and Kaiser, W. (1987). Terahertz quantum beats in molecular liquids. *Chemical Physics Letters*, 133(5):373–377. 4

Lewis, A. and Lieberman, K. (1991). Near-field optical imaging with a non-evanescently excited high-brightness light source of sub-wavelength dimensions. *Nature*, 354:214–216. 10

Lewis, A., Taha, H., Strinkovski, A., Manevitch, A., Khatchatouriants, A., Dekhter, R., and Ammann, E. (2003). Near-field optics: from subwavelength illumination to nanometric shadowing. *Nature Biotechnology*, 21(11):1378–1386. 9

Linnros, J. (1998). Carrier lifetime measurements using free carrier absorption transients.ii. lifetime mapping and effects of surface recombination. *Journal of Applied Physics*, 84(1):284–291. 18

Liu, H. (2020). Imaging reconstruction comparison of different ghost imaging algorithms. *Scientific Reports*, 10:14626. 67

Liu, J., Schmutz, H., and Merkt, F. (2009). Generation of widely tunable fourier-transform-limited terahertz pulses using narrowband near-infrared laser radiation. *Journal of Molecular Spectroscopy*, 256(1):111–118. 5, 59

Lyon, S. A. (1986). Spectroscopy of hot carriers in semiconductors. *Journal of Luminescence*, 35(3):121–154. 33, 34

Macfaden, A. J., Reno, J. L., Brener, I., and Mitrofanov, O. (2014). 3 μm aperture probes for near-field terahertz transmission microscopy. *Applied Physics Letters*, 104(011110). 9

Maine, P., Strickland, D., Bado, P., Pessot, M., and Mourou, G. (1988). Generation of ultrahigh peak power pulses by chirped pulse amplification. *IEEE Journal of Quantum Electronics*, 24(2):398–403. 29

Manly, H. P. and Gorder, L. O. (1951). *Drake's Cyclopedia of Radio and Electronics A Reference and Instruction Book Radio, Sound Systems, Television, Photoelectricity, Electronic Tubes, Electronics in Industry.* Frederick J. Drake Co. Publishers, 14th edition. 12

Mao, P., Wei, Y., Li, H., and Wang, J. (2017). Junction diodes in organic solar cells. *Nano Energy*, 41:717–730. 19

Marouf, M. S. (2021). Study of the damage threshold of optical surfaces of high-power energy pulse lasers with changing coefficient of optical surface roughness, and the damage threshold is increased by thermal treatment of optical glass. *Journal of Optics and Physics Sciences*, 2(4):1–8. 63

Meiklejohn, R. A., Meyer, R. J., Aronovic, S. M., Schuette, H. A., and Meloch, V. W. (1957). Characterization of long-chain fatty acids by infrared spectroscopy. *Analytical Chemistry*, 29(3):329–334. 3

Mickan, S., Abbott, D., Munch, J., Zhang, X.-C., and van Doorn, T. (2000). Analysis of system trade-offs for terahertz imaging. *Microelectronics Journal*, 31(7):503–514. 66

Mitrofanov, O. (2000). Terahertz near-field microscopy based on a collection mode detector. *Applied Physics Letters*, 77(3496). 9, 10

Mitrofanov, O., Lee, M., Hsu, J. W. P., Pfeiffer, L. N., West, K. W., and Wynn, J. D. (2001). Terahertz pulse propagation through small apertures. *Applied Physics Letters*, 79(907). 9

Mittleman, D. M. (2017). Perspective: Terahertz science and technology. *Journal of Applied Physics*, 122(230901). 21

Murray, J. E. and Lowdermilk, W. H. (1980). Nd : Y ag regenerative amplifier. *Journal of Applied Physics*, 51(7):3548–3555. 22

Nahata, A., Weling, A. S., and Heinz, T. F. (1996). A wideband coherent terahertz spectroscopy system using optical rectification and electro-optic sampling. *Applied Physics Letters*, 69(16):2321–2323. 5

Niessen, K. A. and Markelz, A. (2013). Optimization of thz microscopy imaging. Mainz, Germany. 59, 63

Nuss, M. C., Auston, D. H., and Capasso, F. (1987). Direct subpicosecond measurement of carrier mobility of photoexcited electrons in gallium arsenide. *Physical Review Letters*, 58(22):2355. 4

Okumura, K. and Tanimura, Y. (1998). Two-dimensional thz spectroscopy of liquids: non-linear vibrational response to a series of thz laser pulses. *Chemical Physics Letters*, 295(4):298–304. 4

Olivieri, L., Gongora, J. S. T., Pasquazi, A., and Peccianti, M. (2018). Time-resolved nonlinear ghost imaging. *ACS Photonics*, 5(8). 15, 68, 71, 72

Olivieri, L., Gongora, J. S. T., Peters, L., Cecconi, V., Cutrona, A., Tunesi, J., Tucker, R., Pasquazi, A., and Peccianti, M. (2020). Hyperspectral terahertz microscopy via nonlinear ghost imaging. *Optica*, 7(2):186. 73, 74, 75, 76

Papaioannou, E. T. and Beigang, R. (2021). Thz spintronic emitters: a review on achievements and future challenges. *Nanophotonics*, 10(4):1243–1257. 21

Parker, W. D. (2012). Silicon. 17

Pessot, M., Maine, P., and Mourou, G. (1987). 1000 times expansion/compression of optical pulses for chirped pulse amplification. *Optics Communications*, 62(6):419–421. 28

Peters, L., Tunesi, J., Pasquazi, A., and Peccianti, M. (2017). Optical pump rectification emission: Route to terahertz free-standing surface potential diagnostics. *Scientific Reports*, 7:9805. 11

Pittman, T. B., Shih, Y. H., Strekalov, D. V., and Sergienko, A. V. (1995). Optical imaging by means of two-photon quantum entanglement. *Physical Review A*, 52(5):R3429. 14

Proctor, C. M., Kuik, M., and Nguyen, T.-Q. (2013). Charge carrier recombination in organic solar cells. *Progress in Polymer Science*, 38(12):1941–1960. 18, 19

Ragy, S. and Adesso, G. (2012). Nature of light correlations in ghost imaging. *Scientific Reports*, 2(651). 67

Ravi, K., Huang, W. R., Carbajo, S., Nanni, E. A., Schimpf, D. N., Ippen, E. P., and Kärtner, F. X. (2015). Theory of terahertz generation by optical rectification using tilted-pulse-fronts. *Optics Letters*, 23(4):5253–5276. 29, 30

Rice, A., Jin, Y., Ma, X. F., Zhang, X., Bliss, D., Larkin, J., and Alexander, M. (1994). Terahertz optical rectification from< 110 >zinc-blende crystals. *Applied Physics Letters*, 64(11):1324–1326. 11, 25, 26

Rossi, F. and Kuhn, T. (2002). Theory of ultrafast phenomena in photoexcited semiconductors. *Reviews of Modern Physics*, 74(3):895–950. 34

Rossler, U. (2009). *Solid State Theory: an Introduction*. Springer-Verlag, 2nd edition. 17, 18, 32

Rottenfusser, R., Wilson, E. E., and Davidson, M. W. (2021). Numerical aperture and resolution. `http://zeiss-campus.magnet.fsu.edu/articles/basics/resolution.html`. 8

Sah, C.-T., Noyce, R. N., and Shockley, W. (1957). Carrier generation and recombination in p-n junctions and p-n junction characteristics. *Proceedings of the IRE*, 45(9):1228–1243. 19

Schall, M. and Jepsen, P. U. (2000). Freeze-out of difference-phonon modes in znte and its application in detection of thz pulses. *Applied Physics Letters*, 77(18):2801–2803. 59

Schneider, A., Neis, M., Stillhart, M., Ruiz, B., Khan, R. U. A., and Günter, P. (2006). Generation of terahertz pulses through optical rectification in organic dast crystals: theory and experiment. *Journal of the Optical Society of America B*, 23(9):1822–1835. 25, 26, 27

Seo, M., Kang, J.-H., Kim, H.-S., Cho, J. H., Choi, J., Jhon, Y. M., Lee, S., Kim, J. H., Lee, T., Park, Q.-H., and Kim, C. (2015). Observation of terahertz-radiation induced ionization in a single nano island. *Scientific Reports*, 5(10280). 2, 3

Shapiro, J. H. (2008). Computational ghost imaging. *Physical Review A*, 78(6):061802. 14, 15

Shapiro, J. H. and Boyd, R. W. (2012). The physics of ghost imaging. *Quantum Information Processing*, 11:949–993. 13, 14

Shiers, G. (1997). *Early Television: A Bibliographic Guide to 1940*. Taylor & Francis. ISBN 978-0-8240-7782-2. 12

Shrekenhamer, D., Watts, C. M., and Padilla, W. J. (2013). Terahertz single pixel imaging with an optically controlled dynamic spatial light modulator. *Optics Express*, 21(10):12507–12518. 12

Siemion, A. (2021). The magic of optics—an overview of recent advanced terahertz diffractive optical elements. *Sensors*, 21(100). 7, 56

Smith, R. P., Hwang, A. A.-C., Beetz, T., and Helgren, E. (2018). Introduction to semiconductor processing: Fabrication and characterization of p-n junction silicon solar cells. *American Journal of Physics*, 86(10):740–746. 19

Stantchev, R. I., Sun, B., Hornett, S. M., Hobson, P. A., Gibson, G. M., Padgett, M. J., and Hendry, E. (2016). Noninvasive, near-field terahertz imaging of hidden objects using a single-pixel detector. *Science Advances*, 2(6). 15, 68

Strickland, D. and Mourou, G. (1985). Compression of amplified chirped optical pulses. *Optics Communications*, 55(6):447–449. 2, 22

Suizu, K., Koketsu, K., Shibuya, T., Tsutsui, T., Akiba, T., and Kawase, K. (2009). Extremely frequency-widened terahertz wave generation using cherenkov-type radiation. *Optics Express*, 17(8):6676–6681. 25, 27

Tani, M., Horita, K., Kinoshita, T., Que, C. T., Estacio, E., Yamamoto, K., and Bakunov, M. I. (2011). Efficient electro-optic sampling detection of terahertz radiation via cherenkov phase matching. *Optics Express*, 19(21):19901–19906. 28

Times (1907). Sending photographs by telegraph. *The New York Times*. 11

Tomandl, M. (2021). Near field and far field. 8

Totero-Gongora, J. S. (2019). Resolution calculation. Technical report, University of Sussex, Department of Physics and Astronomy. 56

Turtaev, S., Leite, I. T., Mitchell, K. J., Padgett, M. J., Phillips, D. B., and Izmar, T. C. (2017). Comparison of nematic liquid-crystal and dmd based spatial light modulation in complex photonics. *Optics Express*, 25(24):29874–29884. 70

Valdmanis, J., Mourou, G., and Gabel, C. (1983). Subpicosecond electrical sampling. *IEEE Journal of Quantum Electronics*, 19(4):664–667. 4

van Exter, M., Fattinger, C., and Grischkowsky, D. (1989). Terahertz time-domain spectroscopy of water vapor. *Optics Letters*, 14(20):1128–1130. 5

Vaz, P. G., Amaral, D., Ferreira, L. F. R., Morgado, M., and Cardoso, J. (2020). Image quality of compressive single-pixel imaging using different hadamard orderings. *Optics Express*, 28(8):11666–11680. 14, 71

Walther, M., Cooke, D. G., Sherstan, C., Hajar, M., Freeman, M. R., and Hegmann, F. A. (2007). Terahertz conductivity of thin gold films at the metal-insulator percolation transition. *Physical Review B*, 76(125408). 60

Wang, B., Zhong, S., Lee, T.-L., Fancey, K. S., and Mi, J. (2020). Non-destructive testing and evaluation of composite materials/structures: A state-of-the-art review. *Advances in Mechanical Engineering*, 12(4):1–28. 3

Wang, K., Mittleman, D. M., van der Valk, N. C. J., and Planken, P. C. M. (2004). Antenna effects in terahertz apertureless near-field optical microscopy. *Applied Physics Letters*, 85(14):2715–2717. 10

Wang, X., Cui, Y., Hu, D., Sun, W., ShengYe, J., and Zhang, Y. (2008). Terahertz quasi-near-field real-time imaging. *Optics Communications*, 282(24):4683–4687. 6

Wang, X., Cui, Y., Sun, W., Ye, J. S., and Zhang, Y. (2010). Terahertz real-time imaging based on balanced electro-optic detection. *Journal of the Optical Society of America A*, 27(11):2387–2393. 10

Wei, Z., Zhang, J., Xu, Z., and Liu, Y. (2020). Optimization methods of compressively sensed image reconstruction based on single-pixel imaging. *Applied Sciences*, 10(3288). 13

Weingarten, K. J., Rodwell, M. J. W., and Bloom, D. M. (1988). Picosecond optical sampling of gaas integrated circuits. *IEEE Journal of Quantum Electronics*, 24(2):198–220. 4, 12, 57, 64

Williams, G. P. (2005). Filling the thz gap—high power sources and applications. *Reports on Progress in Physics*, 69(2):301. 2

Woodward, R. M., Cole, B. E., Wallace, V. P., Pye, R. J., Arnone, D. D., Linfield, E. H., and Pepper, M. (2002). Terahertz pulse imaging in reflection geometry of human skin cancer and skin tissue. *Physics in Medicine and Biology*, 47(21):3853–3863. 4

Wu, Q. and Zhang, X. C. (1995). Free-space electro-optic sampling of terahertz beams. *Applied Physics Letters*, 67(24):3523–3525. 4, 30, 59

Wyncke, B. and Brehat, F. (1989). Calculation of the effective second-order nonlinear coefficients along the phase matching directions in acentric orthorhombic biaxial crystals. *Journal of Physics B: Atomic, Molecular and Optical Physics*, 22(2):363–376. 25, 26

Wynne, K. and Jaroszynski, D. A. (1999). Superluminal terahertz pulses. *Optics Letters*, 24(1):25–27. 6, 7, 9, 11

Yang, K. H., Richards, P. L., and Shen, Y. R. (1971). Generation of Far-Infrared Radiation by Picosecond Light Pulses in $LiNbO_3$. *Applied Physics Letters*, 19(9):320–323. 4

Yeh, K.-L., Heffman, M., Hebling, J., and Nelson, K. A. (2007). Generation of $10\mu j$ ultrashort terahertz pulses by optical rectification. *Applied Physics Letters*, 90:171121. 26

Yoneda, H., Morikami, H., Ueda, K.-I., and More, R. M. (2003). Ultrashort-pulse laser ellipsometric pump-probe experiments on gold targets. *Physical Review Letters*, 91(7):075004. 35

Yu, C., Fang, S., Sun, Y., and Pickwell-Macpherson, E. (2012). The potential of terahertz imaging for cancer diagnosis: A review of investigations to date. *Quantitative Imaging in Medicine and Surgery*, 2(1):33–45. 4

Zeng, Y., Qiang, B., and Wang, Q. J. (2020). Photonic engineering technology for the development of terahertz quantum cascade lasers. *Advanced Optical Materials*, 8(3):1900573. 3

Zenhausern, F., O'Boyle, M. P., and Wickramasinghe, H. K. (1994). Apertureless near-field optical microscope. *Applied Physics Letters*, 65(13):1623–1625. 10

Zhang, X., Ma, X. F., Jin, Y., Lu, T., Boden, E. P., Phelps, P. D., Stewart, K. R., and Yakymyshyn, C. P. (1992). Terahertz optical rectification from a nonlinear organic crystal. *Applied Physics Letters*, 61(26):3080–3082. 5

Zheng, Z.-P., Fan, W.-H., Liang, Y.-Q., and Yan, H. (2012). Application of terahertz spectroscopy and molecular modeling in isomers investigation: Glucose and fructose. *Optics Communications*, 285(7):1868–1871. 2